Dust and star formation in NGC 4449

Oskar Łukasz Karczewski

under supervision of
Prof M. J. Barlow and Prof M. J. Page

Submitted for the degree of Doctor of Philosophy

London · 2013

I, *Oskar Łukasz Karczewski*, confirm that the work presented in this thesis is my own. Where information has been derived from other sources, I confirm that this has been indicated in the thesis.

Abstract

The low degree of processing of the interstellar medium (ISM) in nearby metal-poor galaxies, such as NGC 4449, allow them to be viewed as local analogues of the first galaxies formed in the Universe. In this work we present a study of dust and star formation in NGC 4449, both on global and local scales.

We present the spectral energy distribution (SED) of NGC 4449 from the FUV to the submm. Our analysis of a global optical spectrum of NGC 4449 suggests an early onset of star formation, while our results from a chemical evolution dust model provide an indication of the chemical composition of dust globally. These results were used as constraints in constructing a photoionization and radiative transfer MOCASSIN model of NGC 4449. The presented iterative scheme allowed us to infer a total mass of the youngest stellar population which is likely to reside in the centre, in the SW and in the N of NGC 4449. The derived global recent star formation rate is in good agreement with previous estimates. We conclude that our scheme is a new tool, which is particularly suitable for deriving integrated properties of galaxies.

Based on spectroscopic observations from the *Spitzer Space Telescope* and the *Herschel Space Observatory* we obtained a detailed view of the ionized regions, the photo-dissociation regions and the dust emission within NGC 4449. Our results suggest a deficit of ionized polycyclic aromatic hydrocarbons (PAHs) near the centre of NGC 4449 and bright $[\mathrm{O\,III}]_{88}$ emission dominating the ISM cooling locally.

Additionally, we examined a sample of type Ibc supernovae to assess their possible contribution to dust formation in the early Universe. We found that the estimated dust masses are too low to consider type Ibc supernovae as major dust producers.

To my wife Valérie,
and to my children Philip and Mary

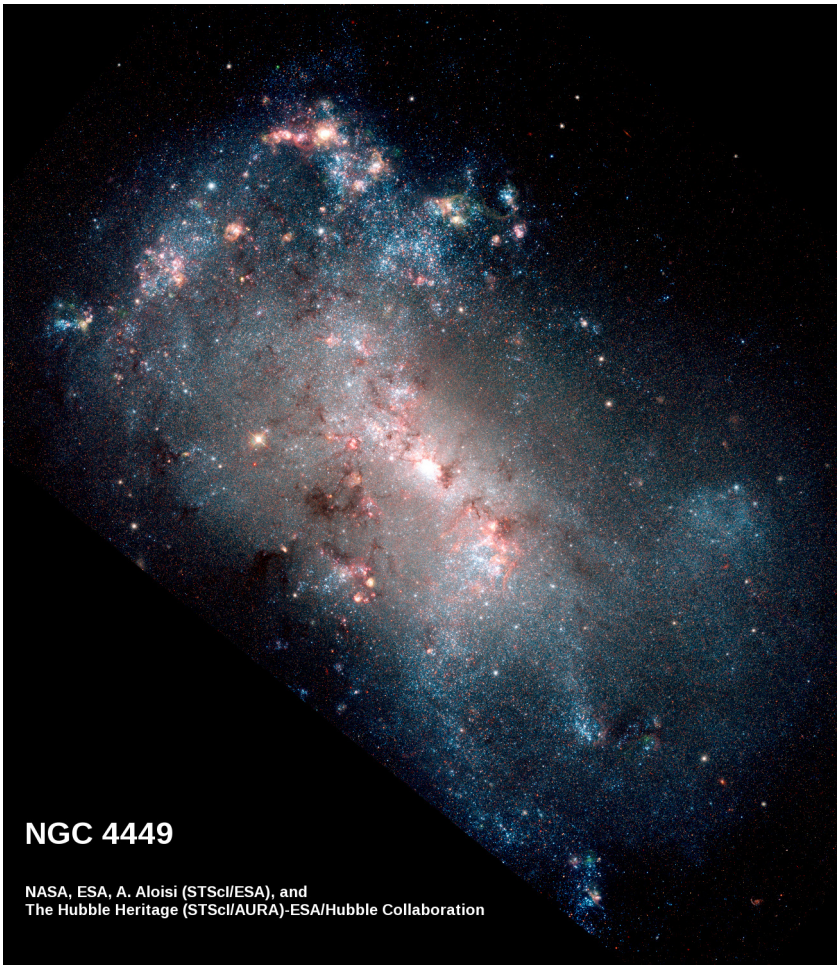
NGC 4449
NASA, ESA, A. Aloisi (STScI/ESA), and
The Hubble Heritage (STScI/AURA)-ESA/Hubble Collaboration

Contents

List of Figures

List of Tables

1 Introduction

Nature has endowed humans with a unique ability to reason. Our innate desire to understand the world around us and our ability to consciously interact with it form the corner stone of science and make humans truly unique beings. We have developed a variety of conceptual tools to build the framework of the scientific method, so that all investigations, whether in history or in biology, satisfy the same standards of organisation and self-consistency, and are placed in the context of contemporary understanding.

Physical sciences study inanimate and material components of our world. In most fields in physics understanding is developed by performing laboratory experiments and comparing their results to observations. However, in studies of the Universe direct experiments are not possible. We gain insight into the world beyond the Earth only by passively observing radiation that emerges from the deep space. Astronomy and astrophysics, from observational and theoretical perspectives, aim to describe the Universe we observe today, but also to study its origin and its possible fate.

The observed electromagnetic radiation in the Universe arises from a wide range of physical environments. At optical wavelengths, the night sky is dominated by emission from individual stars nearby, star clusters and galaxies. The emission from stars arises from thermonuclear reactions in their interiors (e.g. Bethe 1939). Cores of stars similar to our Sun have temperatures of $\approx 10^7$ K which allow fusion of hydrogen nuclei and a net energy release of 26.2 MeV for every helium nucleus formed (e.g. Salpeter 1952, Hayashi & Cameron 1962). At later stages of stellar evolution hydrogen in the core is exhausted and, depending on the initial mass of a star, elements heavier than helium may be synthesised. In massive stars, consecutive fusion reactions continue up to the formation of iron, and the products of nuclear fusion are eventually injected into the interstellar medium (ISM) through supernova explosions (e.g. Reeves & Salpeter 1959, Hoyle & Wickramasinghe 1970). Stars with masses less than ~ 8 $M_\odot$ undergo mass loss during the asymptotic giant branch (AGB) phase, shed their outer envelopes and collapse to become white dwarfs (e.g. Liebert 1980, Kaler 1985, Bryan et al. 1990). Through these later stages of stellar evolution, the local ISM is enriched with heavy elements, or metals, produced in stellar interiors. At sufficiently low temperatures metals condense to form interstellar dust (e.g. Salpeter 1977). Stellar deaths reduce the intensity of the ambient radiation field, which, together with the presence of newly synthesised heavy elements, allows more effective cooling of the ISM (e.g. Tielens & Hollenbach 1985, Neufeld et al. 1995). Local gas density fluctuations, which may be triggered by gravitational encounters or outflows from neighbouring stars, may lead to gravitational instabilities and the formation of dense molecular clouds (e.g. Toomre 1964, Oey & Massey 1995, Elmegreen 2002, Krumholz & McKee 2005). In time, a new generation of stars may be born and the process will start again.

Therefore, the processes governing star formation depend on physical and chemical properties of the local environments, which, on the other hand, can be studied on many physical scales. For example, studies of chemical pathways in a molecular cloud may explain the

formation of an important coolant (e.g. Woods et al. 2012), calculations based on known physical laws may show whether or not the cloud is likely to collapse and form a star (e.g. Burkert & Alves 2009), observations of gas density distribution in galaxies may show an underlying relationship between observable parameters on larger scales (e.g. Kennicutt 1989), and simulations involving a large number of galaxies may explain the structure of the Universe, such as the observed large-scale clustering of galaxies (e.g. Springel et al. 2005). This concept is illustrated in Fig. 1.1.

Each constituent particle of the local environment, whether an atom, a star, or an entire galaxy continuously interacts with its immediate neighbourhood by emitting or absorbing electromagnetic radiation and by exchanging energy through collisions or gravitational encounters. By selecting appropriate tools and instruments, the escaping radiation can be interpreted to offer valuable insight into the past, present and sometimes even the future of the studied environment.

The interstellar medium

The ISM in a galaxy is composed of atoms, molecules and dust particles, together forming a complex and dynamic system. Local density fluctuations of gas may lead to gravitational instabilities, formation of molecular clouds and, eventually, stars (e.g. Toomre 1964, Kennicutt 1989, Bastien et al. 1991, Elmegreen 2002). Star-forming processes may also be triggered by compression of pre-existing clouds by stellar winds (e.g. Oey & Massey 1995). Supernova explosions, delivering substantial amounts of kinetic energy into the local ISM, may trigger as well as hinder star formation (e.g. Wada & Norman 2001, Hartmann et al. 2001, Nagakura et al. 2009). Through these later phases of stellar evolution the local ISM is enriched chemically with heavy elements produced in stellar interiors. As a result, the physical and chemical composition of the ISM changes with time and varies within the galaxy. Thus, studies of the ISM can provide an important insight into the galaxy's past and present.

The ISM is illuminated and heated by nearby stellar emission but also by cosmic rays, high-energy X-ray emission from accreting binaries, supernova remnants or active galactic nuclei (AGN; e.g. Begelman 1985). As photons are absorbed by atoms or molecules in the ISM, their electrons are excited into higher energy levels or may be ejected, which results in ionization. Ionized species recombine by capturing a free electron, which cascades down the energy ladder emitting photons as it loses energy (e.g. Bowen 1928). At optical wavelengths the Hα and Hβ lines are the most prominent emission lines arising from the ionized ISM. However, certain excitation states with lower transition probability have long lifetimes for radiative de-excitation and are more likely to be de-excited by a collision at laboratory conditions. Transitions involving these states are known as forbidden, and they require low gas densities to be observed (e.g. Bowen 1936). Thus, below a specific gas density, or critical density, which is unique for every transition, forbidden lines may be readily observed and used to probe the conditions in the ISM. Such lines are known as diagnostic lines.

Local electron temperatures and electron densities may be quantified from ratios of diagnostic lines of the same species, e.g. the [N II] or the [O III] line ratios at optical wavelengths (e.g. Czyzak et al. 1986). The strengths of $[\mathrm{O\,III}]_{\lambda4363}$, $[\mathrm{O\,III}]_{\lambda4959}$ and $[\mathrm{O\,III}]_{\lambda5007}$ together with $[\mathrm{O\,II}]_{\lambda\lambda3726,9}$ are also commonly used in direct determinations of the ISM oxygen abundance and metallicity through the electron temperature $T_\mathrm{e}(\mathrm{O\,III})$ and the electron density $n_\mathrm{e}(\mathrm{O\,II})$ and by assuming a 'standard' ionization structure (e.g. Peimbert 1967, Peimbert &

a

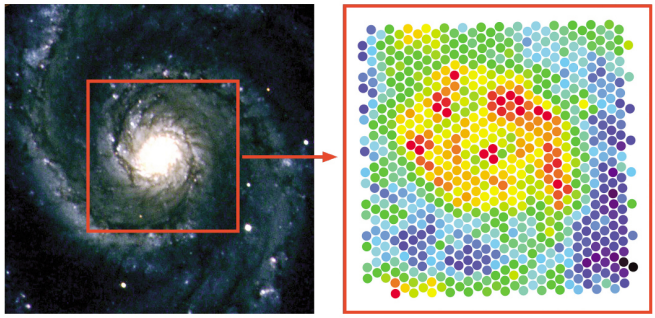

b

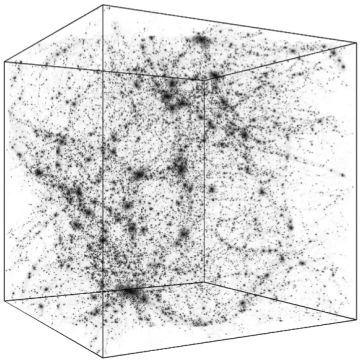

c

Figure 1.1. Star formation processes can be studied on three physical scales. The dark molecular cloud Barnard 68 located 125 pc from the Earth *(a)* is 0.13 pc across. Its very high gas density allows only one in 10^{12} photons of visible light to escape, giving the dark appearance. In about 200,000 years a star like our Sun will be born in the cloud's centre (Burkert & Alves 2009; image credit: ESO). In the Whirlpool Galaxy *(b)* new stars form primarily near the centre and in the spiral arms. The rate of star formation in the observed individual 170 pc regions is closely related to the local gas density (Blanc et al. 2009; image credit: G. Blanc/K. Fricke/T. Jones/McDonald Obs.). On the largest scale *(c)*, supercomputers are used to simulate the evolution of galaxies and the formation of galaxy clusters to learn how the Universe we observe today was formed. One side of the simulated volume is 80 Mpc in length and each point represents one galaxy (Kravtsov 2006).

Costero 1969, Peimbert & Torres-Peimbert 1977). However, elemental abundances may also be determined from other bright emission lines in instances when the weak $[\mathrm{O\,III}]_{\lambda4363}$ is not detected (e.g. Pagel et al. 1979, Alloin et al. 1979, Hidalgo-Gámez & Ramírez-Fuentes 2009).

Nebular lines are important probes of the quality of the local interstellar radiation field (ISRF). Lines arising from high energy states, such as $[\mathrm{Ne\,III}]_{15.56}$ with an ionization potential of 40.96 eV, are emitted from within ionized regions, or H II regions, located close to massive, recently formed stars. Ratios of different ionization stages of the same species, e.g. $[\mathrm{Ne\,III}]_{15.56}/[\mathrm{Ne\,II}]_{12.8}$, can therefore be used to probe the hardness of the ionizing spectrum (e.g. Groves et al. 2008b).

Fine-structure lines arise from collisional excitation of electrons into higher J levels followed by radiative de-excitation, e.g. $^2P_{3/2} \rightarrow {}^2P_{1/2}$ for $[\mathrm{C\,II}]_{158}$ in the far-infrared (FIR; e.g. Cooksy et al. 1986, Goldsmith et al. 2012). Because of their relatively low critical densities and low excitation and ionization energies, fine-structure lines such as $[\mathrm{O\,I}]_{63}$ or $[\mathrm{C\,II}]_{158}$ are useful probes of the photo-dissociation regions (PDRs) at interfaces between the ionized and the neutral gas (e.g. Chokshi et al. 1988, Tielens & Hollenbach 1985, Stacey et al. 1991). They are often bright in star-forming regions (e.g. Brauher et al. 2008).

Overall, the collisional excitation and the subsequent emission of photons by atomic or molecular species allows cooling of the ISM and balances heating through ionization and the photoelectric ejection of electrons from dust grains (e.g. Tielens & Hollenbach 1985). Radiative cooling is particularly important in star-forming regions where additional heat is generated by gravitational collapse of protostellar clouds (e.g. Goldsmith & Langer 1978, Neufeld et al. 1995).

Depending on the environment, gas heating may be dominated by electron emission from polycyclic aromatic hydrocarbons (PAHs) or small dust grains, but may also be traced by continuum emission from large dust grains in the FIR if a constant photoelectric efficiency is assumed (e.g. Watson 1972, Bakes & Tielens 1994). The efficiency of gas heating can be defined as the fraction of the interstellar FUV energy that is absorbed by dust and contributes to neutral gas heating, through the photoelectric effect. It can be quantified through a ratio of the intensity of cooling lines to the total intensity of dust emission (e.g. Tielens & Hollenbach 1985).

A detailed study of the galaxies NGC 1097 and NGC 4559 showed that $([\mathrm{O\,I}]_{63} + [\mathrm{C\,II}]_{158})/I_{\mathrm{FIR}}$ varies between 0.6 per cent and 0.3 per cent, while $([\mathrm{O\,I}]_{63} + [\mathrm{C\,II}]_{158})/I_{\mathrm{PAH}}$ remains approximately constant at 6 per cent across different environments (Croxall et al. 2012). Similarly, in the giant H II region LMC-N11B the ratios amount to $\approx$0.55 per cent and 7 per cent, respectively (Lebouteiller et al. 2012). In these objects a tight correlation between $[\mathrm{O\,I}]_{63} + [\mathrm{C\,II}]_{158}$ and I_{PAH} suggested that the PAHs dominate gas heating, whereas a constant ratio $([\mathrm{O\,I}]_{63} + [\mathrm{C\,II}]_{158})/I_{\mathrm{PAH}}$ indicated that the lines $[\mathrm{O\,I}]_{63}$ and $[\mathrm{C\,II}]_{158}$ dominate the ISM cooling.

Therefore spectroscopic observations allow us to determine *(i)* the abundances and the degree of ionization of individual elements, *(ii)* the physical properties of the ionized and neutral gas, *(iii)* the quality of the ISRF, and *(iv)* the details of the heating and cooling processes in the ISM.

The interstellar dust

Interstellar dust takes the form of small solid particles, or dust grains, and is one of the major components of the ISM in galaxies. Its presence can be inferred at UV and optical wavelengths from varying degrees of interstellar extinction, also known as interstellar absorption or reddening. The degree of extinction may be probed and quantified by, for example, comparing the observed and theoretical intensities of nebular Balmer-series transitions (e.g. Miller & Mathews 1972). The absorption of stellar energy by dust contributes to gas heating through the photoelectric effect (e.g. Watson 1972) and is accompanied by thermal emission from heated dust at FIR wavelengths (e.g. Neugebauer et al. 1984).

While the existence of such extinction in the UV/optical, or the presence of FIR continuum emission can be attributed to the presence of dust grains in the ISM, more detailed studies are needed to establish their chemical composition. Direct studies of dust grains in the Earth's vicinity only recently became possible with the launch of the *Stardust* spacecraft. In 2000–2004 *Stardust* captured samples of interplanetary and interstellar dust and dust from the tail of the comet Wild 2, revealing its solar as well as pre-solar origin (Brownlee et al. 2006). Laboratory measurements of candidate dust species show important differences in their optical properties, which enable a variety of grain species in the ISM to be identified (e.g. Stecher 1969, Draine & Lee 1984). Thus, the chemical composition of interstellar dust in galaxies can be inferred from spectroscopic and photometric constraints (e.g. Zubko et al. 2004).

Studies of AGB stars reveal FIR dust emission, implying dust formation in their outflows (e.g. van Loon et al. 1999, Matsuura et al. 2009). Detailed observations of the recent and nearby supernova SN 1987A provided evidence of MIR and FIR emission from dust in its ejecta (e.g. Wooden et al. 1993, Ercolano et al. 2007, Matsuura et al. 2011). Indeed, net formation of interstellar dust is believed to take place predominantly in outflows from AGB stars and in type II supernova ejecta, such as SN 1987A (e.g. Barlow 2009, Tielens 2012).

Dwarf galaxies and NGC 4449

Dwarf galaxies are less massive, fainter in appearance and less chemically processed than regular galaxies, such as the Andromeda Galaxy (e.g. Hunter 1997). Therefore, they may be viewed as local analogues of the first galaxies formed in the Universe and are of key importance in developing our understanding of the processes of star formation.

Fig. 1.2 shows an idealised structure of the ISM near a star. In a metal-poor ISM, fewer metals are available to absorb energy as dust grains. Therefore, the ionizing UV photons penetrate deeper into the interstellar clouds. This hinders the formation of carbon monoxide (CO), which is the dominant coolant within PDRs. As a consequence, the shell of CO shrinks, and CO is no longer an effective tracer of the total mass of the molecular gas (e.g. Madden et al. 2006, Schruba et al. 2012). Since the efficiency of molecular hydrogen cooling at higher gas densities decreases, the first stars in the Universe were generally more massive, having formed from larger and warmer clouds (e.g. Bromm et al. 1999, Kreckel et al. 2010). Thus, the conditions in the ISM of metal-poor galaxies are significantly different from the conditions in the more evolved galaxies.

In this work we present a study of dust and star formation focused on NGC 4449, which is a nearby barred Magellanic-type irregular galaxy (de Vaucouleurs et al. 1991, Corwin et al. 1994) seen face-on. It is forming stars twice as actively as the Andromeda Galaxy (e.g.

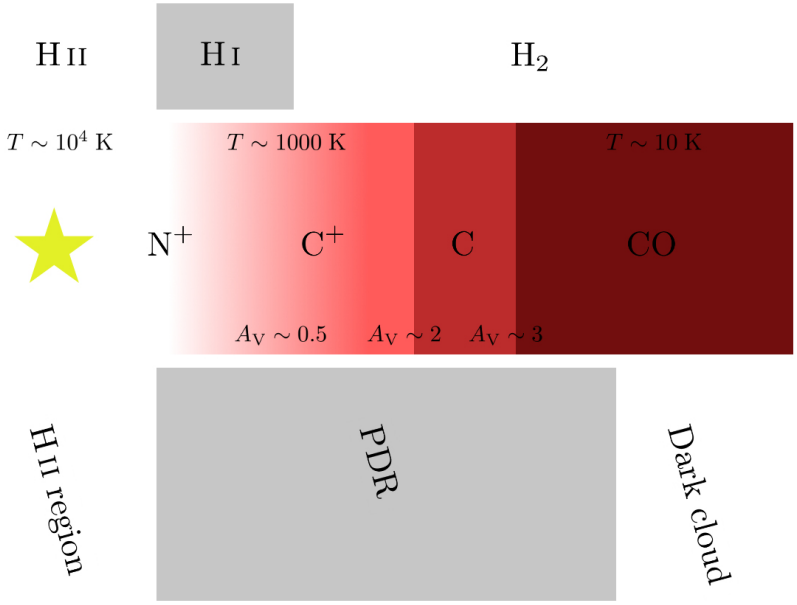

Figure 1.2. Diagram showing an idealised physical and chemical structure of the interstellar medium (ISM) near a star. High energy photons emitted by the star (middle left) ionize the gas forming an H II region around the star. At a certain distance from the star, most photons with enough energy to ionize hydrogen will have been absorbed. Recombination of free electrons with protons now allows a shell of neutral hydrogen (H I) to form. Within this photo-dissociation region (PDR) the radiation is still too energetic for survival of complex molecular species, but the reduced number of free electrons and collisions between atoms effectively lower the ambient temperature. When enough shielding from high energy photons is achieved and the gas is sufficiently cool, dense molecular clouds form (see Fig. 1.1) and may later collapse to form new stars. (Image adapted from Hony 2011.)

Hunter et al. 1999, Ford et al. 2013), yet holds approximately one third of Andromeda's metal content (e.g. Engelbracht et al. 2008, Yin et al. 2009). NGC 4449, observed by the *Herschel Space Observatory* as part of the Dwarf Galaxy Survey (DGS; Madden et al. 2013), was chosen for this study because of its wide range of existing observations extending from the far-UV to the FIR.

The *Spitzer Space Telescope* (Werner et al. 2004), in full operation in 2003–2009, and the *Herschel Space Observatory* (Pilbratt et al. 2010), in operation in 2009–2013, provided science instruments which were key to this work:

Spitzer InfraRed Array Camera (IRAC; Fazio et al. 2004) covers the wavelength range 3.2–9.2 μm in four channels centred at 3.6, 4.5, 5.8 and 8 μm, probing the warm dust continuum and the PAH emission,

Spitzer InfraRed Spectrograph (IRS; Houck et al. 2004) covers the spectral range 5.2–38 μm, probing the emission lines from ionized gas and the emission features from the PAH molecules,

Herschel Photodetector Array Camera and Spectrometer (PACS; Poglitsch et al. 2010) in the photometry mode, covers the wavelength range 60–210 μm in three channels centred at 70, 100 and 160 μm, probing the warm dust continuum emission; in the spectroscopy mode, covers the spectral range 51–220 μm over the field-of-view (FOV) of $47'' \times 47''$, probing the emission from neutral and ionized gas,

Herschel Spectral and Photometric Imaging REceiver (SPIRE; Griffin et al. 2010) in the photometry mode, covers the wavelength range 210–600 μm in three channels centred at 250, 350 and 500 μm, probing the cool dust continuum emission; in the spectroscopy mode, not used in this study, covers the spectral range 194–671 μm, probing the emission from molecular gas.

In interpreting these observations we used MOCASSIN (MOnte CArlo SimulationS of Ionized Nebulae; Ercolano et al. 2003, 2005, 2008), a photoionization and radiative transfer code, which predicts the emission lines and the spectral energy distribution (SED) from the given geometry of the modelled environment, the elemental abundances and the distribution of gas and dust.

Thus, a global, galaxy-wide view of NGC 4449 is presented in Chapter 2, including a self-consistent gas and dust model, a description of the dominant stellar populations and a model of dust evolution in galaxies such as NGC 4449. On a smaller scale, in Chapter 3 we describe the H II regions, the PDRs, the dust emission, the balance of ISM heating and cooling and the recent star formation activity within NGC 4449.

In Chapter 4 we examine dust formation in type Ibc supernovae to estimate the contribution of type Ibc supernovae to the total dust production in the Universe. The conclusions and a discussion of potential future work are presented in Chapter 5.

For consistency we use the author's 'we' throughout.

2 Modelling the spectral energy distribution, the ionization structure and the star formation history of NGC 4449

The work described in this chapter was published in MNRAS by O. Ł. Karczewski, M. J. Barlow, M. J. Page, N. P. M. Kuin, I. Ferreras, M. Baes, G. J. Bendo, A. Boselli, A. Cooray, D. Cormier, I. De Looze, M. Galametz, F. Galliano, V. Lebouteiller, S. C. Madden, M. Pohlen, A. Rémy-Ruyer, M. W. L. Smith, and L. Spinoglio with title 'A multiwavelength study of the Magellanic-type galaxy NGC 4449 – I. Modelling the spectral energy distribution, the ionization structure and the star formation history' and reference MNRAS (2013), 431(3), 2493–2512 (doi: 10.1093/mnras/stt345).

The Herschel data products described in Section 2.2.3 were provided by the Dwarf Galaxy Survey (DGS) collaboration (Madden et al. 2013).

2.1 Introduction

The conditions in the interstellar medium (ISM) in a galaxy and the environment-dependent processes governing the formation of stars and dust can be studied on many physical scales. Considering an entire galaxy, the interplay between the underlying stellar emission, the degree of radiation reprocessing taking place in the ISM and the thermal or non-thermal emission due to dynamical or evolutionary processes give rise to a unique pattern of emission and absorption features in the observed spectral energy distribution (SED).

The spectroscopic measurements alone provide a wealth of information about the ionized (H II) regions or photo-dissociation regions (PDRs) in galaxies (e.g. Guseva et al. 2004; Vasta et al. 2010). Studies constrained by broadband photometric measurements can allow a better understanding of the main components of the thermal continuum, namely, the stellar emission and the emission due to interstellar dust. Observed emission lines and diagnostic line ratios provide important further constraints (Martínez-Galarza et al. 2011). Synthetic single stellar populations (SSPs) can be used to characterise star-forming regions within galaxies (e.g. Groves et al. 2008a, Ferreras et al. 2012), or to decompose the observed SEDs of entire galaxies (e.g. Amorín et al. 2012). The composition of dust and the masses of dust species can be inferred from observations by assuming measured laboratory properties of dust (e.g. Galliano et al. 2008a and references therein). Together, these components can provide an in-depth view of a galaxy (e.g. Cormier et al. 2012, Hermelo et al. 2013).

Numerical models reproducing all the available photometric and spectroscopic measure-

ments across a wide range of wavelengths can provide the most complete picture of the integrated properties of a galaxy. We wish to examine a multicomponent model treating the stellar content, the gaseous phase and the dust within a galaxy in a self-consistent way. Our initial goals include finding a robust numerical scheme, which could be applied to a sample of dwarf galaxies in order to study the details of their star formation histories and dust content.

In this work, we describe the first multicomponent observation-driven model of a galaxy generated with the photoionization and radiative transfer code MOCASSIN (Ercolano et al. 2003, 2005, 2008), which includes a simultaneous and self-consistent treatment of the stellar component, the gaseous phase, its ionization structure and multiple dust species. MOCASSIN is a fully three-dimensional code, whose recent applications include modelling the extreme bipolar planetary nebula NGC 6302 (Wright et al. 2011) and studying dust emission by supernova ejecta (Wesson et al. 2010). Applying MOCASSIN to simulate entire galaxies is more resource-consuming since both the gas phase and the dust phase need to be treated self-consistently over relatively large physical scales. The small intrinsic size of dwarf galaxies make them ideal candidates for such multiwavelength studies. Indeed, dwarf galaxies provide small self-contained but dynamic environments. As such, they are useful in developing our understanding of mechanisms underlying star formation, including chemical enrichment and feedback processes, especially for low-metallicity objects resembling those formed at earlier epochs in the evolution of the Universe.

In a similar context, MOCASSIN was first used to model Mrk 996 (James 2009). In this work we describe a model of the well-known starburst galaxy NGC 4449, which is a low-metallicity [$\log(\mathrm{O/H}) + 12 = 8.23$, $1/3\mathrm{Z}_{\odot}$; Engelbracht et al. 2008] actively star-forming (SFR $\sim 0.5\ \mathrm{M}_{\odot}\,\mathrm{yr}^{-1}$; Hunter et al. 1998, Hill et al. 1998) barred Magellanic-type irregular galaxy (de Vaucouleurs et al. 1991, Corwin et al. 1994) seen face-on. At a distance of 3.8 Mpc (Annibali et al. 2008) its H I envelope extends to 12.9 kpc ($11'.6$), equal to approximately three Holmberg radii (Swaters et al. 2002, Hunter et al. 1999), and forms a pronounced system of streamers with a counter-rotating H I core, which may be indicative of past mergers (Hunter et al. 1999, Theis & Kohle 2001). NGC 4449 is particularly suitable for multiwavelength studies because of its wide range of existing photometric data extending to the far-infrared (FIR). The new observations acquired with the *Spitzer* Space Telescope (Werner et al. 2004) and the *Herschel* Space Observatory (Pilbratt et al. 2010) are essential in studying gas cooling processes and the properties of dust in the ISM of NGC 4449.

In the following sections we discuss in detail a model of NGC 4449 based on multiple observational constraints and including a treatment of polycyclic aromatic hydrocarbons (PAHs). Thus, in Section 2.2 we describe the observations and data reduction techniques, and in Section 2.3 we describe the modelling method, as well as the assumptions and the convergence criteria adopted. The results and discussion are presented in Section 2.4, and the conclusions follow in Section 2.5. In Chapter 3 we study the FIR cooling lines and discuss properties of PDRs inferred from spatially-resolved spectroscopic observations of NGC 4449.

2.2 Photometric observations and data reduction

In constructing the observed SED of NGC 4449 we have used data from previous studies (e.g, Kennicutt 1992, Engelbracht et al. 2008, Bendo et al. 2012b, Hunter et al. 1986, Böttner et al. 2003) and from systematic surveys [Sloan Digital Sky Survey (SDSS), York et al. 2000, Two

Micron All Sky Survey (2MASS), Skrutskie et al. 2006, *WISE*, Wright et al. 2010 and *Planck*, Planck Collaboration 2011]. We present archival data from *GALEX* (Martin et al. 2005; UV wavebands) and *Swift* (Gehrels et al. 2004; UV and optical wavebands), as well as new FIR photometry from *Herschel* (Pilbratt et al. 2010). A journal of observations is given in Table 2.1.

In Table 2.2 we list all global photometric measurements used to construct the observed SED for NGC 4449. Existing submillimetre SCUBA (Submillimetre Common-User Bolometer Array) measurements at 450 μm and 850 μm (Böttner et al. 2003) were omitted from the list of photometric measurements due to their incomplete field-of-view (FOV) and the availability of space borne *Herschel* and *Planck* observations offering a similar wavelength coverage. Five illustrative false-colour images of NGC 4449 over selected broadband ranges are presented in Fig. 2.1.

2.2.1 Ultraviolet observations with GALEX and Swift

At UV wavelengths NGC 4449 has been observed by two recent space-borne missions, *GALEX* (in two UV bands) and the *Swift* Ultraviolet/Optical Telescope (UVOT; in three UV and three optical bands). Standard aperture photometry using the in-flight calibration of Morrissey et al. (2007) was performed on tile 5228 acquired as part of *GALEX* Nearby Galaxy Survey and accessible via General Release 6. The overall uncertainties include photometric repeatability measurements by Morrissey et al. (2007).

Swift/UVOT (Roming et al. 2005) offers four times the angular resolution of *GALEX* in three narrow UV bands. The telescope is equipped with a photon-counting detector and was originally designed to detect and observe gamma-ray bursts. As a consequence, standard data reduction procedures cannot be applied straightforwardly to observations of extended sources. In the Appendix we discuss this problem in detail and present a method of obtaining global photometry, which is appropriate for extended sources.

2.2.2 Optical observations with SDSS

In addition to the optical fluxes derived from the *Swift*/UVOT observations, SDSS observations in five optical bands (u, g, r, i and z) are available as part of Data Release 7. NGC 4449 is contained entirely within one field, thus minimizing deblending or sky subtraction issues which may arise in the case of extended sources. Standard aperture photometry was performed using elliptical apertures and the counts were converted into flux densities as described by West et al. (2010). The uncertainties in the derived fluxes are dominated by uncertainties in sky determination and subtraction.

2.2.3 Far-infrared observations with Herschel

NGC 4449 has been observed by *Herschel* (Pilbratt et al. 2010) as part of the Dwarf Galaxy Survey (DGS; Madden et al. 2013) with its two imaging photometers: the Photodetector Array Camera and Spectrometer (PACS; Poglitsch et al. 2010) at 70 μm, 100 μm and 160 μm and the Spectral and Photometric Imaging REceiver (SPIRE; Griffin et al. 2010) at 250 μm, 350 μm and 500 μm. The Full Width at Half Maximum (FWHM) of the PSF is $5\farcs2$, $7\farcs7$, $12\farcs0$, $18\farcs2$, $24\farcs9$, $36\farcs3$ in these bands, respectively. The details of all PACS and SPIRE data reduction steps, including error estimation, can be found in Rémy-Ruyer et al. (2013).

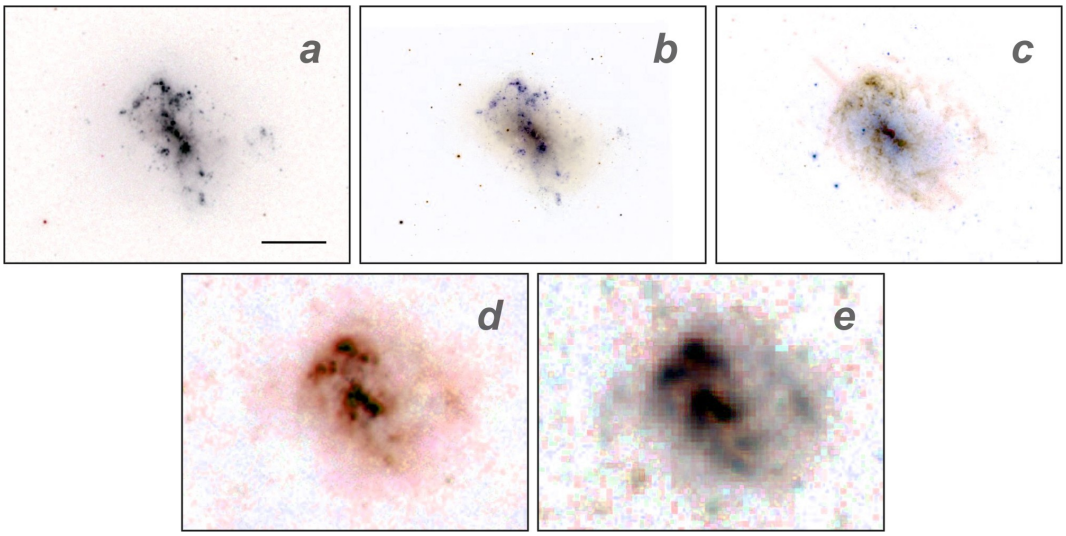

Figure 2.1. False-colour (R, G, B) broadband images of NGC 4449: *(a) Swift*/UVOT (2486 Å, 2221 Å, 1991 Å), *(b)* SDSS (*r*, *g*, *u*), *(c) Spitzer*/IRAC (8 μm, 5.8 μm, 3.6 μm), *(d) Herschel*/PACS (160 μm, 100 μm, 70 μm) and *(e) Herschel*/SPIRE (500 μm, 350 μm, 250 μm). North is up, east is to the left. The images are centred at $12^{\rm h}28^{\rm m}11\overset{\rm s}{.}1$, $+44°05'37''$ (J2000). The bar in the top left image is $2'$ in length (2.2 kpc).

Instrument	Bandpass/$\lambda_{\rm eff}$	Time (s)	Date observed	Observation ID
	New observations			
Herschel/PACS	70 μm + 160 μm	3497	2011 May 16	1342221125
	70 μm + 160 μm	3497	2011 May 16	1342221126
	100 μm + 160 μm	3497	2011 May 16	1342221127
	100 μm + 160 μm	3497	2011 May 16	1342221128
Herschel/SPIRE	250 μm, 350 μm, 500 μm	1035	2010 June 12	1342198243
	Archival observations			
Swift/UVOT	*uvw2*/2030Å	1544	2007 Mar 27	00035873001
	uvm2/2231Å	1091	2007 Mar 27	00035873001
	uvw1/2634Å	771	2007 Mar 27	00035873001
	u/3501Å	385	2007 Mar 27	00035873001
	b/4329Å	385	2007 Mar 27	00035873001
	v/5402Å	385	2007 Mar 27	00035873001
GALEX	FUV/1539Å	835	2006 Mar 15	tile 5228
	NUV/2316Å	765	2006 Mar 15	tile 5228
SDSS	*u*/3551Å	54	2003 Mar 24	3813/1/41/237/241
	g/4686Å	54	2003 Mar 24	3813/1/41/237/245
	r/6165Å	54	2003 Mar 24	3813/1/41/237/237
	i/7481Å	54	2003 Mar 24	3813/1/41/237/239
	z/8931Å	54	2003 Mar 24	3813/1/41/237/243

Table 2.1. List of observations.

Survey/instrument	$\lambda_{\rm eff}$	F_ν	Aperture[a]	Reference
GALEX	1539 Å	152 ± 12 mJy	11.′5	(1)
	2316 Å	183 ± 9 mJy	7.′5	
Swift/UVOT	1991 Å	175 ± 12 mJy	8.′5 × 6′	(1)
	2221 Å	189 ± 14 mJy		
	2486 Å	202 ± 15 mJy		
	3442 Å	249 ± 22 mJy		
	4321 Å	463 ± 41 mJy		
	5410 Å	611 ± 57 mJy		
SDSS	3551 Å	242 ± 5 mJy	6.′5 × 4.′7	(1)
	4686 Å	457 ± 14 mJy		
	6165 Å	573 ± 40 mJy		
	7481 Å	622 ± 50 mJy		
	8931 Å	683 ± 34 mJy		
2MASS	1.24 μm	916 ± 21 mJy	8′[b]	(2)
	1.66 μm	1070 ± 30 mJy		
	2.16 μm	839 ± 31 mJy		
WISE	3.4 μm	391 ± 7 mJy	4.′0 × 2.′8	(3)
	4.6 μm	251 ± 4 mJy		
	12 μm	954 ± 17 mJy		
	22 μm	2860 ± 60 mJy		
Spitzer/IRAC	3.6 μm	493 ± 15 mJy	...	(4)
	4.5 μm	317 ± 10 mJy		
	5.8 μm	615 ± 19 mJy		
	8 μm	1420 ± 40 mJy		
IRAS	12 μm	2.1 ± 0.2 Jy	8′	(5)
	25 μm	4.7 ± 0.5 Jy		
	60 μm	36 ± 3 Jy		
Spitzer/MIPS	24 μm	3.29 ± 0.13 Jy	9.′3 × 6.′6	(6)
	70 μm	43.8 ± 4.4 Jy		
	160 μm	78.1 ± 9.4 Jy		
Herschel/PACS	70 μm	49.3 ± 2.5 Jy	8.′3	(7)
	100 μm	75.9 ± 3.8 Jy		
	160 μm	79.5 ± 4.0 Jy		
Herschel/SPIRE	250 μm	35.7 ± 2.5 Jy	8.′3	(7)
	350 μm	16.2 ± 1.1 Jy		
	500 μm	5.6 ± 0.4 Jy		
Planck	350 μm	16.14 ± 0.34 Jy	6.′1 × 5.′2[c]	(8)
	550 μm	4.97 ± 0.24 Jy	5.′8 × 4.′8[c]	
	850 μm	1.45 ± 0.15 Jy	6.′0 × 4.′4[c]	
IRAM	1.2 mm	260 ± 40 mJy	two fields 2.′3	(9)

[a] given as diameters for circular apertures or major × minor axes for elliptical apertures; [b] major axis of the 'total' aperture; [c] FWHM of a Gaussian fit

Table 2.2. Summary of the derived photometric data for NGC 4449. All fluxes have been corrected for the foreground extinction using $E(B-V) = 0.019$ (Schlegel et al. 1998) and the extinction law of Cardelli et al. (1989) with $R_V = 3.1$. References: (1) this work; (2) 2MASS All-Sky Extended Source Catalog (Skrutskie et al. 2006); (3) *WISE* All-Sky Source Catalog (Wright et al. 2010); (4) Engelbracht et al. (2008); (5) Hunter et al. (1986); (6) Bendo et al. (2012b); (7) Rémy-Ruyer et al. (2013); (8) *Planck* Early Release Compact Source Catalogue (Planck Collaboration 2011); (9) Böttner et al. (2003).

The PACS observations were performed as four pairs of orthogonal scans covering an area of $24' \times 24'$. We used an adapted version of the standard script of v7.0 of the Herschel Interactive Processing Environment (HIPE; Ott 2010). The basic processing includes flagging bad or saturated pixels, converting the signal into Jy/pixel and applying the flatfield correction. Additionally, we systematically masked column 0 of all of the constituent 16×16 matrices in the PACS array to avoid electronic crosstalk and we performed second level deglitching. The resulting Level 1 products were converted into maps with the pixel size of 2, 2 and 4 arcsec for the three PACS bands and processed with Scanamorphos (Roussel 2012), which is particularly suitable for extended sources with low frequency noise. The integrated PACS fluxes of NGC 4449 are well represented by a 40 K blackbody and suitable colour corrections were applied accordingly (Müller et al. 2011b), where no additional correction factors are required to correct for the extended nature of the source (Sauvage 2011). The quoted uncertainties include the calibration uncertainties at 5 per cent in all bands (Rémy-Ruyer et al. 2013, Müller et al. 2011a).

The SPIRE observations were performed as two orthogonal scans covering an area of $24' \times 24'$. The corresponding maps were reduced using a modified version of the SPIRE pipeline in HIPE. The steps up to Level 1 were identical to those in the original pipeline provided by the SPIRE Instrument Control Center (ICC). Additionally, residual baseline subtraction was performed by subtracting the median of the time-lines for each bolometer over the entire observation (Pohlen et al. 2010). This was followed by an iterative process to completely remove residual signals that appear as stripes in the maps (Bendo et al. 2010). The final map was constructed using Naive Mapper available in HIPE and calibrated for an extended source. A modified blackbody fit of the form $S_\nu \propto \nu^\beta B_\nu(T)$ yields $\beta \approx 2$ globally for NGC 4449 (Rémy-Ruyer et al. 2013), which was used for colour correction of the integrated fluxes (SPIRE Observers' Manual; Valtchanov 2011). The uncertainties include the revised overall calibration uncertainties at 7 per cent in all SPIRE bands (Griffin & Lim 2011).

2.2.4 2MASS, WISE and Planck catalogue data

Global 2MASS photometric measurements for NGC 4449 were taken from columns `j_m_ext`, `h_m_ext` and `k_m_ext` of the 2MASS All-Sky Extended Source Catalog, and were subsequently converted to flux densities using the zero points tabulated by Cohen et al. (2003). *WISE* photometry was taken from columns `gmag` and `gerr` of the *WISE* All-Sky Source Catalog. Colour correction was applied using interpolated correction factors suitable for a source emitting as $\nu^{-1.18}$ across the four *WISE* bands. *Planck* photometry was taken from column `GAUFLUX(_ERR)` of the Early Release Compact Source Catalogue. Similarly, the interpolated colour correction factors used were suitable for a source emitting as $\nu^{2.80}$ across the *Planck* bands centred at 350, 550 and 850 μm.

2.3 Modelling method

2.3.1 Overview

The numerical code MOCASSIN (MOnte CArlo SimulationS of Ionized Nebulae; Ercolano et al. 2003, 2005, 2008) was originally intended as a tool to construct realistic models of

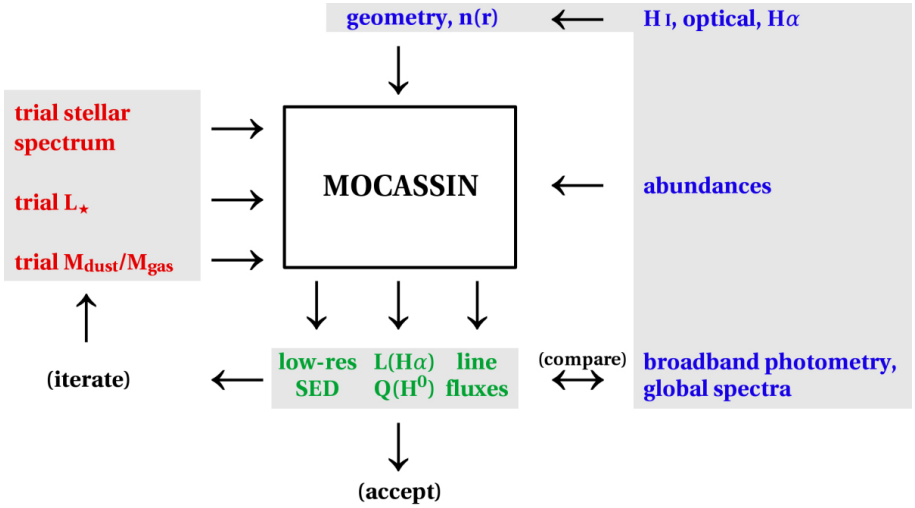

Figure 2.2. Summary of the modelling method. The shaded regions group together the input variables (left) the outputs (middle) and the observational constrains (right).

photoionized nebulae. It allows arbitrary three-dimensional geometries, separate for gas and dust, multiple ionizing sources emitting with a given input spectrum, variable gas chemistry, multiple dust species and arbitrary dust grain size distributions. Given these input parameters, the code self-consistently solves the radiative transfer in the coexisting gas and dust phases and calculates the ionization degree, electron temperature and dust grain temperature at every grid cell, and the overall emergent SED of the gas and dust.

In the sections that follow we will describe how MOCASSIN (v2.02.70) can be used to model large physical systems, such as galaxies. Our model is constructed 'bottom-up', where as many parameters as possible are fixed a priori based on observations. The simulations are set up with the empirical elemental abundances and the observed radial gas distribution fixed. The input stellar spectrum corresponding to a mixture of stellar populations, scaled by the stellar luminosity $L_\star$, and the dust to gas mass ratio ($M_{\rm dust}/M_{\rm gas}$) are free parameters. Based on these input parameters, which form a theoretical model of a galaxy, MOCASSIN produces a predicted low-resolution SED and a full set of predicted emission line intensities. If these predictions agree with observations, the original parameter set can be regarded as a true representation of the galaxy under the assumptions made. Otherwise, individual parameters can be adjusted and simulations repeated iteratively, as summarised schematically in Fig. 2.2.

In constructing our MOCASSIN model of NGC 4449 we have made simplifying assumptions about the geometry, gas density distribution, elemental abundances, dust composition and dust grain size distribution.

We have also made assumptions about the star formation history. In Section 2.3.4 we discuss a general picture of the stellar populations in NGC 4449, obtained using the spectral decomposition code STARLIGHT. In Section 2.3.7 we characterise the youngest stellar population based on observational constraints. Finally, in Section 2.3.7 we fit the older populations taking into account the constraints from earlier sections.

The fitting of the star formation history and dust is performed almost simultaneously for self-consistency. Therefore, the young stellar population, the episodes of star formation and dust are never modelled on their own. The youngest stellar population is fitted together

with a representative sample of older populations, and the final dust content is determined relatively early in the process to ensure self-consistency.

The assumptions listed below form basis of the iterative scheme described in detail in Section 2.3.7.

2.3.2 Gas density distribution

Spherical symmetry is assumed. Although MOCASSIN is a fully three-dimensional code, this capability is not exploited at this time due to technical limitations (see Section 2.3.6). However, the method presented in this work can be very easily adapted for fully three-dimensional modelling and the first step towards such modelling is discussed in Section 2.4.4.

We used the H I radial profile of Swaters et al. (2002) to approximate $n_{\rm H}(r)/{\rm cm}^{-3}$ as four second-order polynomials in the form $ar^2 + br + c$ for radii up to 3.3 kpc (3′.0), corresponding to the extent of the galaxy in the FIR (Fig. 2.1). Although NGC 4449 is highly irregular, for simplicity we treat the star formation regions cumulatively, and based on the optical image (Fig. 2.1) we assume that all gas is ionized within a distance of ~ 0.4 kpc from a single ionizing source. The total observed H I mass for NGC 4449 is 2–2.5 $\times$ 10^9 $M_\odot$ (Swaters et al. 2002; Bajaja et al. 1994), which is distributed between a system of streamers of mass 9×10^8 $M_\odot$ and the central region with diameter 24–35 kpc and mass 1.1–1.25 $\times$ 10^9 $M_\odot$ (Hunter et al. 1998, 1999). The H I mass within the radius of 3.3 kpc derived using our formulation is 5.5×10^8 $M_\odot$, which is consistent with the estimated total of 1.1–1.25 $\times$ 10^9 $M_\odot$ for the inner system given the radial surface density profile of Swaters et al. (2002).

The mass of H_2, based on $L_{\rm CO(1–0)} = 8.4 \times 10^6$ K km s^{-1} pc^2 (corrected for $D = 3.8$ Mpc; Böttner et al. 2003) and assuming $\alpha_{\rm CO} \sim$ 10–20 $M_\odot$ (K km s^{-1} pc^2)$^{-1}$ (cf. Sandstrom et al. 2012, Schruba et al. 2012 and references therein), can be estimated at $\sim$ 0.8–1.7 $\times$ 10^8 $M_\odot$. However, we note that CO-to-H_2 conversion factors for low metallicity objects are very uncertain, and therefore we include no estimates of H_2 mass in our gas mass totals.

We assumed that all gas exists in small clumps described by the filling factor ϵ, which is the same at all radii. Considering a Strömgren sphere of radius 0.4 kpc with $L_{\rm H\alpha}$ given by Hunter et al. (1999) and assuming that the average electron density is equal to the central $n_{\rm e}$ given by Martin (1997), we derive an initial estimate of $\epsilon \sim 0.003$. This is revisited in Section 2.3.7. Using similar assumptions and the formalism of Barlow (1987) we estimate that the mass of ionized gas is $\sim 1.5 \times 10^6$ $M_\odot$.

2.3.3 Elemental abundances

Elemental abundances are assumed to be constant throughout the galaxy. The abundances were taken from Vigroux et al. (1987), except for carbon, neon and sulphur, where the Large Magellanic Cloud (LMC) ratios for C/O, Ne/O and S/O were assumed (Russell & Dopita 1992). Although the sophisticated framework offered by MOCASSIN can also be used to determine elemental abundances (Ercolano et al. 2010), in this work MOCASSIN is not used in this context.

2.3.4 Star formation history

Star formation histories are difficult to constrain because of observational limitations (e.g. instrumental sensitivity), but also because of the more fundamental age-metallicity degen-

eracy (e.g. Worthey 1994; Ferreras et al. 1999; Ferreras & Silk 2003). However, a galactic spectrum contains age-sensitive features (e.g. the Hβ absorption line; Worthey & Ottaviani 1997) and metallicity-sensitive features (e.g. the [MgFe] index; González 1993, Thomas et al. 2003), which can be useful in breaking this degeneracy. At lower spectral resolutions the absorption features produced by massive stars, for example Balmer lines, can be weakened by coincident emission within a starburst galaxy. However, higher-order Balmer lines are less prone to this effect because the strengths of corresponding nebular Balmer emission lines strongly decrease with decreasing wavelength (González Delgado et al. 1998). Therefore, a combined analysis of higher-order Balmer lines and other tracers may give an indication of the ages and metallicities of the dominant underlying stellar populations in a galaxy. To obtain a range of possible ages and metallicities in NGC 4449 we used the spectral fitting code STARLIGHT (v04; Cid Fernandes et al. 2005, Asari et al. 2007) and the global optical spectrum acquired by Kennicutt (1992). This analysis will provide a first indication of the star formation history, which will form basis for more detailed stellar population fitting in Section 2.3.7.

From the observed optical spectrum, sampled every 2 Å, we selected the range 3700–4900 Å for fitting, with the contaminating Balmer emission lines Hβ–Hη, as well as the unresolved [O II]$_{\lambda\lambda 3726,9}$ doublet and [Ne III]$_{\lambda 3869}$, masked out. We adopted 280 km s^{-1} for the global recession velocity by direct measurement from the observed spectrum, but the recession velocities are generally lower and vary as a function of position (Valdez-Gutiérrez et al. 2002). The observed internal velocity dispersion, on the other hand, is $\sim$30 km s^{-1} (Fuentes-Masip et al. 2000). Since the grating selected by Kennicutt (1992) offered a resolving power of only R $\sim$ 900, the velocity dispersion cannot be resolved by the observations and the code cannot take advantage of the more suitable high-resolution stellar spectra for fitting. Nevertheless, the distribution of stellar populations resulting from spectral fitting performed here is not sensitive to the assumed internal velocity dispersion.

We used the synthetic single stellar population (SSP) spectra of Bruzual & Charlot (2003) with R $\sim$ 2000, which were generated with the stellar initial mass function (IMF) of Chabrier (2003) and provided as part of the STARLIGHT package. This assumed IMF is very similar to and consistent with the IMF of Kroupa et al. (1991, 2001) adopted in this work. STARLIGHT was run with 12 sets of 5–99 stellar templates, or 'bases', to probe the star formation history at different sampling resolutions of age and metallicity. The lower and upper limits of the stellar ages were 1 Myr and 12 Gyr and 1–3 metallicities, corresponding to 0.2–1.0 Z$_\odot$, were tested at a time. One of the fits is presented in Fig. 2.3.

Our fits showed a significant spread in age–metallicity pairs at high resolutions of age and metallicity. Therefore, in Table 2.3 we present a summary of the fitted populations, grouped into 'young', 'intermediate' and 'old' and based on results from all fits. Table 2.3 shows that the most metal-poor populations are relatively well constrained and represent almost all of the stellar mass in NGC 4449. We find no evidence for a significant mass of stars with metallicities above 0.2Z$_\odot$ amongst the old ($\gtrsim$ 1 Gyr old) population. Based on our results, we estimate the first onset of star formation at approximately 12 Gyr ago. Because STARLIGHT tended to select the oldest available template for the oldest population, we emphasise that this result is approximate and onset epochs ranging from 10 Gyr ago to the age of the Universe should be considered equally plausible. Our results also consistently point to an age of 400 $\pm$ 100 Myr as being representative for the intermediate population.

These results are supported by the resolved stellar population study of Annibali et al.

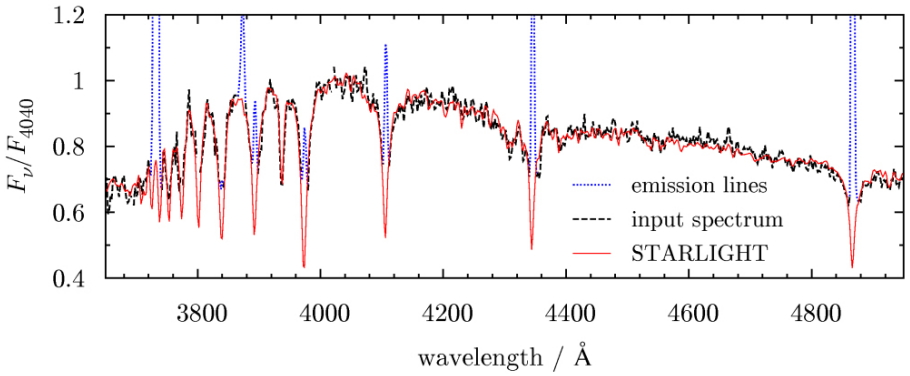

Figure 2.3. One of 12 STARLIGHT fits, in the range 3700–4900 Å, to the global spectrum of NGC 4449 acquired by Kennicutt (1992). The input spectrum (black line) was decomposed using 33 different stellar ages at $Z/\mathrm{Z}_\odot = 0.2$. Contaminating emission lines in the observed spectrum, shown in blue, were masked out. See text for more details.

	Mass fraction by age of stellar population		
Metallicity	Young ($\lesssim 10$ Myr)	Intermediate ($\sim 10^2$ Myr)	Old ($\gtrsim 10^3$ Myr)
$0.2\mathrm{Z}_\odot$	1%	20–25%	60–75%
$0.4\mathrm{Z}_\odot$	$< 2\%$	2%	
$\mathrm{Z}_\odot$	$< 1\%$	$< 7\%$	

Table 2.3. Summary of results from STARLIGHT fits to the global spectrum of NGC 4449 acquired by Kennicutt (1992). The figures show the percentages of the total mass of stars contributed by populations in the given age and metallicity bin.

(2008), suggesting continuous star formation activity for at least 1 Gyr, and by the results of Bothun (1986), who estimated that the underlying old stellar component has a mean age of 3–5 Gyr. A very young population of stars, on the other hand, is inferred from the presence of Wolf-Rayet stars (Martin & Kennicutt 1997).

Therefore we assume that star formation started not later than ~ 4 Gyr ago and continued until very recently or continues to the present day. We also assume three continuous star formation episodes. This assumption reduces the complexity of the model, and, at the same time, hints at a possible star formation history. The continuous-episode approach can be viewed as a generalisation of a starburst approach, which is discussed in Section 2.4.1.

2.3.5 Interstellar dust

Distribution and composition

The dust distribution is assumed to follow that of the gas, with the dust to gas mass ratio (abbreviated here as DGR or $M_{\rm dust}/M_{\rm gas}$) initially kept constant throughout the galaxy (however see, e.g. Bianchi 2008, Baes et al. 2010, MacLachlan et al. 2011, Schechtman-Rook et al. 2012, De Looze et al. 2012). We assumed two dominant dust species: amorphous carbon (Hanner 1988) and silicates (Laor & Draine 1993). To limit the number of free variables in the model, we further assume a constant mass ratio of carbonaceous dust to silicaceous dust (hereafter referred to as the carbon-to-silicate ratio) as a function of position. In what follows, we intend to illustrate explicitly the evolution of the carbon-to-silicate ratio for a galaxy continuously forming stars to allow us to fix this ratio for NGC 4449. We refer the reader to Dwek (1998), Morgan & Edmunds (2003), Galliano et al. (2008a) and Dwek & Cherchneff (2011) for more complete studies of dust evolution in the ISM.

The refractory dust in the ISM is believed to form in the outflows from asymptotic giant branch stars (AGB stars; e.g. Matsuura et al. 2009 for the LMC), in type II core-collapse supernova (CCSN) ejecta (e.g. a multi-epoch study of SN 2004et by Fabbri et al. 2011), and has also been suggested to form in molecular clouds (Draine 2009). Dwek (1998) has suggested that low-mass AGB stars are the main source of carbon dust, while type II SNe are the main source of silicate dust. Thus, the relative abundance of carbon and silicate dust depends on the dynamics of dust formation by AGB stars and supernovae, and on dust destruction processes and thus on the lifetimes of individual dust species.

Our calculations assume the dust yields of Ventura et al. (2012) for AGB stars, a constant and continuous star formation activity (Section 2.3.4, above), a constant metallicity, the initial mass function (IMF) of Kroupa et al. (1991, 2001) for stellar masses $1.5\ {\rm M}_\odot < M < 40\ {\rm M}_\odot$, and ignore dust destruction processes including consumption by ongoing star formation.

It is informative to first consider a flat distribution of yields across all SN masses and the carbon-to-silicate ratio inferred for SN 1987A by Matsuura et al. (2011; Model 1). Fig. 2.4 shows the carbon-to-silicate ratio for a galaxy actively forming stars for a continuous period of 4 Gyr. Since the data of Ventura et al. (2012) do not include AGB stars of mass lower than $1.5\ {\rm M}_\odot$, our models cannot be reliably extrapolated beyond the first 4 Gyr. At early times, the carbon-to-silicate ratio is fixed by the assumed dust composition of SN ejecta. When the SN dust dominates the global dust budget, the ratio is not expected to change significantly with time (Fig. 2.4, left, red solid line). If AGB dust dominates dust production, the carbon-to-silicate ratio initially decreases after ~ 40 Myr due to the predicted injection

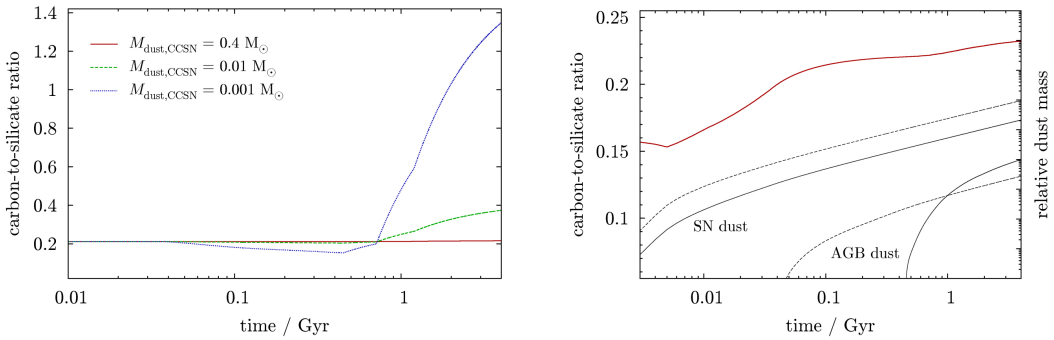

Figure 2.4. A simple model of the evolution of the global relative carbon to silicate dust content of NGC 4449, assuming continuous star formation and a constant metallicity $Z/\mathrm{Z}_\odot \sim 0.1$. The left panel shows the evolution of the carbon-to-silicate ratio for supernova dust yields identical to those derived by Matsuura et al. (2011) for SN 1987A (solid line), adopting their lower limit of $M_{\rm dust} = 0.4$ M$_\odot$ and a carbon-to-silicate ratio of 0.21 (their Model 1). Similar models with dust masses scaled to 0.01 M$_\odot$ (dashed line) and 0.001 M$_\odot$ (dotted line) are also presented, where the 0.001 M$_\odot$ model may be viewed as one where core-collapse supernovae are not important in global dust production. The right panel shows the evolution of the carbon-to-silicate ratio for supernova dust yields based on the elemental yields of Woosley & Weaver (1995; solid line). The thin solid and dashed lines show, respectively, the relative masses of carbon and silicate dust produced.

of silicates by super-AGB stars. After $\sim$400 Myr, less massive AGB stars begin injecting carbonaceous dust leading to carbon-dominated ISM dust after $\sim$1 Gyr (Fig. 2.4, left, blue dotted line).

A more realistic model includes variations in dust mass production as a function of CCSN progenitor mass, based on CCSN element yields of Woosley & Weaver (1995). Since the metallicity assumed by Ventura et al. (2012) is $Z/\mathrm{Z}_\odot = 0.05$, we chose the closest $Z/\mathrm{Z}_\odot = 0.1$ ^{56}Ni-producing models from Woosley & Weaver (1995) for all stellar progenitor masses, thus ignoring fallback of heavy elements (Moriya et al. 2010). We further scaled the CCSN elemental yields by a constant factor of 0.2 to bring the predicted dust masses into approximate agreement with the dust masses inferred from a range of supernovae (Wesson et al. 2010; Temim et al. 2006; Barlow et al. 2010; Matsuura et al. 2011; Gomez et al. 2012b). This scaling factor may be physically interpreted as the adopted condensation efficiency of dust. As amorphous olivine is observed to dominate the silicate mass in the diffuse ISM (Kemper et al. 2004), we assumed silicate stoichiometry of $MgFeSiO_4$ for calculations of silicate dust masses.

The results in Fig. 2.4 (right) show that the carbon-to-silicate ratio increases with time, owing to more carbon-rich dust being produced by lower mass SNe. This is strengthened at later times by carbon-rich dust contribution from the less massive AGB stars.

In this model a single metallicity of $Z/\mathrm{Z}_\odot \sim 0.1$ was assumed for the dust. However, the yields of Woosley & Weaver (1995) suggest that as metallicity increases, the relative production of carbon by CCSNe also increases. The opposite trend is suggested for AGB stars. In low metallicity environments AGB stars are expected to produce less silicates, while maintaining the same or an enhanced production of carbon dust (Sloan et al. 2006, 2012) than in higher metallicity environments. Since these trends operate on different time-scales, their combined effect is likely to result in a carbon-to-silicate profile which is more steeply increasing than the one shown in Fig. 2.4.

Therefore, given our assumptions about metallicity, the limited period of modelled star formation activity, and the uncertainty of the degree of dust enrichment by SNe, our final carbon-to-silicate mass ratio of 0.23 (Fig. 2.4, right) is likely to represent the lower limit of relative carbon content in a continuous star formation scenario. NGC 4449, with $\log(\mathrm{O/H}) + 12 = 8.23$, is similar in terms of metallicity to the LMC (Russell & Dopita 1992), whose dust content suggests a slightly higher carbon-to-silicate mass ratio of 0.33 (Weingartner & Draine 2001). If our model is allowed to evolve beyond the first 4 Gyr, the relative carbon content in NGC 4449 would be expected to match or exceed the LMC value, depending on the age of NGC 4449. This observation may warrant the use of metallicity-based assumptions about the carbon-to-silicate ratio in future studies. Therefore, given that our spectral fitting results discussed in Section 2.3.4 point to an early onset of star formation, we adopt the LMC carbon-to-silicate mass ratio of 0.33.

Grain size distribution

While the absence of distinct silicate emission features in the *Spitzer* Infrared Spectrograph (IRS) spectra (Section 3.2.1) may indicate a small abundance of Si, our chemical evolution models (Section 2.3.5, above) predict a non-negligible mass of silicate dust. If all dust is assumed to reside in a thin layer around the central ionizing source, this would impose an upper limit of 20 per cent on the mass fraction of Si in 'ultrasmall' silicate grains (< 15 Å; Li & Draine 2001) and suggest that the contribution of hot silicate dust to the global dust budget is relatively small (e.g. Smith et al. 2010). However, NGC 4449 is a face-on irregular galaxy and it is reasonable to assume, to a first-order approximation, that the radial distribution of dust follows the radial distribution of gas. Therefore, the absence of distinct silicate emission features in the global IRS spectrum may indicate effects resulting from geometry, for example extinguishing the emission from small grains by self-shielding.

We assume that the dust grain size distribution follows $n(a) \propto a^{-3.5}$ (Mathis et al. 1977) and we adopt the same range of grain sizes a between 0.005 μm and 0.25 μm for both amorphous carbon and silicates.

Polycyclic aromatic hydrocarbons

Prominent emission features in the mid-infrared, also known as the unidentified infrared bands (UIBs), are visible in the spectra of many types of objects, and are also detected in the *Spitzer* spectrum of NGC 4449 (Section 3.2.1). They are believed to originate from the C–H and C–C vibrations of large organic molecules, or polycyclic aromatic hydrocarbons (PAHs; e.g. Allamandola et al. 1985, Peeters et al. 2002, Bauschlicher et al. 2009). The relative strengths of these emission features are believed to reflect the particle size distribution and the local physical environment of the PAH molecules (e.g. Galliano et al. 2008b, Bauschlicher et al. 2009).

We assumed the mathematical description of pure ionized PAHs from Draine & Li (2007) with the grain size distribution of Weingartner & Draine (2001) for grain sizes of 3.5–30 Å. The PAH masses in this approach are not constrained by abundances (cf. Zubko et al. 2004). Since MOCASSIN currently allows only one grain size distribution per simulation, the PAHs have to be modelled separately.

2.3.6 Numerical setup

A series of preliminary simulations showed that the best compromise between high spatial resolution and reasonable computing time is obtained for a grid of $80 \times 80 \times 80$ cells, corresponding to 0.5 million grid cells. In a spherically symmetric setup, MOCASSIN uses a Cartesian x, y, z grid, with cells populating one octant of a sphere resulting in an eight-fold reduction of computing time for a given spatial resolution. The grid cells were not equal in size, and the resolutions used were 15 pc, 50 pc and 185 pc for the inner 0.5 kpc region, intermediate radii up to 2.5 kpc, and for outer radii, respectively. The number of grid cells and the resolutions ensure adequate sampling of the gas density profile (Section 2.3.2) as a function of radius. A single ionizing source, describing the stellar content of the entire galaxy, was placed at the origin of the coordinate system. The physical inner and outer radii of the galaxy were defined as 1 pc and 3300 pc.

The computation time for a single gas and dust simulation resulting from the setup described in this work was $\sim$9 h using 8 CPUs with 8 GB of RAM per CPU.

2.3.7 Variables and convergence criteria

As described in Section 2.3.1 and shown in Fig. 2.2, the three variables, the global bolometric luminosity $L_\star$, the DGR and the assumed star formation history (SFH), are iteratively adjusted until all observables are well matched. Of these, $L_\star$ is the most independent and can be fixed at early stages of the modelling.

The DGR and the SFH are not independent, as a higher dust content increases the extinction at the UV and optical wavelengths and therefore requires more ionizing photons to maintain the observed continuum levels. The SFH in itself is a multi-dimensional function, which can be explored to reach the most probable solution. We use the general picture of the SFH emerging from Section 2.3.4 as a constraint for constructing trial three-episode star formation scenarios. The steps described below may be viewed as an attempt to minimise a multi-dimensional mathematical expression by examining its partial derivatives locally.

The bolometric stellar luminosity $L_\star$

A large fraction of all the energy emitted by a starburst galaxy comes from the youngest and most massive stars. These stars contribute to the observed UV and optical continuum and govern the observed global ionization states of species present in the ISM. The same radiation field is also partially absorbed by the interstellar dust and re-radiated thermally in the IR. The degree of ionization of nebular species and the degree of reprocessing of radiation are also dependent on the clumpiness of the ISM.

Therefore, by focusing initially on the youngest stellar component and considering a representative set of star formation scenarios it is possible not only *(i)* to further simplify the SFH by constraining this youngest component, but also *(ii)* to fix the filling factor ϵ, *(iii)* to fix $L_\star$ and *(iv)* to provide an initial estimate for the DGR. Two main constraints, namely, the absolute level of the UV continuum and the 'recent' star formation rate (SFR) as traced by Hα or a similar tracer, must both be matched by the total stellar luminosity and the average age of the youngest population given the adopted filling factor.

The 'recent' star formation rate for NGC 4449 is estimated at $\sim 0.5\ \mathrm{M_\odot\ yr^{-1}}$ (Hunter et al. 1986, 1999) for a Salpeter IMF (Salpeter 1955; see discussion in Section 2.3.7). Since Dopita

et al. (2006) showed that for a SSP all ionizing photons are emitted within 10 Myr, we adopt 10 Myr, the lifetime of O- and B-type stars with masses $\gtrsim 13$ M$_\odot$, as a representative period of continuous star formation for the youngest stars.

The trial star formation histories (here also referred to as 'scenarios') were generated using STARBURST99 (Leitherer et al. 1999; v6.0.2) with the IMF of Kroupa (Kroupa et al. 1991, 2001), along with the Pauldrach/Hillier model atmospheres (Smith et al. 2002), the updated Padova AGB tracks (Vázquez & Leitherer 2005) and an assumed single constant metallicity of $Z/\mathrm{Z}_\odot = 0.4$ (cf. Table 2.3).

For a representative set of scenarios consisting of three star formation episodes, we first varied the degree of clumpiness, represented by ϵ, to allow enough gas to be ionized and produce the observed nebular emission line intensities (Kobulnicky et al. 1999) to within a factor of a few. We found that $\epsilon = 0.033$ is most representative, which corresponds to an average n_e of 41 cm^{-3} within the modelled ionized region. This choice is discussed further in Section 2.4.3.

We constructed a grid in parameter space formed by a representative set of scenarios consisting of three star formation episodes, a range of SFRs of the youngest population which is continuously forming stars for a period of 10 Myr, and a small range of initial values for $L_\star$ and the DGR. The predictions were then compared with observations. In particular,

1. the predicted UV continuum level was compared with the observed SED (Table 2.2),
2. the estimated total number of ionizing photons, $Q(\mathrm{H}^0)$, was compared with that derived from the integrated Hα luminosity (Hunter et al. 1999) and
3. the predicted nebular emission line fluxes were compared with the measurements of Kobulnicky et al. (1999).

The best-fitting models were found by minimising residuals between the model and the observations in a way similar to χ^2 minimisation. At this stage of modelling more weight was given to line intensities and to the level and shape of the continuum in the UV. To reduce the extent of the parameter space and the overall computation time, the iterative scheme in Fig. 2.2 was not allowed to advance automatically. Instead, after each iteration, candidate parameter sets were inspected to identify trends in each variable. The most promising parameter combinations were then manually expanded into a higher-resolution parameter space and iterated according to Fig. 2.2.

Our results suggest an on-going star formation activity with recent SFR ≈ 0.28 M$_\odot$ yr^{-1}, $L_\star \approx 5.7\times10^9$ L$_\odot$ and an initial DGR $\sim 1/250$, thus allowing us to fix the youngest population and $L_\star$. The empirical $L_\star$, computed by integrating measurements in Table 2.2 between 0.15 μm and 3.5 μm, is 3.1×10^9 L$_\odot$. This suggests that a significant fraction of the total luminosity originates from the recently formed massive stars.

The initial mass function

The recent SFR of 0.28 M$_\odot$ yr^{-1}, suggested by our initial models, is in good agreement with previous estimates (see below), when the revised distance of 3.8 Mpc (Annibali et al. 2008) and differences in the assumed IMFs are taken into account.

The Salpeter IMF, often used in the formulations of the SFR (e.g. Kennicutt 1998), is defined as $N(M)\ \mathrm{d}M \propto M^{-2.35}\ \mathrm{d}M$ (Salpeter 1955). However, the Kroupa IMF, which is

assumed in this work, is defined in two intervals, with a flatter distribution of the number of stars at lower stellar masses. Therefore, the Salpeter IMF will overestimate the number of lower-mass stars compared to the Kroupa IMF. This will in turn overestimate the total mass of stars resulting in a higher prediction of the SFR.

We generated distributions of stellar masses normalised to give the same number of stars at a stellar mass of 25 $M_\odot$, which we assumed to be representative of the population generating the ionizing photons and giving rise to the observed Hα emission. We computed the total mass of stars from $N(M)M\ \mathrm{d}M$ for $0.1 \leq M/M_\odot \leq 100$, which yielded a factor of 1.54 difference between the two IMFs. Assuming that the integrated luminosity of a galaxy scales linearly with the total mass, the SFRs based on the Salpeter IMF are therefore likely to be a factor of ≈ 1.5 higher than if the Kroupa IMF were used. This result is also evident from the results of Dwek et al. (2011a), who tabulate the masses of all stars born per one supernova event for a range of stellar IMFs.

Overall, our recent SFR of 0.28 $M_\odot\,\mathrm{yr}^{-1}$ is in good agreement with the distance-corrected and IMF-corrected estimates of 0.22–0.33 $M_\odot\,\mathrm{yr}^{-1}$ (Hunter et al. 1986), 0.30 $M_\odot\,\mathrm{yr}^{-1}$ (Hunter et al. 1999), and 0.21 $M_\odot\,\mathrm{yr}^{-1}$ (based on high ionization potential neon lines; Section 3.7).

Three episodes of star formation

To constrain $L_\star$ and the youngest stellar population, we assumed a representative older stellar component. Since the contribution of stars older than ~ 10 Myr to the ionization structure, to the number of ionizing photons, or to the far-UV continuum, is very small, the older populations can be studied in more detail without affecting the validity of our findings from Section 2.3.7.

The shape of the observed SED from the UV to the near-infrared (NIR) can be fitted by varying the lengths and characteristic epochs determining the remaining episodes of continuous star formation. Initially, we tested a set of 36 scenarios, which consisted of all combinations of:

1. three epochs corresponding to the onset of star formation (4, 8 and 12 Gyr ago),
2. four epochs corresponding to the transition between the first (old) episode and the second (intermediate) episode of star formation (100, 200, 400 and 1000 Myr ago),
3. three star formation rates ranging from 0.05 $M_\odot\,\mathrm{yr}^{-1}$ to 0.15 $M_\odot\,\mathrm{yr}^{-1}$ further defining the second episode.

The star formation activity during the third (young) episode remained fixed in both duration and magnitude, and $L_\star$ represented the luminosity of all stellar components, as described in Section 2.3.7. Therefore, the star formation rate of the first (oldest) episode was not an independent variable, but depended on $L_\star$ and the durations and star formation rates in items 1–3, for each scenario.

The resulting low-resolution SEDs were compared with the observed SED to select the best matches. Afterwards, following the scheme shown in Fig. 2.2, the transition epochs and the star formation rates inferred from the best matches were expanded into a narrower, but higher-resolution parameter space, analogous to conditions in items 2–3.

The criteria for finding the best-fitting combinations of stellar populations were similar to those used to find $L_\star$, where we minimised residuals between the model and the observations.

At this stage, more weight was given to the number of ionizing photons $Q(H^0)$, the line intensities and the level and shape of the entire stellar continuum from the UV to the NIR. As before, to reduce the extent of the parameter space and the overall computation time, the iterative scheme in Fig. 2.2 was not allowed to advance automatically. Instead, after each iteration, candidate parameter sets were inspected *(i)* to identify trends in each variable and *(ii)* to verify if the fit could be improved while still satisfying the observed number of ionizing photons $Q(H^0)$. The most promising parameter combinations were then manually expanded into a higher-resolution parameter space.

A two-zone solution for $M_{\rm dust}/M_{\rm gas}$ and modelling PAHs

NGC 4449 is modelled as a centrally-concentrated, spherically-symmetric galaxy, even though its morphology is highly irregular (cf. Fig. 2.1). Therefore, spherical symmetry inevitably misrepresents the interstellar radiation field (ISRF) within the galaxy. The single central source is much more luminous than any individual source in the real galaxy, as it must deliver enough energy to the correct mass of gas and dust to reproduce the observed strengths of the emission lines and the observed SED. Consequently, the conditions in the immediate proximity of the single central source result in unrealistically high ionization of the gaseous species and vaporisation of any existing dust grains. This effect is discussed in more detail in Section 2.4.3.

In order to fit the dust emission in the FIR, we divided the galaxy into two zones: an inner zone with a lower DGR and an outer zone with a higher DGR, which ensures realistic absolute masses of hot dust near the centre. For technical reasons this was preferred to an alternative approach, in which the radial distribution of dust density is defined directly through the MOCASSIN input parameter `Ndust`. We found that for larger systems, such as galaxies, defining dust distribution through `MdMg` gives best performance.

The best-fitting models were repeated with pure ionized PAH dust and the PAH grain size distribution (Section 2.3.5), and compared with the observed global SED (Table 2.2) and the global *Spitzer*/IRS spectrum (Fig. 3.3) to estimate the total mass of PAH molecules. In the final step, the resulting spectra were combined with the corresponding amorphous carbon and silicate models.

2.4 Results and discussion

2.4.1 Preliminary models

Our preliminary models included both starburst-only scenarios and continuous star formation scenarios. In the starburst-only scenario, a fit satisfying all observational constraints can be obtained for three representative starbursts occurring 3 Myr ago, 100 Myr ago and 4 Gyr ago, contributing to the total stellar mass in a ratio 1:200:1000. These models were later generalised by replacing starbursts with longer star formation episodes. For a scenario assuming two continuous star formation episodes the inferred star formation rates were ~ 0.25 $M_\odot\,yr^{-1}$ and ~ 0.09 $M_\odot\,yr^{-1}$ between ~ 6 Gyr ago and ~ 120 Myr ago, and ~ 120 Myr ago and the present day, respectively. The star formation history in these models was constrained only by the observed SED and by the observed emission line intensities. We note that the representative populations and star formation rates are not too dissimilar to the assumptions

Parameter	Value	Comments
	Numerical setup	
geometry	3D, spherically-symmetric	
grid size	$80 \times 80 \times 80$	ionizing source at $(x, y, z) = (0, 0, 0)$
number of photons	2×10^8	over all wavelengths
	Observationally constrained parameters	
physical radius	3.3 kpc	
gas distribution	exponential-like	derived from the H I profile of Swaters et al. (2002)
$M_{\rm gas}$	0.55×10^9 M$_\odot$	computed for $0 \leq r \leq 3.3$ kpc; molecular gas not included
filling factor (ϵ)	0.033	
chemical elements	H, He, C, N, O, Ne, S	abundances constant throughout galaxy
$Q(\mathrm{H}^0)$	4.84×10^{52} s^{-1}	based on $L_{\mathrm{H}\alpha}$ (Hunter et al. 1999)
	Adopted dust characteristics	
dust composition	amorphous carbon and silicates (1:3)	Hanner (1988); Laor & Draine (1993)
dust grain sizes	0.005–0.25 μm (20 sizes)	Mathis et al. (1977)
PAH grain sizes	3.5–30 Å (10 sizes)	PAHs modelled separately; Weingartner & Draine (2001)
	Best-fitting parameters	
$L_\star$	5.7×10^9 L$_\odot$	
$M_\star$	$1.05 \pm 0.15 \times 10^9$ M$_\odot$	
$M_{\rm dust}$	$2.9 \pm 0.5 \times 10^6$ M$_\odot$	including PAH grains
$M_{\rm PAH}$	$0.058 \pm 0.005 \times 10^6$ M$_\odot$	ionized PAH grains; Draine & Li (2007)
$M_{\rm dust}/M_{\rm gas}$	1/190	effective; 1/1000 in centre, 1/182 otherwise

Table 2.4. Summary of the input parameters and the results from the best-fitting MOCASSIN model of NGC 4449.

described in Section 2.3.4 and the recent star formation rate of 0.28 M$_\odot$ yr^{-1} (Section 2.3.7). Therefore, it may be argued that combining the three convergence criteria, namely, *(i)* matching the observed SED, *(ii)* matching the total observed rate of ionizing photons, $Q(\mathrm{H}^0)$, and *(iii)* matching the observed nebular emission line fluxes, may give informative results, even for a relatively simplified model.

2.4.2 Final model

Fig. 2.5 shows the best-fitting MOCASSIN model of NGC 4449 satisfying the observational constraints over the entire wavelength range from the UV to sub-mm. The individual SEDs arising from the assumed three continuous star formation episodes are also shown for comparison. The input parameters and the results are summarised in Table 2.4 and the details of the best-fitting parameters describing the star formation history are given in Table 2.5.

The three episodes of star formation shown in Fig. 2.5 suggest that most of the UV emission,

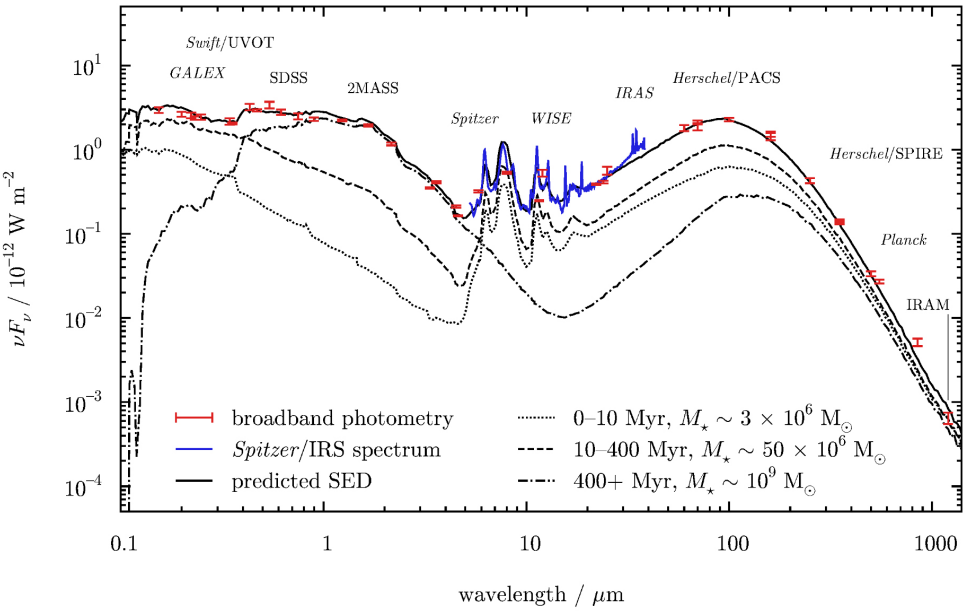

Figure 2.5. SED of the best-fitting MOCASSIN model of NGC 4449. The three star formation episodes were modelled simultaneously, but their individual SEDs are also shown for comparison. The photometric measurements have been corrected for foreground extinction, and the mid-IR spectrum acquired with *Spitzer*/IRS is discussed in detail in Chapter 3.

and most of the processed radiation emitted in the FIR, originates from the intermediate-age stars of ages between 10 and $\sim$ 400 Myr. The stars produced in the first episode, i.e., those older than $\sim$ 400 Myr, dominate in the optical and in the NIR. The youngest stars of ages less than 10 Myr contribute mainly in the far-UV.

Additionally, Fig. 2.6 shows the effects of varying the input parameters for the same best-fitting model (red solid line). For example, the effect of varying $L_\star$ is a vertical shift of the predicted SED in the stellar part (Fig. 2.6, top panel) and a corresponding change in $Q(\mathrm{H}^0)$, as the IMF-weighted distribution of stellar luminosities is scaled by a constant.

The predicted and observed global emission line intensities, relative to Hβ, are shown in Table 2.6. The discrepancies between the predicted and the observed nebular line intensities of some species, most notably [S II], result from the simplifying assumptions about the geometry and the degree of clumpiness, and are discussed in Section 2.4.3. Because the current version of MOCASSIN offers no treatment of PDRs, the PDR line [O I] in Table 2.6 is underpredicted. However, MOCASSIN is in the process of being expanded to accommodate PDRs via the recently developed three-dimensional PDR code 3D-PDR (Bisbas et al. 2012).

Stellar populations

In our three-episode model a stellar mass of $\approx 1 \times 10^9$ M$_\odot$ is produced at rates 0.25–0.10, 0.14 and 0.28 M$_\odot$ yr^{-1} over three periods, as shown in Table 2.5. The best-fitting SED in Fig. 2.5 shows that this model does not fully account for the emission between 7000 Å and 2 μm, which may be a result of the assumption of only three episodes of star formation with a constant SFR for the duration of each episode. However, we note that a non-trivial three-dimensional dust distribution, where the degree of obscuration does not follow the distribution of gas or stars, may have a significant effect on the observed attenuation (e.g. Witt et al. 1992, Baes

& Dejonghe 2000).

We found that the results are degenerate for the oldest stars and therefore the first onset of star formation 4, 8 or 12 Gyr ago is equally plausible, resulting in a range of predicted star formation rates. The spectral fits performed with STARLIGHT and discussed in Section 2.3.4 suggest an onset 12 Gyr ago or earlier. For an onset of star formation 12 Gyr ago, the average star formation rate for the duration of the first episode is 0.09 $M_\odot\,yr^{-1}$. Because the mass of recently formed stars is small in comparison (cf. Tables 2.3 and 2.5), it is possible that up to 95 per cent of the total stellar mass $M_\star$ in NGC 4449 was produced at higher instantaneous rates in an initial starburst.

The predicted onset of the second episode, 300–400 Myr ago, coincides with a possible encounter with the galaxy DDO 125 400–600 Myr ago (Theis & Kohle 2001). Given the simplifications of our model it would be difficult to quantify the effects of this postulated encounter on star formation rates. However, we note that our STARLIGHT fits (Section 2.3.4) select a population $\sim$400 Myr old as being representative for the intermediate-age populations. Similarly, the three-episode MOCASSIN fits to the observed stellar SED converge to 300–400 Myr ago as the transition epoch between the first episode and the second.

Our model suggests that in the last 10 Myr star formation has been taking place continuously at an average rate of 0.28 $M_\odot\,yr^{-1}$ (0.42 $M_\odot\,yr^{-1}$ assuming Salpeter IMF; Section 2.3.7). This recent SFR, obtained by fitting both the UV continuum and the emission lines (Section 2.3.7), is consistent with other estimates based on the UV continuum emission (0.44 $M_\odot\,yr^{-1}$; using data in Table 2.2 and following the formalism of Kennicutt 1998) or emission line intensities (Hunter et al. 1986, Hunter et al. 1999, Section 3.7).

The FIR emission arises from dust heated by stars and can also be used to estimate the recent SFR. Integrating the best-fitting SED in Fig. 2.5 between 8 and 1000 μm yields $I(\mathrm{FIR}) \approx 3.6\times10^{-12}$ W m^{-2}. The corresponding recent star formation rate is 0.28 $M_\odot\,yr^{-1}$ assuming a Salpeter IMF (Kennicutt 1998), which is significantly lower than the estimate of 0.44 $M_\odot\,yr^{-1}$ based on the UV emission. Indeed, the ratio SFR(FIR)/SFR(UV) for NGC 4449 based on the data in Table 2.2, and on the fit presented in Fig. 2.5, is 0.28/0.44 = 0.64, suggesting that approximately 35 per cent of the UV radiation does not contribute to the heating of dust. This UV 'leakage' (e.g. Relaño et al. 2012) is observed also in Haro 11 and NGC 4214 (Cormier et al. 2012; Hermelo et al. 2013), and may result from porosity of the ISM or different distributions for the stars and dust.

The low ratio SFR(FIR)/SFR(UV) may also suggest that, globally, in NGC 4449 the dust is heated by younger stellar populations. Similarly, a spatially-resolved study by Galametz et al. (2010) suggests that the distribution of cooler dust within a different dwarf galaxy, NGC 6822, may be correlated with star formation activity. In spiral galaxies, on the other hand, several studies suggest that the dust is heated by both the younger and the evolved stellar populations (e.g. Bendo et al. 2010, Boquien et al. 2011, Bendo et al. 2012a).

Interstellar dust

We infer a dust mass of $2.9 \pm 0.5 \times 10^6$ $M_\odot$ by making assumptions about the distribution of dust and its characteristics: the carbon-to-silicate ratio and the grain size distribution (cf. Section 2.3.5 and Table 2.4).

As explained in Section 2.3.7, in modelling the dust emission within NGC 4449 we adopted two zones with differing DGRs. Fig. 2.6 (middle panel) shows the two components, modelled

simultaneously, in green and blue. The combined effect of the best-fitting DGRs and the adopted distribution of gas (Section 2.3.2) is a relatively constant distribution of dust as a function of radius, varying by less than a factor of three between the centre and $r = 3.3$ kpc, and yielding $M_{\rm gas}/190$ within the modelled region. The need for two zones demonstrates that the actual distribution of dust is significantly different from the distribution of gas, even for one-dimensional azimuthally-averaged profiles. Fig. 2.6 also shows results for a smaller and a larger overall DGR, suggesting that the uncertainty in the best-fitting dust mass is $\sim 0.5 \times 10^6$ M$_\odot$.

The composition of dust has a major influence on the amount of attenuation produced at UV and optical wavelengths, and therefore on the total amount of dust required to reproduce the observed FIR emission. Fig. 2.5 shows that the photometric measurements agree with the model near the prominent absorption feature at 2175 Å, which is attributed to carbon dust (e.g. Fitzpatrick & Massa 1986). The *Spitzer*/IRS spectrum, on the other hand, is dominated by the PAH emission features and shows no discernible 10 μm silicate feature (Fig. 3.3), and no additional underlying component at 10 μm was needed to fit the PAH emission. Therefore, while appreciating that the assumed carbon-to-silicate ratio of 1:3 may be underestimated (also see discussion in Section 2.3.5), we conclude that the adopted ratio is consistent with observations. We find a contribution from PAHs to the total mass of dust of 2 per cent, which is consistent with the $M_{\rm PAH}/M_{\rm dust}$ ratios expected for a galaxy with 1/3Z$_\odot$ (Galliano et al. 2008a).

For comparison, in Fig. 2.6 (bottom panel, dotted line) we show the SEDs corresponding to different compositions of dust for the same total mass of dust. Additional carbon-rich dust (dotted line and dashed line) produces more emission in the FIR. If such carbon-rich compositions were used in fitting the SED, the overall required mass of dust would be lower. More silicate-rich dust (dot-dashed line), on the other hand, would increase the required mass of dust. Dust mass estimates in the literature range from 2.0×10^6 M$_\odot$ (Engelbracht et al. 2008) to 3.8×10^6 M$_\odot$ (Böttner et al. 2003), reflecting different properties of dust adopted in interpreting the FIR emission.

The metallicity of NGC 4449 is similar to that of NGC 1705 and NGC 6822 studied previously (O'Halloran et al. 2010; Galametz et al. 2010). However, the DGRs, in the range 1/80–1/186, derived for these galaxies are higher. The higher ratios may result from the assumption of pure graphite or pure amorphous carbon dust, and from the adopted gas and dust budget.

We note that the DGR of 1/190 was computed using the total derived dust mass for NGC 4449, while the model covered the inner radius of 3.3 kpc, the extent of the galaxy in the FIR, and as such took into account only about 25 per cent of the total observed gas (Section 2.3.2). If we considered only the gas present within the modelled region, that would require all metals in NGC 4449 to be locked into dust. However, NGC 4449 is a highly dynamic system, postulated to have been involved in a merger (Theis & Kohle 2001) and possessing a recently discovered companion (Rich et al. 2012). Since its optical body is not likely to be an isolated system, it is informative to include the extended H I envelope in the calculations, which yields a lower DGR of $\sim 1/760$. We also note that our gas masses do not include the mass of H_2 due to large uncertainties in the CO-to-H_2 conversion factors for low metallicity galaxies. Inclusion of an H_2 mass of $\sim 1.7 \times 10^8$ M$_\odot$ could decrease the global DGR even further to $\sim 1/820$.

On the other hand, an elevated flux at 850 μm, visible in Fig. 2.5 and not matched by

	Episode 1 (Old)	Episode 2 (Intermediate)	Episode 3 (Young)
onset / yr ago	$4–12 \times 10^9$	$300–400 \times 10^6$	10×10^6
$M_\star$ / $M_\odot$	$\sim 10^9$	$\sim 50 \times 10^6$	$\sim 3 \times 10^6$
SFR / $M_\odot\,yr^{-1}$	0.25–0.10	0.14	0.28

Table 2.5. The best-fitting three-episode star formation history of NGC 4449 assuming Kroupa IMF. The assumed star formation activity is continuous, and the onsets of episode 2 and 3 coincide with the end of the preceding episodes.

the model, may suggest the presence of a significant mass of cold dust (e.g. Galliano et al. 2003). Correctly accounting for the sub-mm emission is likely to increase the total mass of dust, and consequently the DGR, and can be crucial for accurate dust mass determinations (e.g. Galametz et al. 2011).

Finally, the dust mass predicted by our model can be used to infer the fraction of metals locked into dust in NGC 4449. Adopting the total H I mass of 2.2×10^9 $M_\odot$ (cf. Swaters et al. 2002, Bajaja et al. 1994) and given the total dust mass of 2.9×10^6 $M_\odot$, the carbon-to-silicate ratio of 1:3, the LMC gas-phase C/O ratio of 0.5, the LMC gas-phase Si/O ratio of 0.29 (Russell & Dopita 1992) and the observed mean oxygen abundance O/H of 1.95×10^{-4} (Vigroux et al. 1987), we estimate that approximately 30 per cent of carbon, 16 per cent of oxygen and 14 per cent of silicon atoms are locked in the solid phase as carbon and silicate dust. These estimates are consistent with the efficiency of 0.12 implied for SN 2003 gd (Sugerman et al. 2006) and the efficiences expected in early-formed galaxies (Morgan & Edmunds 2003). They are also broadly consistent with the dust condensation efficiency of 0.2 adopted independently for the theoretical supernova yields tabulated by Woosley & Weaver (1995) in order to match the dust masses inferred for a number of supernovae (Section 2.3.5).

2.4.3 Spherical symmetry limitations

To achieve representative heating conditions in a spherical model, the numerical setup must allow for enough ionizing photons to interact with the correct mass of gas for a given strength of the averaged ISRF. The images in Fig. 2.1, as well as the *Hubble* Space Telescope observations of NGC 4449 presented by Annibali et al. (2008) and the study of its young stellar clusters by Reines et al. (2008) show a variety of distinct actively star-forming regions. A spherically symmetric model must reproduce not only the combined strength of the numerous individual sources, but also the average ionization structure resulting from the real three-dimensional distribution of these ionizing sources. As a consequence, the required strength of the central ionizing source may be slightly overestimated.

In general, Table 2.6 shows good agreement between the predicted optical and infrared emission line fluxes and the observations. Since the ISRF in our models falls with distance from the central source as $1/r^2$, good agreement with observations can only be achieved by modifying the clumpiness or physical distribution of individual atomic or molecular species.

For example, our results do not correctly predict the ionization structure of sulphur: lines from the higher ionization potential S^{2+} ion are systematically underpredicted whereas lines from the lower ionization potential S^+ ion are overpredicted. This discrepancy cannot be

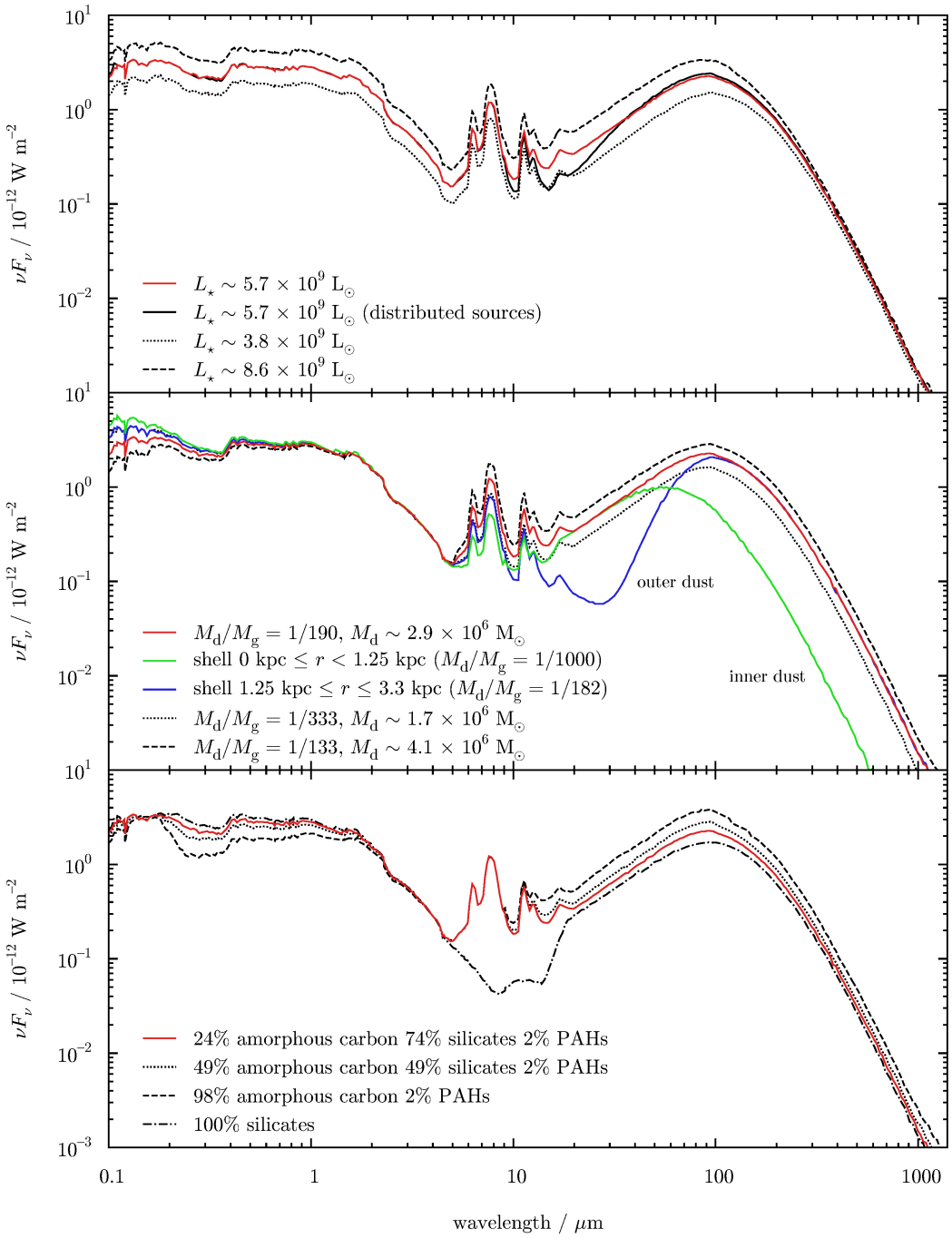

Figure 2.6. The effects of varying $L_\star$ (top panel), the DGR (middle panel) and the relative dust composition (bottom panel) on the predicted SED. While $L_\star$, the DGR and the distribution of the DGR were free variables in the models, the dust composition was fixed (Section 2.3.5) and its effect is presented here for illustration purposes only. The red solid lines represent the best-fitting model. See text for more details.

Line	Predicted $[I_{H\beta} = 1]$	Observed $[I_{H\beta} = 1]$	Ratio	References
[O II] λ3727	3.198	3.891	0.822	(1)
[Ne III] λ3868	0.173	0.189	0.916	(1)
Hδ λ4101	0.260	0.279	0.932	(1)
Hγ λ4340	0.469	0.492	0.953	(1)
Hβ λ4861	1.000	1.000	1.000	(1)
[O III] λ4959	0.699	0.689	1.015	(1)
[O III] λ5007	2.086	2.069	1.008	(1)
He I λ5876	0.079	0.079	1.000	(1)
[S III] λ6312	0.008	0.019	0.423	(1)
[N II] λ6548	0.102	0.115	0.892	(1)
Hα λ6563	2.922	2.866	1.020	(1)
[N II] λ6584	0.313	0.338	0.927	(1)
He I λ6678	0.022	0.028	0.798	(1)
[S II] λ6716	1.117	0.476	2.347	(1)
[S II] λ6731	0.784	0.334	2.349	(1)
[S IV] 10.5 μm	0.264	0.219	1.205	(2)
[Ne III] 15.6 μm	0.228	0.387	0.588	(2)
[O I] 63 μm	0.012	0.413	0.030	(2)
[O III] 88 μm	0.654	0.647	1.011	(2)
[C II] 158 μm	1.112	1.307	0.851	(2)

Table 2.6. Predicted and observed line strengths relative to Hβ and the predicted-to-observed ratio for the best-fitting MOCASSIN model of NGC 4449. References: (1) Kobulnicky et al. (1999); (2) Chapter 3.

explained by the assumed global abundances. However, the predicted relative sulphur line fluxes shown in Table 2.6 can be brought into very good agreement with observations by using a filling factor of $\epsilon = 0.055$ for sulphur in place of the lower global value of 0.033 adopted in this work. Physically, a smoother ISM shortens the mean free path of ionizing photons, increasing the degree of ionization within the modelled H II region. This result may suggest that the nebular emission in NGC 4449 originates from two or more gas phases with differing porosity, as well as from the transition zones between the phases. We conclude that a multi-phase gas model has to be invoked in our spherically symmetric approach in order to reproduce the details of the observed ionization structure (cf. Cormier et al. 2012).

2.4.4 Distributed ionizing sources

A more realistic ISRF can be obtained by replacing the single central ionizing source with a uniform distribution of sources forming a central 'ionizing sphere'. For this, we assumed a sphere with $r = 0.2$ kpc containing 100 identical sources, each contributing $L_\star/100$ to the total stellar luminosity.

Fig. 2.6 (top panel, black solid line) presents the predicted global SED resulting from the model with distributed ionizing sources. The SED is similar to the best-fitting model (red solid line), except for the range $\sim$10–30 μm, where the emission is weak in comparison. This discrepancy in the strength of the thermal emission by warm dust can be explained by the lower average photon energy available to interact with the dust in the case of distributed sources: dust in close proximity to one of the ionizing sources emitting with $L_\star/100$ is heated to much lower temperatures than is a relatively smaller mass of dust placed near a single

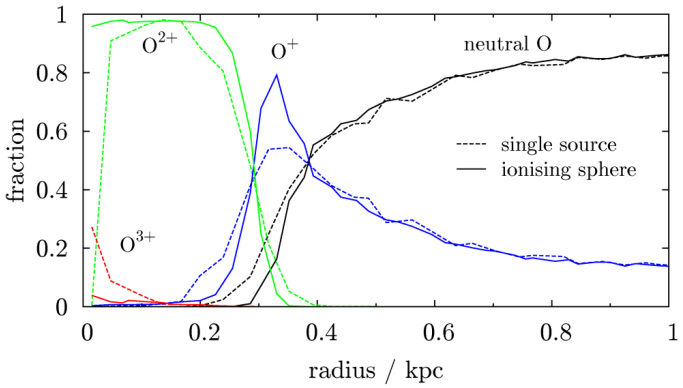

Figure 2.7. The ionization structure of oxygen as a function of radius for the inner 1 kpc in the best-fitting MOCASSIN model of NGC 4449 (dashed lines) and the corresponding structure for the single ionizing source replaced with 100 ionizing sources distributed uniformly within a sphere of $r = 0.2$ kpc (solid lines).

source emitting with $L_\star$.

The plots in Fig. 2.7 illustrate the corresponding differences in the ionization structure as a function of radius. For example, the overall ionization fraction of O^{2+} is significantly higher in the model with distributed sources, whereas the overall ionization fraction of O^{3+} is significantly lower. Since in this case the resulting integrated mass of O^{3+} is smaller, transitions of O^{3+} are likely to produce significantly lower line intensities. The opposite would be expected for O^{2+}. Indeed, in the distributed sources model shown in Fig. 2.7, the line fluxes predicted for the [O III] lines were approximately 5 per cent higher, while the flux of the $[O\,II]_{\lambda3727}$ line was 10 per cent lower than the corresponding fluxes in the single source model (Table 2.6). As discussed above, the key physical factors determining individual line intensities are the mean free paths to the ionizing source and the strength of that ionizing source. Therefore, in more realistic models with distributed sources, the input luminosity $L_\star$ would be expected to be lower by a few per cent to maintain good agreement between the predicted and observed line fluxes.

The physical distribution of ionizing sources affects the global ionization structure and, consequently, also affects the predicted line intensities, derived elemental abundances (cf. Ercolano et al. 2010) and may affect the overall stellar luminosity $L_\star$. Therefore, we note that performing line fitting of global emission lines is a valuable constraint on the overall properties of a galaxy, but may not be meaningful without taking the morphology into consideration.

2.5 Conclusions

In this work, we used results from previous studies, the available multiwavelength data, the spectral fitting code STARLIGHT and a simple chemical evolution code to construct a photoionization and radiative transfer MOCASSIN model of NGC 4449 through an iterative scheme.

We assumed a simplified star formation history consisting of three continuous episodes. Using the shape of the observed SED, the observed rate of ionizing photons, $Q(H^0)$ derived

from $L_{\mathrm{H}\alpha}$, and the observed nebular emission line fluxes as criteria in our scheme, we infer 3×10^6 $\mathrm{M}_\odot$ for the youngest stellar population (0–10 Myr old), which corresponds to an average recent star formation rate of 0.28 $\mathrm{M}_\odot\,\mathrm{yr}^{-1}$ or 0.42 $\mathrm{M}_\odot\,\mathrm{yr}^{-1}$, assuming a Kroupa IMF or a Salpeter IMF, respectively. We infer a bolometric stellar luminosity of 5.7×10^9 $\mathrm{L}_\odot$ generated by a total stellar mass of $\approx 1 \times 10^9$ $\mathrm{M}_\odot$. Although the ages of the oldest stellar populations in NGC 4449 are not well constrained by the model, we note that a very early onset, 12 Gyr ago or earlier, is selected by an independent analysis using the spectral fitting code STARLIGHT. A more in-depth study of stellar absorption line diagnostics at higher spectral resolutions would be necessary to reach more definite conclusions about these older populations.

We modelled the entire stellar component self-consistently along with a mixture of carbon and silicate dust. Our model yields a dust mass of $2.9 \pm 0.5 \times 10^6$ $\mathrm{M}_\odot$, which includes 2 per cent of PAHs. This estimate of M_{dust} could be lower, if a higher proportion of carbon-rich dust is assumed. Overall, the results from our chemical evolution model for a galaxy continuously forming stars are consistent with the carbon to silicate dust mass ratio of 1:3 inferred for the LMC (Weingartner & Draine 2001). Interestingly, the dust condensation efficiency emerging from our MOCASSIN model and from the observed abundance of oxygen in NGC 4449 is comparable with the value of 0.2 adopted independently in our chemical evolution model to match the dust masses inferred for a range of supernovae.

We note that a DGR of 1/190 was derived for the modelled region with a radius of 3.3 kpc. Including the extended H I envelope and the molecular gas is likely to lower the DGR to $\sim 1/800$. Similarly, our model does not account for cold dust, which may be responsible for an excess at 850 μm. Taking this additional component into account may have a significant effect on the derived DGR.

We conclude that our iterative scheme is a new tool, which can be used to model both the dominant stellar populations and the dust content in a self-consistent way. Although significant degeneracies in the derived parameters are expected, they can be reduced by supplementary spectroscopic data.

In the case of an irregular object, such as NGC 4449, we note that the assumption of spherical symmetry may lead to a misrepresentation of the ISRF giving rise to unphysical conditions near the central ionizing source. In particular, our results have shown that a single ISM phase does not fully reproduce the observed ionization structure, while the assumption of a single DGR overpredicts the mass of warm dust, suggesting that the radial density profiles of dust and gas are significantly different.

Our scheme is easily expandable to three dimensions, and in future work a realistic distribution of ionizing clusters could be used together with a diffuse evolved stellar population component and several gas and dust phases to construct more detailed representations of galaxies. In Chapter 3 we present a map of the recent star formation rate derived from $[\mathrm{Ne\,II}]_{12.8} + [\mathrm{Ne\,III}]_{15.6}$, as well as spatially-resolved measurements of the densities of ionized and neutral ISM phases, which may be useful in constructing a three-dimensional model of NGC 4449 in the future.

3 The interstellar medium of NGC 4449 as probed by Spitzer and Herschel

The Herschel data products described in Section 3.2.2 were provided by the Dwarf Galaxy Survey (DGS) collaboration (Madden et al. 2013).

3.1 Introduction

The atoms, molecules and dust particles within a galaxy together form the interstellar medium (ISM). In Chapter 1 we described some of the tools which may be used to study the ISM. In particular, spectroscopic observations allow us to determine *(i)* the abundances and the degree of ionization of individual elements, *(ii)* the physical properties of the ionized and neutral gas, *(iii)* the quality of the interstellar radiation field (ISRF), and *(iv)* the details of the heating and cooling processes in the ISM.

The *Spitzer* InfraRed Spectrograph (IRS; Houck et al. 2004) and the *Herschel* Photodetector Array Camera and Spectrometer (PACS; Poglitsch et al. 2010) have gathered a wealth of spectroscopic data at wavelengths from ~ 5 μm to ~ 210 μm at an unprecedented spatial resolution, allowing an in-depth analysis of star-forming regions (e.g. Galametz et al. 2013). Fig. 3.1 illustrates the wide range of environments, in terms of the ionized gas density and the hardness of the ISRF, which can be probed by both instruments.

In this work we analyse the available *Spitzer* and *Herschel* observations to describe the H II regions, the PDRs and the balance of heating and cooling within NGC 4449.

3.2 Observations and data reduction

NGC 4449 has been observed in the mid-infrared (MIR) by *Spitzer* and in the FIR by *Herschel*. The MIR observations of NGC 4449 completed with the *Spitzer*/IRS are discussed in Section 3.2.1. The observations in the FIR with *Herschel*/PACS integral field unit (IFU) are discussed in Section 3.2.2. A journal of observations is given in Table 3.1.

3.2.1 Spitzer/IRS spectroscopy

NGC 4449 was observed by the *Spitzer*/IRS as part of a nearby galaxy survey with Programme ID 50550 (PI: Frédéric Galliano). Mapping-mode observations in the Short-Low (SL) and Long-Low (LL) modules cover the spectral range from 5.2 to 38 μm. The spatial coverage of the observations is shown in Fig. 3.2.

We used the standard cube extraction tool CUBISM (v1.8, calibrations as of 2010-12-22) to construct four data cubes resulting from spectroscopy in the first and second spectroscopic orders. The dedicated sky observations linked to the on-target map of NGC 4449 consist of

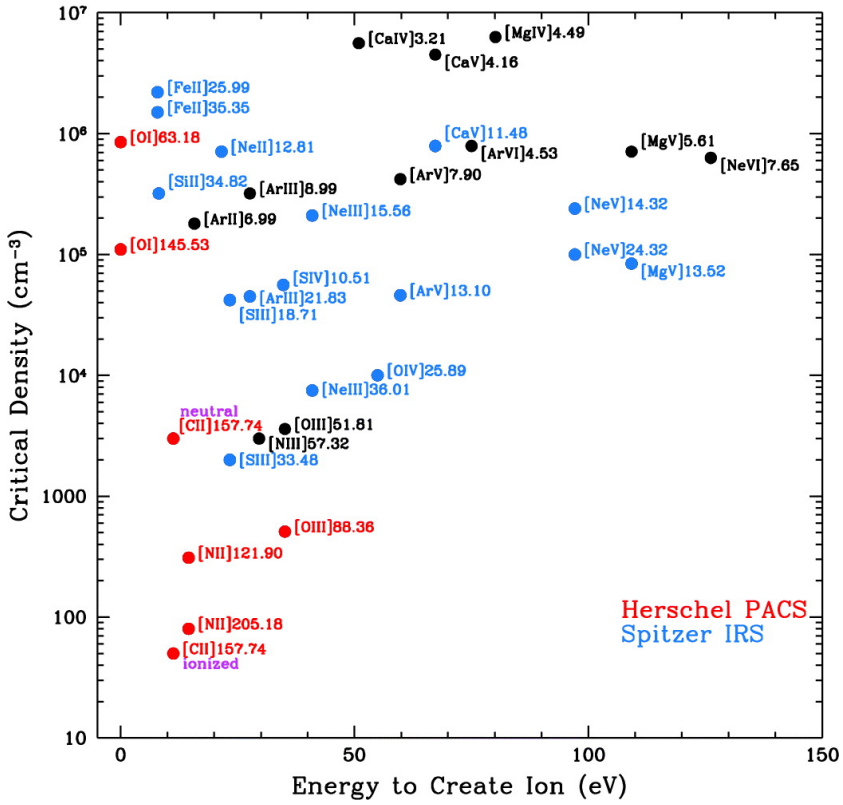

Figure 3.1. Ionization potentials and critical densities for selected diagnostic emission lines. Lines observable by *Spitzer*/IRS are in blue, lines observable by *Herschel*/PACS are in red and the remaining lines are in black. Reproduced from Kennicutt et al. (2011).

Instrument	Wavelength range	$t_{\rm exp}$ / s	Date observed	Observation ID
Herschel/PACS	55–210 μm	12741	2011 June 26	1342223138
				1342223139
				1342223140
				1342223141
				1342223142
				1342223143
		13738	2010 June 06	1342197813
				1342197814
Spitzer/IRS	5.2–38 μm	12777	2008 June 08	26396928

Table 3.1. List of spectroscopic observations with *Spitzer* and *Herschel*. Observations with *Herschel*/PACS were completed in two complementary sets, as explained in Section 3.2.2.

one slit position in each module and, due to high noise levels, were found unsuitable to use for background subtraction. Instead, a number of off-target slit positions from the on-target map were selected to create a sigma-trimmed average background. Bad pixels were removed using the tools available within CUBISM.

The observations in the SL module, covering the wavelength range 5.2–14.7 μm, consist of an array of 40 × 5 slit positions observed in a sequence, covering approximately 2′.9 × 5′.7 on the sky. Eight slit positions within the fifth column of 40 slit positions were used as background. A spectral cube of 158 × 77 × 77 [pixels × pixels × wavelength bins] was constructed for observations in the SL2 subslit (second spectral order of the SL module). Similarly, a cube of 158 × 77 × 117 was constructed for SL1. To improve the overall S/N, two columns of pixels on either side of the extraction area were excluded, and the global spectra were extracted from the physical area of 123 × 77 pixels.

The observations in the LL module, covering the wavelength range 14.3–38.4 μm, consist of 20 × 2 slit positions observed in a sequence, covering approximately 4′.4 × 6′.0 on the sky. Spectral cubes of 68 × 41 × 75 and 68 × 41 × 100 were constructed for observations in the subslits LL2 and LL1. Only one column of 20 slit positions was used for spectrum extraction in each case, and, to improve the overall S/N, one column of pixels on either side of the extraction area was excluded. The extracted physical area was 33 × 41 pixels. Six slit positions within the second column of 20 slit positions were used as background.

Fig. 3.2 shows the coverage of all subslit positions with respect to the 8 μm broadband image of the galaxy (*Spitzer*/IRAC AOR 4467456, channel 4).

The extracted SL and LL portions of the resulting global spectrum were multiplied by a factor of 0.762 and 0.821, respectively, to integrate from average MJy/sr to Jy. These factors were calculated from $23.5 \times 10^{-6} \times (S)^2 \times A$, where S is the detector pixel scale (1″.85/pixel and 5″.08/pixel) and A is the extraction area in pixels.

Close examination of Fig. 3.2 suggests three effects which should be taken into account for accurate global spectroscopy. Firstly, the IRS observations may not cover the entire galaxy and this effect is noticeable particularly in the N and SW edges of the high-contrast 8 μm image of the galaxy. We used Starlink GAIA (v4.4.0) to estimate the percentage of the total galactic light at 8 μm falling within the extraction area for each subslit.

Secondly, background measurements from the slit positions on the sides of the galaxy may be contaminated by galactic light. Therefore, the resulting global spectrum may be

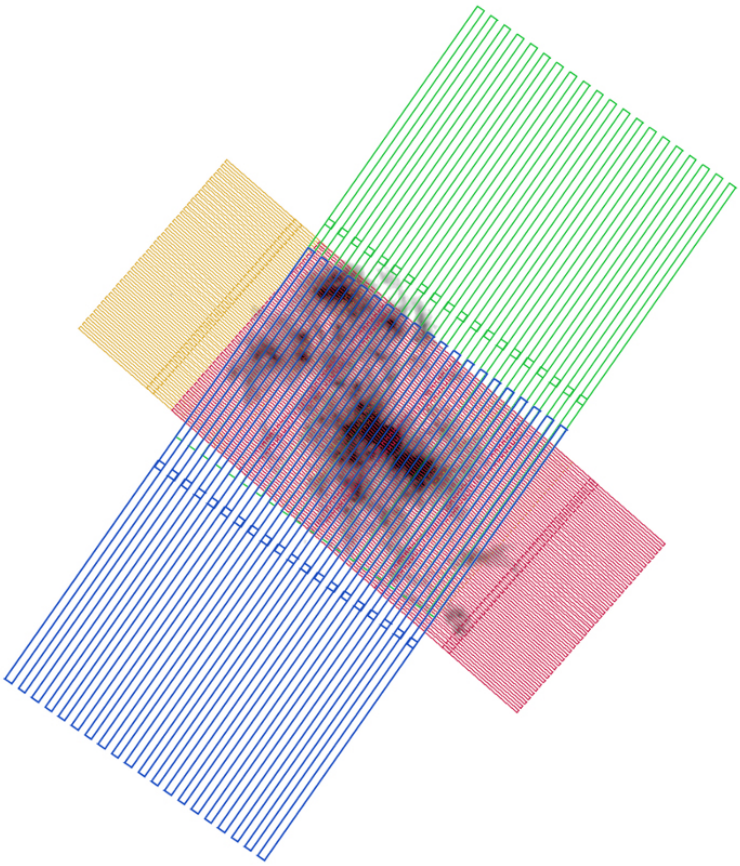

Figure 3.2. Spatial coverage of the *Spitzer*/IRS map of NGC 4449 with the broadband 8 μm image shown in greyscale for comparison. The coverage in the individual subslits SL2, SL1, LL2 and LL1 is indicated in yellow, red, green and blue. North is up, east is to the left.

overcorrected for background levels. We used the statistics tool in CUBISM and the 8 μm broadband image of the galaxy to compare the average background levels at the slit positions selected for background measurements with the average levels at distant sites in the field.

Finally, actual slit positions in the maps may not offer continuous coverage of the galaxy in the direction perpendicular to the slit. The gaps between slit positions visible in Fig. 3.2 illustrate sites where spatial information is not accurately preserved and do not necessarily imply a loss in flux. However, the fraction of flux lost due to gaps in slit coverage can be calculated by inspecting the individual slit positions. The difference in consecutive slit positions found in the FITS file headers is $4\farcs26$ (SL) and $13\farcs44$ (LL), which creates gaps of $0\farcs66$ (SL) and $2\farcs94$ (LL) per slit position.

The corrections applied to the extracted spectra are given as multiplicative factors in the table below, where $f_{\rm int}$ is the MJy/sr-to-Jy conversion factor, $f_{\rm map}$ is the correction for the fraction of the galactic 8 μm luminosity covered in the extraction area, $f_{\rm bkg}$ is the correction for background oversubtraction, $f_{\rm slit}$ is the correction for gaps in the slit coverage, and $f_{\rm tot}$ is the resulting overall correction for each subslit.

	$f_{\rm int}$	$f_{\rm map}$	$f_{\rm bkg}$	$f_{\rm slit}$	$f_{\rm tot}$
SL2	0.762	1.0634	1.021	1.1825	0.978
SL1		1.0583	1.082		1.032
LL2	0.821	1.0570	1.0035	1.2804	1.115
LL1		1.0630	1.0033		1.121

To check the reliability of the data reduction process we convolved the corrected global spectrum with the response function of the 8 μm IRAC band and the 24 μm MIPS band. The resulting fluxes are 1.44 $\pm$ 0.01 Jy in the simulated 8 μm IRAC band and 3.62 $\pm$ 0.02 Jy in the simulated 24 μm MIPS band, which is in good agreement with the observed fluxes of 1.42 $\pm$ 0.04 Jy and 3.29 $\pm$ 0.13 Jy, respectively (Engelbracht et al. 2008; Bendo et al. 2012b).

The resulting global, calibrated, corrected and smoothed (σ = 0.0425 μm) spectrum of NGC 4449 is presented in Fig. 3.3.

To perform a more detailed analysis we extracted spatially resolved spectral information from the four data cubes generated by CUBISM, corresponding to observations in the four modules (SL2, SL1, LL2, LL1). We used the IDL package CONV CUBE developed by S. Hony to *(i)* convolve spectral maps at every observed wavelength to the IRS instrumental point spread function (PSF) at 40 μm (FWHM $\approx 10''$), *(ii)* combine the four data cubes taking into account differences in orientation and overlapping spectral regions, and *(iii)* shrink the combined cube by removing pixels not covered across the entire spectral range. The resulting cube, rebinned to $5'' \times 5''$, consisted of 41×27 spatial pixels (spaxels), corresponding to the area $3\farcm4 \times 2\farcm2$ on the sky, and a spectral dimension of 285 wavelength bins sampled from every 0.03 μm at shorter wavelengths to every 0.2 μm at longer wavelengths.

Fig. 3.4 shows the spatial coverage of 154 spaxels with the average S/N per wavelength bin of 1.67 or better for 5.2 μm $\leq \lambda \leq$ 22 μm. Spectra observed in eight different environments are also shown. All 154 spectra were fitted by PAHFIT (Smith et al. 2007) to recover fluxes of individual spectral features at every position. As the fluxes at longer wavelengths in these spectra were associated with significantly larger uncertainties, the fits were limited to wavelengths up to 29 μm.

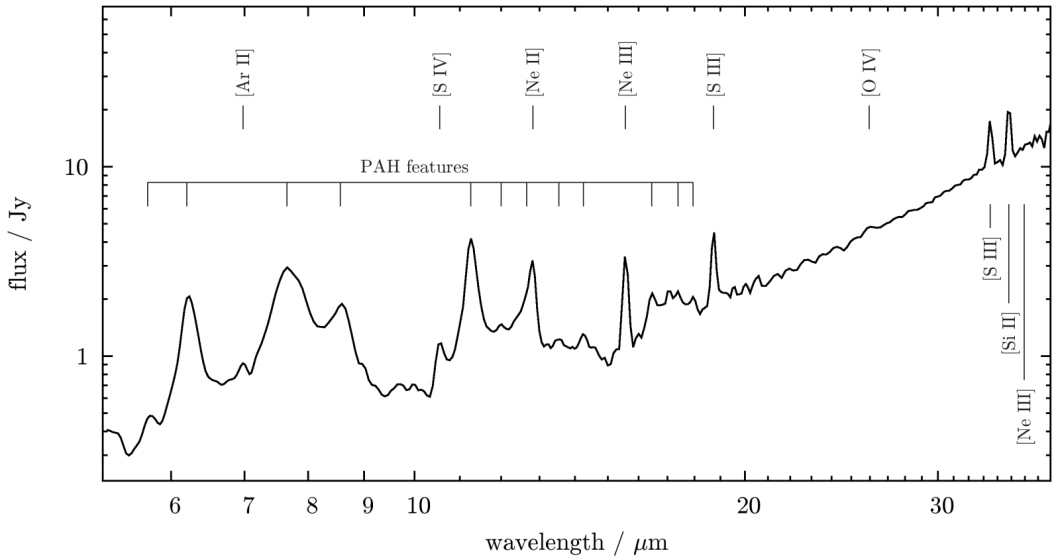

Figure 3.3. Global *Spitzer*/IRS spectrum of NGC 4449. The average statistical uncertainty of flux per wavelength bin is 1 per cent.

3.2.2 Herschel/PACS integral field spectroscopy

The spectroscopic observations in the FIR were completed as part of the *Herschel* Guaranteed Time Key Programmes: Dwarf Galaxy Survey (DGS; Madden et al. 2013) and Survey with Herschel of the ISM in Nearby INfrared Galaxies (SHINING; Sturm et al. 2011).

NGC 4449 was observed with the PACS spectrometer on 6 June 2010 (OD 388). The FIR fine-structure lines [C II]$_{158}$ (obsid 1342197813) and [O I]$_{63}$ (obsid 1342197814) were mapped in a 4 × 7 raster positions as a calibration test for the unchopped scan observing mode. The PACS array is composed of 5 × 5 spatial pixels (spaxels), with a total field of view of 47″ × 47″. Each raster pointing is separated by a step size of ∼1/2 of the array, offering a total map coverage of 3′.0 × 2′.2. The FWHM in the 'blue' band is ∼9″.5, corresponding to a physical scale of ∼180 pc, and ∼13″ in the 'red' band corresponding to ∼240 pc.

Follow-up observations were done on 26 June 2011 (OD 774). We obtained 2 × 3 maps towards the northern part of the galaxy, with step sizes of 34″ in the unchopped scan mode in the lines [C II]$_{158}$ (obsid 1342223143) and [O I]$_{63}$ (obsid 1342223141) to complete the earlier maps due to a misorientation of the test maps on the sky, and to obtain new observations in the [O III]$_{88}$ line (obsid 1342223142). An additional 2 × 2 map with step size 34″ was done in the chop-nod mode for the [O III]$_{88}$ line (obsid 1342223139).

Finally, 2 × 1 maps with step size 34″ were obtained in the unchopped scan mode in the lines [O I]$_{146}$ (obsid 1342223138) and [N II]$_{122}$ (obsid 1342223140) covering the nuclear region of NGC 4449. The spatial coverage of all maps is shown in Fig. 3.5.

The data were reduced in HIPE (Ott 2010), user release v4.0 for obsids 1342197813 and 1342197814, and v7.0 for obsids 1342223138–1342223143. We used standard pipeline scripts to produce Level 2 products. For the unchopped scan observations, we also applied a correction to remove transient effects as explained in Lebouteiller et al. (2012). Off-target spectra were averaged and subtracted from the on-target observations to remove background noise.

For obsids 1342197813 and 1342197814 no off-target observations were performed and we applied a fringe correction by fitting a sinusoidal function to the signal baseline. Since these

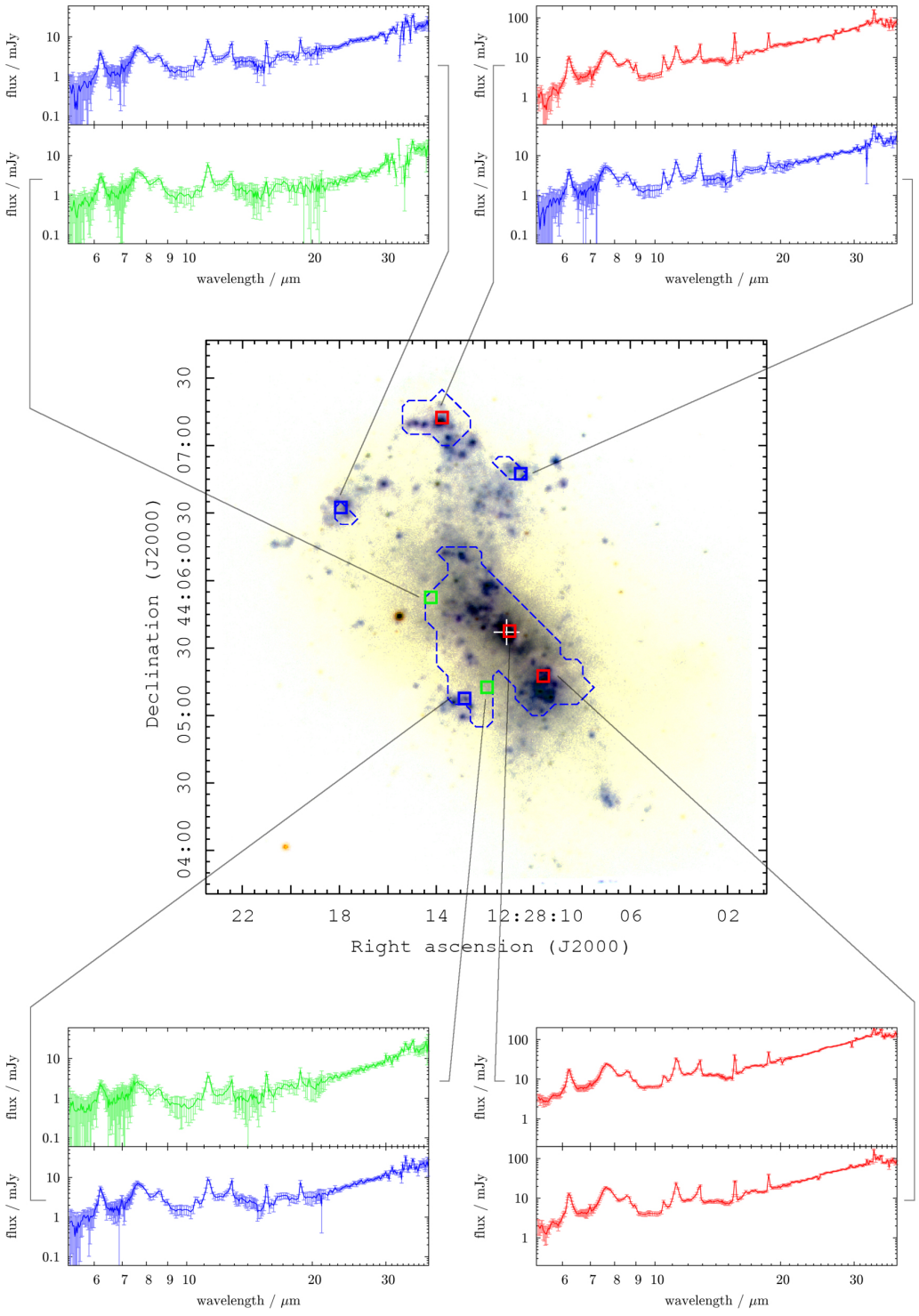

Figure 3.4. *Spitzer*/IRS spectra at eight selected positions within NGC 4449. The squares, corresponding to individual 5″ × 5″ spaxels, and the spectra are colour-coded, according to their average S/N per wavelength bin (S/N_{avg}). Spaxels with $S/N_{avg} \geq 1.67$ are in blue and those with $S/N_{avg} \geq 4.5$ are in red. The two spaxels in green correspond to two low surface brightness sites with $S/N_{avg} \approx 1.9$. The dashed blue contours enclose all 154 spaxels with $S/N_{avg} \geq 1.67$. A false-colour SDSS image is shown as background (Fig. 2.1) and the cross denotes the optical centre of the galaxy.

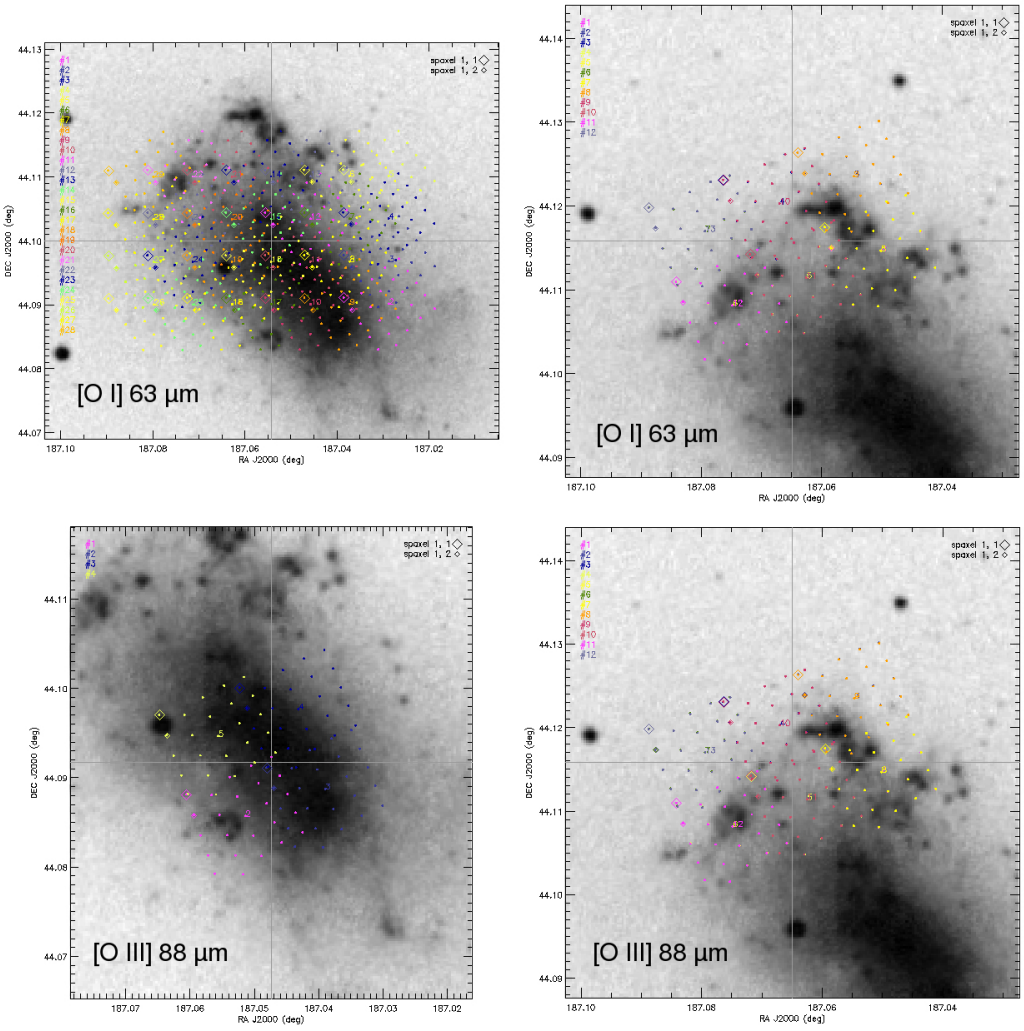

Figure 3.5. Spatial coverage of the *Herschel*/PACS maps of NGC 4449 with an optical SDSS image shown in greyscale. Symbols indicate individual IFU pointings. *(continued on next page)*

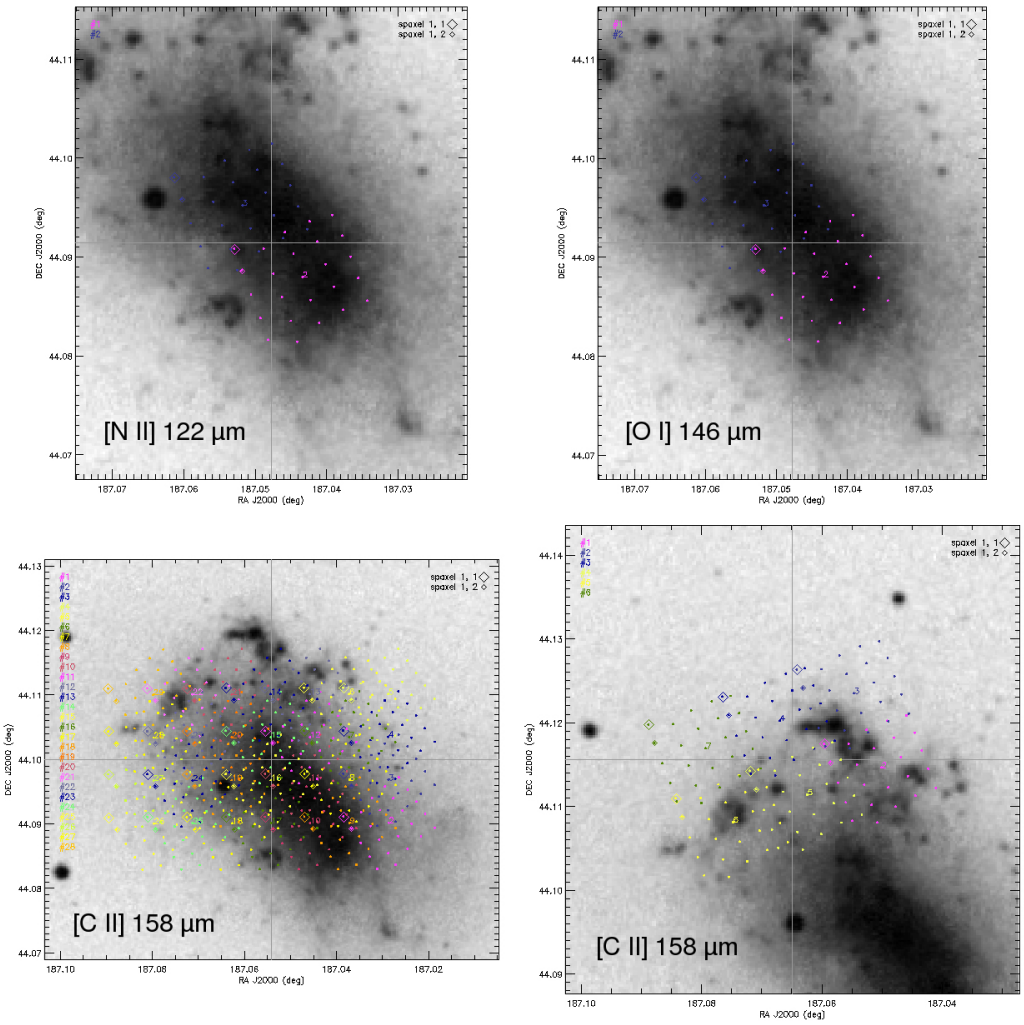

Figure 3.5. *(continued from previous page)*

data were reduced with an older version of HIPE, the spectra were further calibrated by dividing by a factor 1.1 and 1.3 for the 'blue' and 'red' band, respectively (Vandenbussche et al. 2011).

Spectral cubes for each raster position produced by HIPE were used with PACSman (Lebouteiller et al. 2012) to perform line fitting and to generate maps. Lines were fitted assuming Gaussian profiles and a second order polynomial.

3.3 Global mid-infrared spectrum of NGC 4449

The global *Spitzer*/IRS spectrum of NGC 4449 (Fig. 3.3) shows nebular emission lines, as well as emission features known as unidentified infrared bands (UIBs) and commonly attributed to PAHs (e.g. Allamandola et al. 1985, Peeters et al. 2002, Bauschlicher et al. 2009).

We used two methods to analyse the unsmoothed global spectrum of NGC 4449. Gaussian fitting was performed using Starlink DIPSO (v3.6-3). The derived fluxes for the nebular emission lines as well as the dust features are given in Table 3.2 ('Gaussian'). Blended features or features close together were fitted with multiple Gaussian components, otherwise a single Gaussian profile was assumed. We assumed a linear continuum locally, which is simpler than a constrained multi-component approach ('spline'; e.g. Hony et al. 2001; Peeters et al. 2002).

However, the spectrum does not show the underlying finer details of PAH emission revealed by high-resolution spectroscopy (e.g. Peeters et al. 2002) or predicted theoretically (e.g., Bauschlicher et al. 2008, 2009). The underlying PAH features can be fitted using Lorentzians (e.g. Boulanger et al. 1998) or Drude profiles (Smith et al. 2007). These techniques are similar and we used PAHFIT (Smith et al. 2007) as our second method of analysing the global spectrum ('PAHFIT' in Table 3.2).

Table 3.2 lists fluxes derived using both methods. Except for [S IV] and [O IV] the fluxes of nebular emission lines agree very well. However, the fluxes of the PAH features derived by PAHFIT are significantly higher than those derived by the Gaussian method, which is due to the differences in the assumed local continuum. Despite these differences, Galliano et al. (2008b) found that the two methods are strongly correlated and produce self-consistent results.

The recession velocity computed from the measured central wavelengths of the unblended lines [Ne III]$_{15.6}$ and [S III]$_{18.7}$ is 315 ± 4 km s^{-1}, which is greater than 207 km s^{-1} quoted by the NED (NASA/IPAC Extragalactic Database). This discrepancy is a result of the inadequate sampling of our low-resolution spectrum, which, together with the associated uncertainties, does not provide the required accuracy in central wavelength measurements.

3.4 Ionized regions

The four spectral cubes described in Section 3.2.1 were used with CUBISM to generate maps of selected nebular emission lines, which trace ionized regions. The line maps of [S IV]$_{10.5}$, [Ne III]$_{15.6}$, [S III]$_{18.7}$ and [Si II]$_{34.8}$ are shown in Fig. 3.6. We note that the maps extracted from the LL modules lack one row of spatial information due to a combination of undersampling and sky to detector mapping resulting from the slit orientation. Spectral data in the missing row are preserved and no flux losses occur beyond those explained and corrected for in Section 3.2.1.

	GAUSSIAN			PAHFIT			
$\lambda^{\star}_{\rm ref}$ [μm]	$\lambda_{\rm obs}$ [μm]	Flux [$10^{-14} \times$ W m^{-2}]	FWHM [μm]	$\lambda_{\rm obs}$ [μm]	Flux [$10^{-14} \times$ W m^{-2}]	FWHM [μm]	Identification*
5.270	...	...	...	5.274	0.521 ± 0.031	0.18	C–H bending + C–H stretch
5.700	5.714	0.46 ± 0.23	0.20	5.704	0.447 ± 0.021	0.20	C–H bending + C–H stretch
6.220	6.228	2.60 ± 0.13	0.19	6.224	4.55 ± 0.015	0.19	aromatic C–C stretch (in-plane)
6.690	...	...	...	6.695	1.18 ± 0.03	0.47	?
6.909	...	...	...	6.920	0.037 ± 0.008	0.058	H_2 $S(5)$
6.985	6.984	0.105 ± 0.022	0.066	6.988	0.094 ± 0.007	0.052	[Ar II]
7.417[a]				7.425	2.88 ± 0.07	0.94	aromatic C–C stretch
7.598[a]	7.682[†]	6.46 ± 0.15	0.56	7.605	5.01 ± 0.03	0.33	aromatic C–C stretch
7.850[a]				7.855	3.87 ± 0.02	0.42	C–C stretch + C–H bending
8.330	8.526[†]	2.49 ± 0.18	0.53	8.336	1.20 ± 0.01	0.42	C–C stretch + C–H bending?
8.610				8.616	2.41 ± 0.01	0.34	C–H bending (in-plane)
8.991	...	...	...	8.995	0.049 ± 0.002	0.090	[Ar III]
9.665	...	...	...	9.677	0.042 ± 0.002	0.11	H_2 $S(3)$
...	9.718	$\leq$ 0.67	0.8	...	...	...	9.7 μm broad silicate feature
10.51	10.54	0.329 ± 0.046	0.19	10.54	0.164 ± 0.002	0.11	[S IV]
10.68	...	...	...	10.69	0.140 ± 0.004	0.21	C–H bending (out-of-plane)
11.23[b]	11.25[†]	0.69 ± 0.15	0.16	11.24	1.37 ± 0.005	0.14	C–H bending (out-of-plane)
11.33[b]	11.28[†]	1.42 ± 0.14	0.36	11.34	2.26 ± 0.009	0.36	C–H bending (out-of-plane)
11.99	11.99	0.038 ± 0.010	0.11	12.00	0.757 ± 0.008	0.54	C–H bending (out-of-plane)
12.28	...	...	...	12.34	0.036 ± 0.002	0.11	H_2 $S(2)$
12.62[c]	12.66[†]	0.438 ± 0.078	0.33	12.63	1.41 ± 0.01	0.53	C–H bending (out-of-plane)
12.69[c]				12.70	0.266 ± 0.006	0.17	C–H bending (out-of-plane)
12.81	12.82[†]	0.485 ± 0.065	0.14	12.83	0.430 ± 0.002	0.11	[Ne II]

(continued on next page)

Table 3.2. Measurements of global emission line fluxes and dust features in the *Spitzer*/IRS spectral map of NGC 4449. Due to large uncertainties 1σ upper limits are given for the 9.7 μm silicate feature and [Ne III]$_{36}$. Individual features were fitted *(i)* by assuming Gaussian profiles and *(ii)* by assuming that PAH resonances can be described as Drude profiles (Draine & Li 2007) and by decomposing the spectrum with PAHFIT (Smith et al. 2007). *(continued on next page)*

	GAUSSIAN			PAHFIT			
$\lambda^{\star}_{\rm ref}$ [μm]	$\lambda_{\rm obs}$ [μm]	Flux [$10^{-14} \times$ W m^{-2}]	FWHM [μm]	$\lambda_{\rm obs}$ [μm]	Flux [$10^{-14} \times$ W m^{-2}]	FWHM [μm]	Identification*
(continued from previous page)							
13.48	13.54	0.047 ± 0.019	0.21	13.49	0.315 ± 0.008	0.54	C–H bending (out-of-plane)
14.19	14.26	0.084 ± 0.015	0.22	14.20	0.226 ± 0.006	0.36	C–H bending (out-of-plane)
15.56	15.57	0.580 ± 0.021	0.17	15.57	0.525 ± 0.004	0.15	[Ne III]
16.45	16.45†	0.203 ± 0.028	0.27	16.46	0.300 ± 0.010	0.23	C–C–C bending?
17.04	17.06†	0.049 ± 0.012	0.13	17.06	0.064 ± 0.007	0.13	H_2 $S(1)$
17.04^{d}	17.15†	0.629 ± 0.099	1.1	17.05	0.830 ± 0.041	1.1	C–C–C bending?
17.38^{d}	17.39†	0.032 ± 0.015	0.14	17.39	0.135 ± 0.009	0.21	C–C–C bending?
17.87^{d}	17.95†	0.064 ± 0.020	0.20	17.88	0.123 ± 0.008	0.29	C–C–C bending?
18.71	18.73	0.454 ± 0.018	0.17	18.73	0.419 ± 0.004	0.15	[S III]
18.92	...	...	...	18.93	0.196 ± 0.010	0.36	C–C–C bending?
25.89	25.96	0.074 ± 0.020	0.49	25.88	0.038 ± 0.005	0.37	[O IV]
25.99	...	...	...	26.06	0.032 ± 0.005	0.37	[Fe II]
28.22	...	...	...	28.22	0.011 ± 0.003	0.31	H_2 $S(0)$
33.10	...	...	...	33.12	0.336 ± 0.023	1.7	?
33.48	33.48†	0.669 ± 0.029	0.31	33.48	0.649 ± 0.005	0.31	[S III]
34.81	34.81†	0.789 ± 0.031	0.27	34.81	0.826 ± 0.007	0.31	[Si II]
36.01	35.95	$\leq$ 0.52	1	...	...	...	[Ne III]

* reference wavelengths for nebular emission lines as listed in the Atomic Line List (v2.04; van Hoof & Verner 1997); reference wavelengths and tentative identifications of PAH features as in Draine & Li (2007)

† in the Gaussian method, continuous fit with multiple Gaussian components over wavelengths 7.4–8.7, 11.2–12.9, 16.4–18.0 and 33.4–34.9 μm

^{a} 7.7 μm complex; integrated flux is 6.46 ± 0.15 (Gaussian) and 11.8 ± 0.1 (PAHFIT)

^{b} 11.3 μm complex; integrated flux is 2.11 ± 0.21 (Gaussian) and 3.63 ± 0.01 (PAHFIT)

^{c} 12.7 μm complex; integrated flux is 0.438 ± 0.078 (Gaussian) and 1.67 ± 0.01 (PAHFIT)

^{d} 17 μm complex; integrated flux is 0.73 ± 0.10 (Gaussian) and 1.39 ± 0.03 (PAHFIT)

Table 3.2. *(continued from previous page)*

In Fig. 3.7 we present a map of electron density n_e derived from the [S III]$_{18.7}$/[S III]$_{33.5}$ line intensity ratio. To improve accuracy we rejected pixels with the signal-to-noise (S/N) below 5. Because the S/N peaks near the brightest regions of the galaxy, the resulting coverage is significantly smaller than the FOV of individual line maps.

The electron densities corresponding to a range of values of $I_{18.7}/I_{33.5}$ were calculated using the UCL statistical equilibrium codes EQUIB and RATIO described by Kingsburgh & Barlow (1992, 1994) with the transition probabilities of Mendoza & Zeippen (1982) and the collision strengths of Mendoza (1983). A plot of the relationship between the electron density n_e and the ratio $I_{18.7}/I_{33.5}$ is shown in Fig. 3.8. To verify our predictions we compared our electron density derived from an integrated [S III] ratio, with the value derived from [S II]$_{\lambda6717}$/[S II]$_{\lambda6731}$ by Martin (1997) for the centre of NGC 4449. We extracted the average $I_{18.7}/I_{33.5}$ ratio and computed the corresponding n_e for an artificial 180″ slit mimicking that in Martin (1997). The derived n_e(S III) was 200 ± 45 cm^{-3}. This is slightly greater than n_e(S II) of 130^{+11}_{-12} cm^{-3} obtained by Martin (1997) for the same spatial configuration. However, we note that a difference is expected due to the different PSFs of the observations. To obtain the map presented in Fig. 3.7 the observations were degraded to a common PSF of 14″, which is much larger than a PSF of 2″ in the observations of Martin (1997). Thus, our result is representative of a larger physical area in the centre of NGC 4449.

The global electron density corresponding to $I_{18.7}/I_{33.5} = 0.679 \pm 0.040$ (Gaussian) and $I_{18.7}/I_{33.5} = 0.646 \pm 0.008$ (PAHFIT) from the data in Table 3.2 is 170 ± 60 cm^{-3} (Gaussian) and 120^{+12}_{-11} cm^{-3} (PAHFIT), respectively. These results are also consistent with ~ 200 cm^{-3} tabulated by Abel et al. (2005) for the same [S III] ratios. A higher electron density near the centre relative to the global value is consistent with the map shown in Fig. 3.7.

3.5 Photo-dissociation regions

PDRs are defined as regions lying between the ionized gas and the molecular clouds. They are illuminated by the FUV radiation in the range 6 eV $< h\nu <$ 13.6 eV, which is not enough to ionize hydrogen (13.6 eV), but sufficient to photo-dissociate molecular species, such as H_2 (4.5 eV; e.g. Stecher & Williams 1967). Therefore, PDRs are composed of primarily neutral atomic species and dust grains, including PAHs.

3.5.1 Polycyclic aromatic hydrocarbons

The PAH features visible in Fig. 3.3 are observed together across many types of objects. The variations in their relative strengths and relative shifts in wavelength can be used to probe the local physical conditions in the ISM. Their intensity ratios may be interpreted in terms of the properties of the PAH molecules (e.g. Galliano et al. 2008b), while the profiles of individual PAH bands may be attributed to the environment (e.g. Peeters et al. 2002). The *Spitzer*/IRS data shown in Fig. 3.4 cover a continuous range of wavelengths between 5.2 and 38 μm over an extended area on the sky, thus enabling a spatially resolved analysis.

Band ratios

To examine PAH emission the individual spectra at 154 sites shown in Fig. 3.4 were decomposed using PAHFIT. In Fig. 3.9 we present a map of integrated PAH emission constructed by summing the best-fitting PAHFIT intensities of the complexes centred at 6.2, 7.7, 8.6,

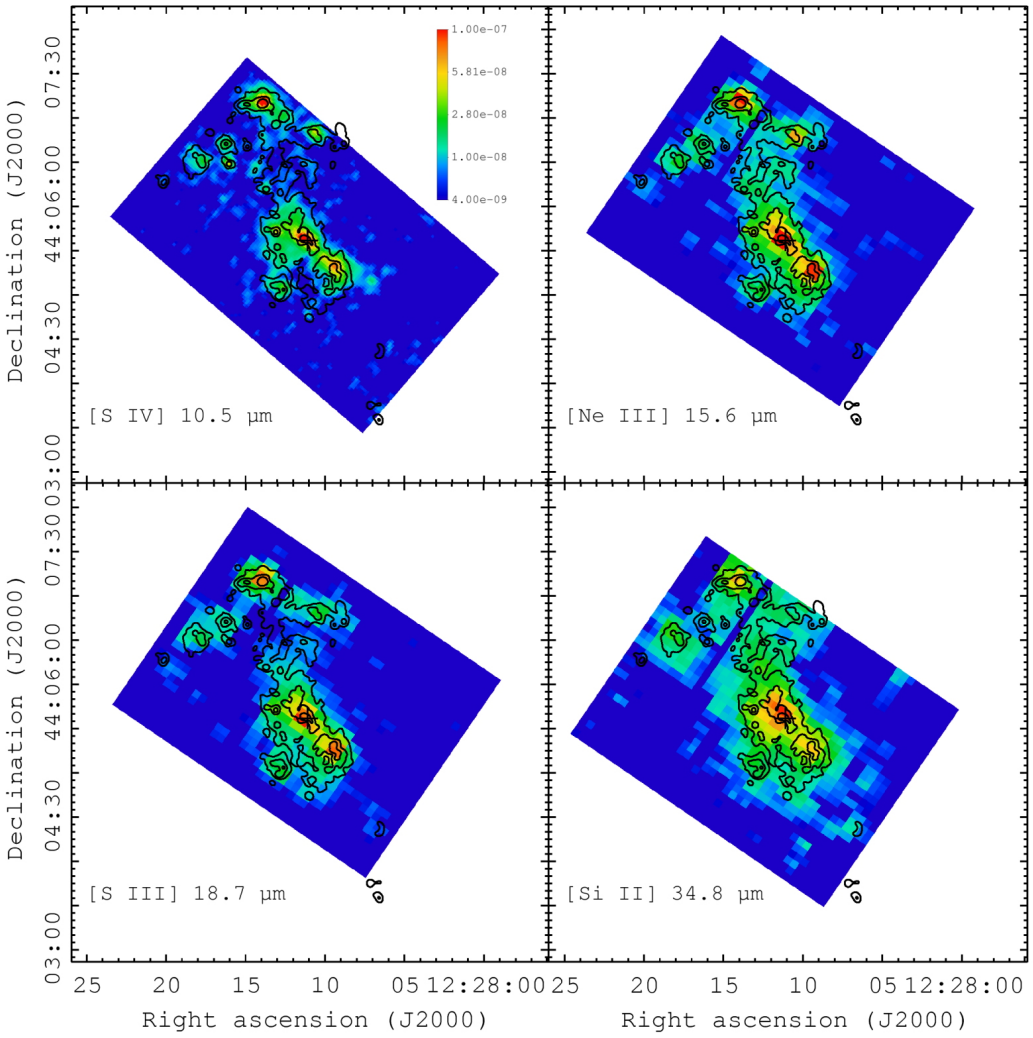

Figure 3.6. Maps of the nebular emission lines [S IV]$_{10.5}$, [Ne III]$_{15.6}$, [S III]$_{18.7}$ and [Si II]$_{34.8}$ observed by *Spitzer*/IRS and extracted with CUBISM. Emission line intensities are given in units of W m^{-2} sr^{-1}. Mean flux uncertainties are 20 per cent, except for the map of [Si II], where the mean uncertainty is 25 per cent. The FWHM of the telescope beam is 3″, 7″, 7″ and 9″, respectively, corresponding to approximately two pixels in diameter. Contours enclose the brightest 70, 40 and 16 per cent of the total Hα emission, and the cross denotes the optical centre of the galaxy.

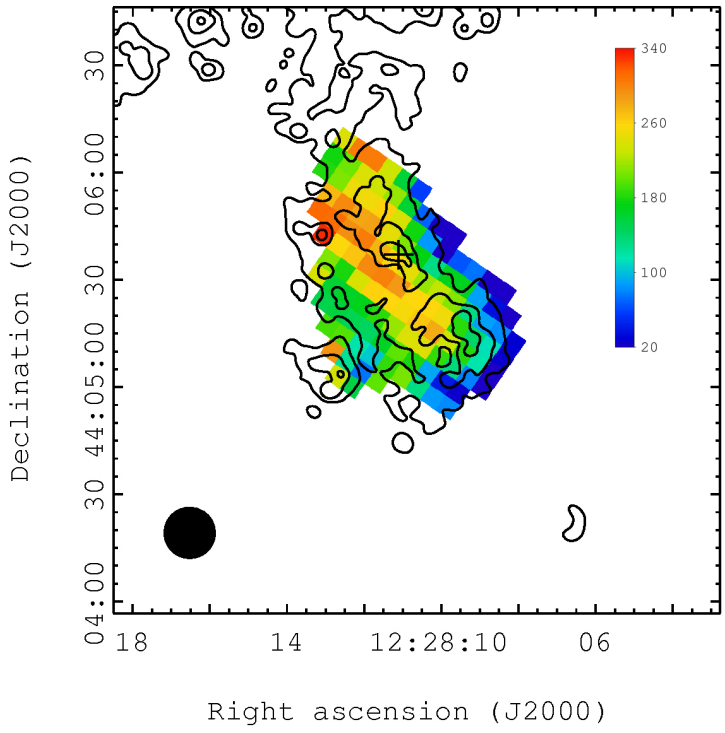

Figure 3.7. Map of electron density near the centre of NGC 4449 in units of cm^{-3} derived from the [S III]$_{18.7}$/[S III]$_{33.5}$ diagnostic ratio (the *Spitzer*/IRS map of [S III]$_{18.7}$ is shown in Fig. 3.6). The density uncertainty is 33 per cent in the outer pixels and 10 per cent in the inner pixels. The FWHM of this map is 14″ and is indicated by a filled circle. Contours enclose the total Hα emission, and the cross denotes the optical centre of the galaxy.

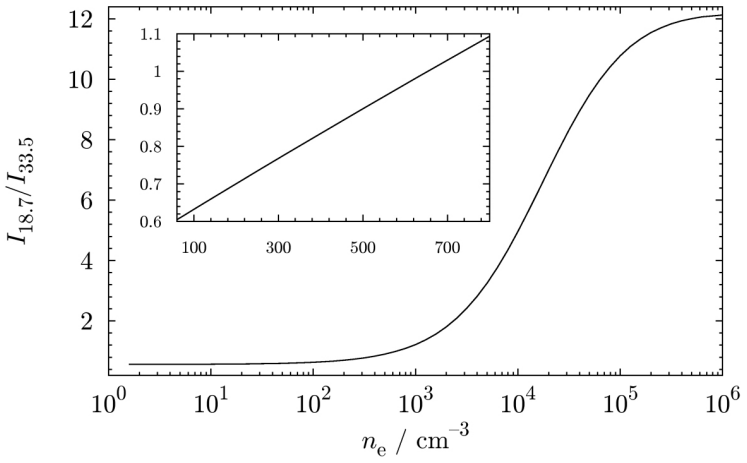

Figure 3.8. The ratio [S III]$_{18.7}$/[S III]$_{33.5}$ as a function of electron density n_e generated by the UCL code EQUIB with the transition probabilities of Mendoza & Zeippen (1982) and the collision strengths of Mendoza (1983). The assumed electron temperature was 10^4 K.

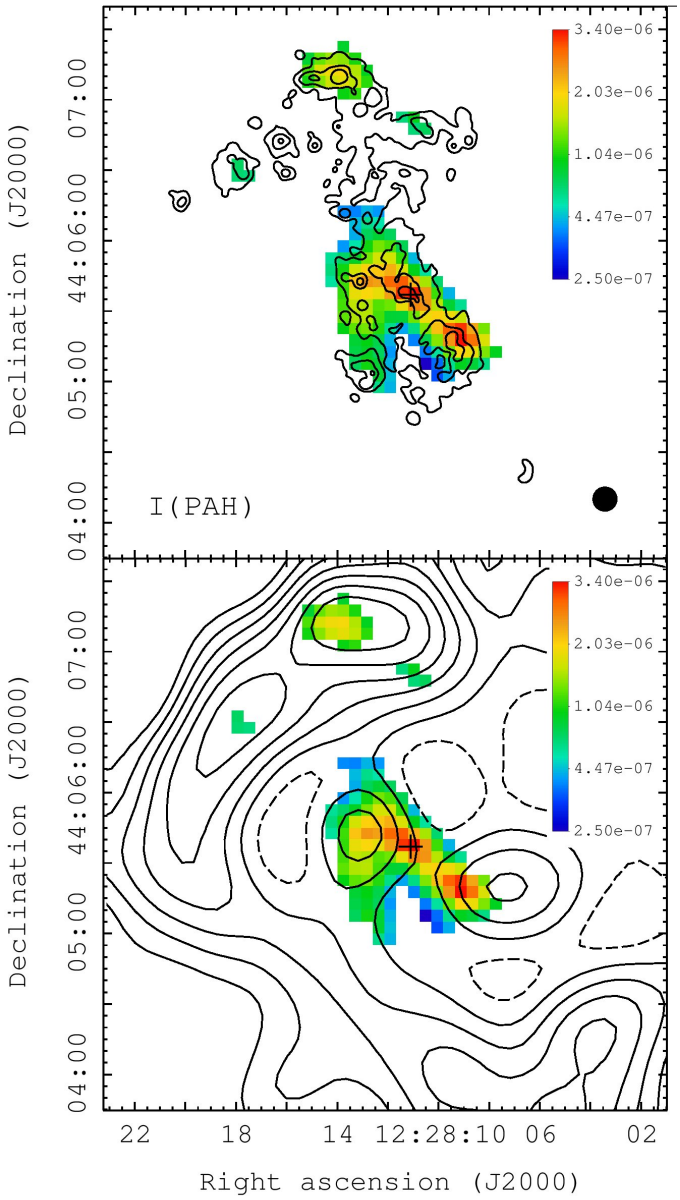

Figure 3.9. Map of integrated PAH emission obtained by summing the PAHFIT flux at 6.2, 7.7, 8.6, 11.3, 12.7 and 17 μm, with a mean total flux uncertainty of 7 per cent. The units are W m^{-2} sr^{-1}. In the top panel the contours enclose the brightest 70, 40 and 16 per cent of the total Hα emission. In the bottom panel the contours show the emission of H I 21 cm, where the dashed H I contours indicate minima. The FWHM of the maps is 10″ and is indicated by a filled circle. The cross denotes the optical centre of the galaxy.

11.3, 12.7 and 17 μm. Maps of the intensity ratios of individual PAH bands are presented in Fig. 3.10.

Our results show that at the resolution of $\sim$185 pc the peaks of the total PAH emission coincide with the peaks of Hα emission. The PAH band ratios, however, show a varied spatial behaviour:

- $I_{12.7}/I_{11.3}$ shows a correlation with Hα,
- $I_{7.7}/I_{6.2}$, $I_{8.6}/I_{6.2}$, $I_{12.7}/I_{6.2}$ and $I_{12.7}/I_{7.7}$ show some correlation with Hα,
- $I_{7.7}/I_{11.3}$ shows a correlation with the atomic gas (H I 21 cm) emission tracing the cold neutral phase of the ISM,
- $I_{6.2}/I_{11.3}$ and $I_{8.6}/I_{11.3}$ show some correlation with H I,
- $I_{17}/I_{6.2}$ and $I_{17}/I_{12.7}$ show an anticorrelation with H I.

The 6.2, 7.7 and 8.6 μm complexes can be attributed to the presence of ionized PAH molecules, while the 11.3 μm complex can be attributed to the presence of neutral PAH molecules (e.g. Bauschlicher et al. 2009). The ratios $I_{6.2}/I_{11.3}$, $I_{7.7}/I_{11.3}$ and $I_{8.6}/I_{11.3}$ in Fig. 3.10 show similar behaviour, supporting this distinction. Since the 7.7 and 11.3 μm complexes are among the brightest features in Fig. 3.3, $I_{7.7}/I_{11.3}$ is expected to correlate strongly with the presence of ionized PAH emission. Our results suggest that the ionized PAH emission originates from the N, E and SW parts of NGC 4449 and coincides with the peaks of the emission from atomic gas. Since the ionized PAHs, as traced by $I_{7.7}/I_{11.3}$, are located outside the centre of NGC 4449, the integrated emission near the centre shown in Fig. 3.9 arises from neutral PAHs along the line of sight but well outside the ionized regions. Therefore, the apparent correlation of the integrated PAH emission with Hα may result from the likely mixing of ISM phases at the linear scales of 185 pc.

The apparent correlation of $I_{7.7}/I_{11.3}$ with neutral gas may identify sites of active star formation, as traced by the column density of neutral gas (cf. Skillman et al. 1988). However, while the high-$I_{7.7}/I_{11.3}$ sites to the N, E and SW of the centre coincide also with the Hα emission, the Hα-bright centre of the galaxy shows a deficit in $I_{7.7}/I_{11.3}$. One possible explanation is that the hard ISRF near the centre (see Fig. 3.23) is more likely to destroy rather than ionize PAH molecules (e.g. Giard et al. 1994). However, Fig. 3.9 suggests a significant mass of PAH molecules coinciding with the optical centre of NGC 4449 and argues against this possibility. The low $I_{7.7}/I_{11.3}$ and the high overall PAH emission may therefore result from mixing of a considerable mass of neutral PAH molecules and a more localised mass of ionized PAH molecules at the resolution of our observations.

Another possibility is less efficient self-shielding in the PDRs and deeper penetration of FUV photons in the N, E and SW, where the high $I_{7.7}/I_{11.3}$ ratios are observed. This hypothesis could be verified by accurate metallicity and abundance determinations, if the N, E and SW sites are found to be lower in metallicity, and therefore lower in dust abundance, than the optical centre (cf. Madden et al. 2006).

Other PAH band ratios are less definite in their interpretation. The enhanced ratio $I_{8.6}/I_{6.2}$ to the W of the centre may be interpreted as arising from larger ionized PAH molecules. The 12.7 μm emission, on the other hand, is centrally-peaked in NGC 4449 and is believed to arise from irregular PAH molecules (e.g. Hony et al. 2001, Bauschlicher et al. 2009).

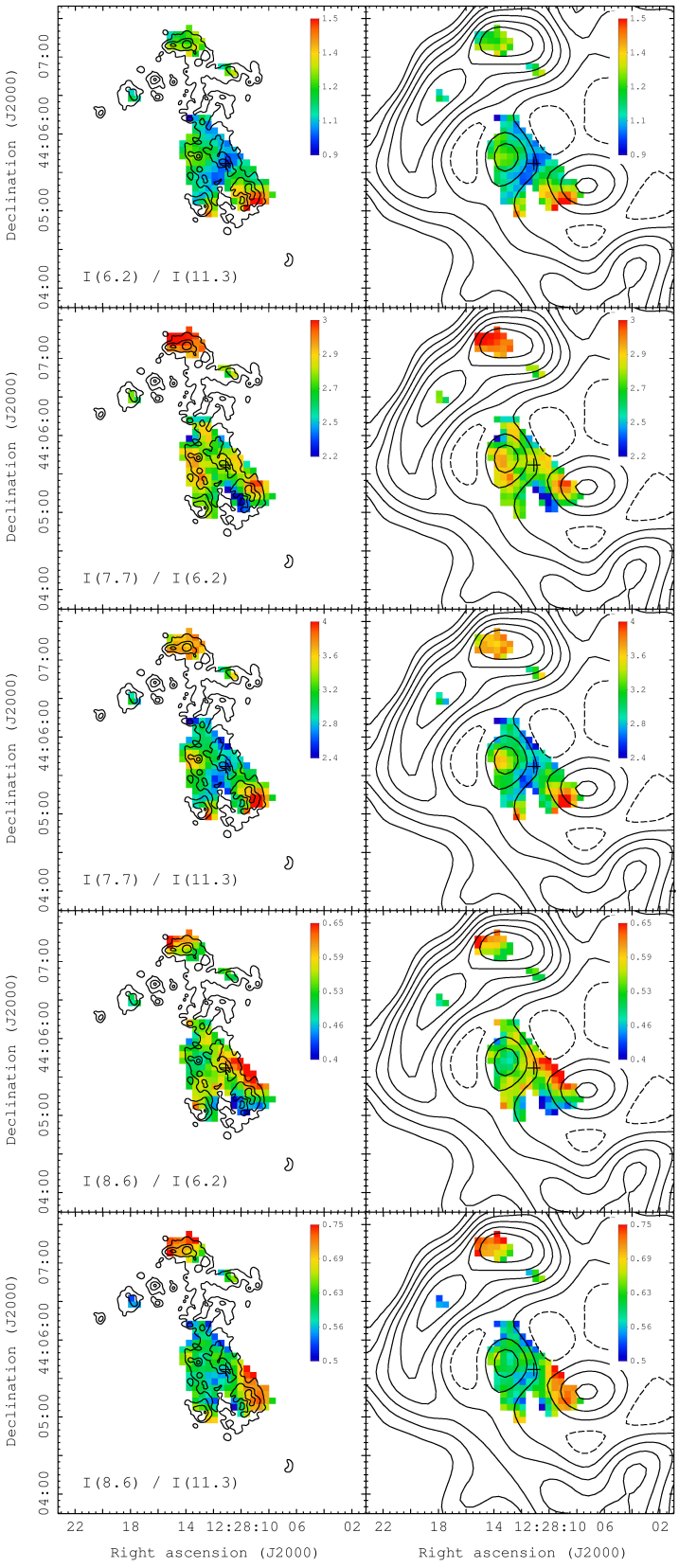

Figure 3.10. Maps of ratios of PAH band fluxes obtained by spectral decomposition. In column 1 the contours enclose the brightest 70, 40 and 16 per cent of the total Hα emission. In column 2 the contours show the emission of H I 21 cm, where the dashed H I contours indicate minima. The cross denotes the optical centre of the galaxy. *(continued on next page)*

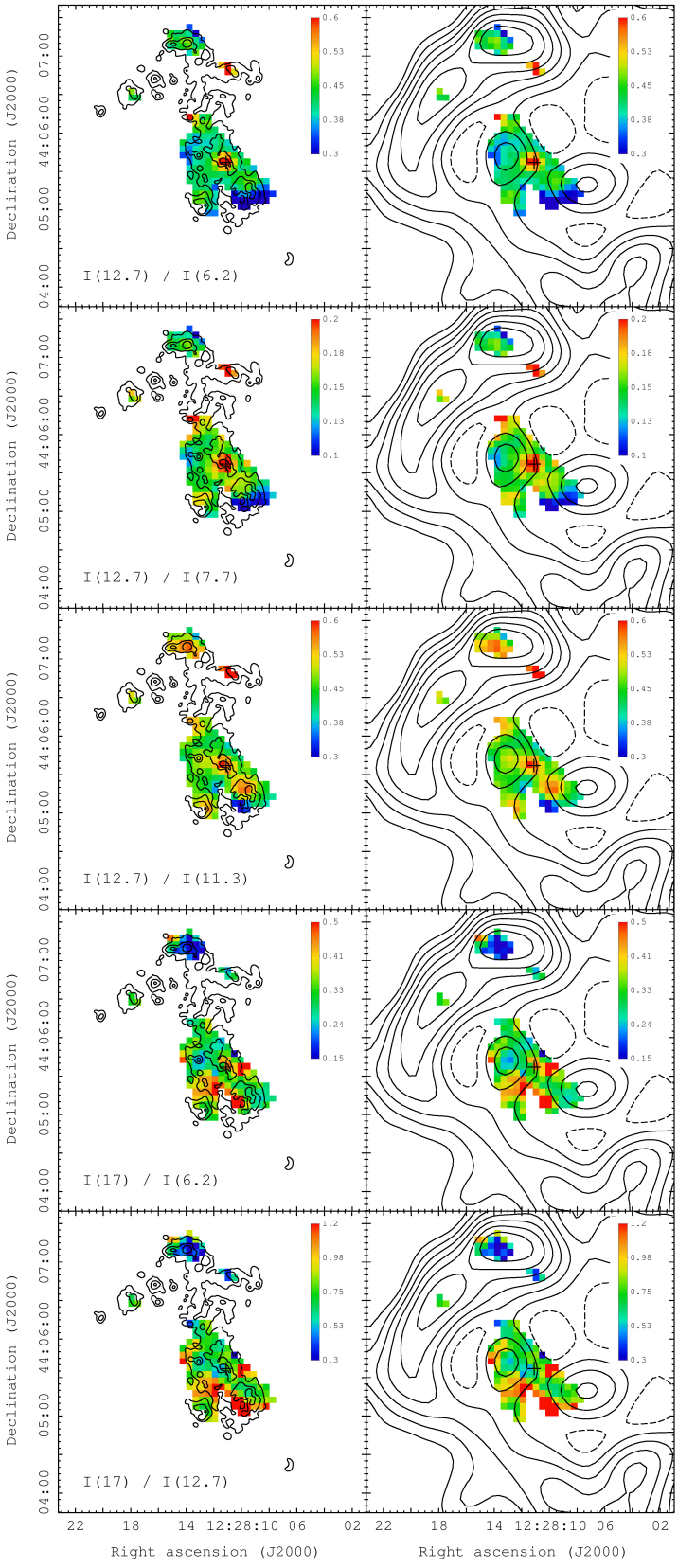

Figure 3.10. *(continued from previous page)*

The selection of spectra in Fig. 3.4 shows small differences in strength and smoothness of the 17 μm PAH complex. The PAH features comprising this complex are attributed to a small number of large (50–200 carbon atom) PAH molecules, which are neutral ('15–18 μm plateau') or ionized (bands centred at 16.4, 17.4 and 17.8 μm; Boersma et al. 2010; Peeters et al. 2012), with a possible contribution from fullerenes (C_{60}) at 17.4 μm (Sellgren et al. 2010). Therefore, the ratios involving the 17 μm complex are likely to trace the largest PAH molecules.

The shape of the complex may also be affected by nearby silicate absorption or emission at 18 μm. Spoon et al. (2007) present a galaxy classification based upon the strength of the 9.7 μm absorption feature, which suggests that smoothness of the 15–20 μm region may be a function of silicate content and relative PAH strength. In starburst galaxies the silicate features may be concealed by prominent PAH emission and warm dust continuum. Since in NGC 4449 the PAH emission dominates the 15–20 μm region (Fig. 3.3) we conclude that the contribution from hot silicates is small.

Overall, we note that the coverage of our data (Fig. 3.4) is too limited to show statistically significant spatial correlations. While the peaks of the integrated PAH emission and of some PAH band ratios coincide with the H I emission or the Hα emission, we note that the H I emission, the Hα emission and the PAH emission are not expected to originate from the same physical environments, and it is likely that mixing of ISM phases occurs at the limited resolution of our maps.

Correlations

In Fig. 3.11 we present pixel-by-pixel correlation plots of selected PAH band ratios. The $I_{7.7}/I_{11.3}$ is expected to vary with ionization, extinction and the PAH temperature distribution affected by the ISRF or the PAH grain size distribution (Galliano et al. 2008b). However, if temperature effects are considered, an increase of $I_{7.7}/I_{11.3}$ implies a decrease of $I_{7.7}/I_{6.2}$. Since in Fig. 3.11 this is not observed and the extinction differences can be neglected, we conclude, in agreement with Galliano et al. (2008b), that this ratio traces PAH ionization.

Our results for $I_{8.6}/I_{6.2}$ vs. $I_{7.7}/I_{11.3}$ show that $I_{8.6}/I_{6.2}$ does not vary with ionization. The relative importance of the 6.2, 7.7 and 8.6 μm bands relative to the 11.3 μm bands is illustrated on the right in Fig. 3.11. These plots show that $I_{7.7}$ is the dominant tracer of ionized PAH emission, with best-fitting linear slope coefficients of 2.7 and 5.1, similar to those for the galaxies M82 and M51, respectively (Galliano et al. 2008b). The plots in Fig. 3.11 show close similarities to the results of Galliano et al. (2008b) and support their conclusion that the mixture of PAH molecules, as traced by PAH ionization, is universal across different environments and distance scales.

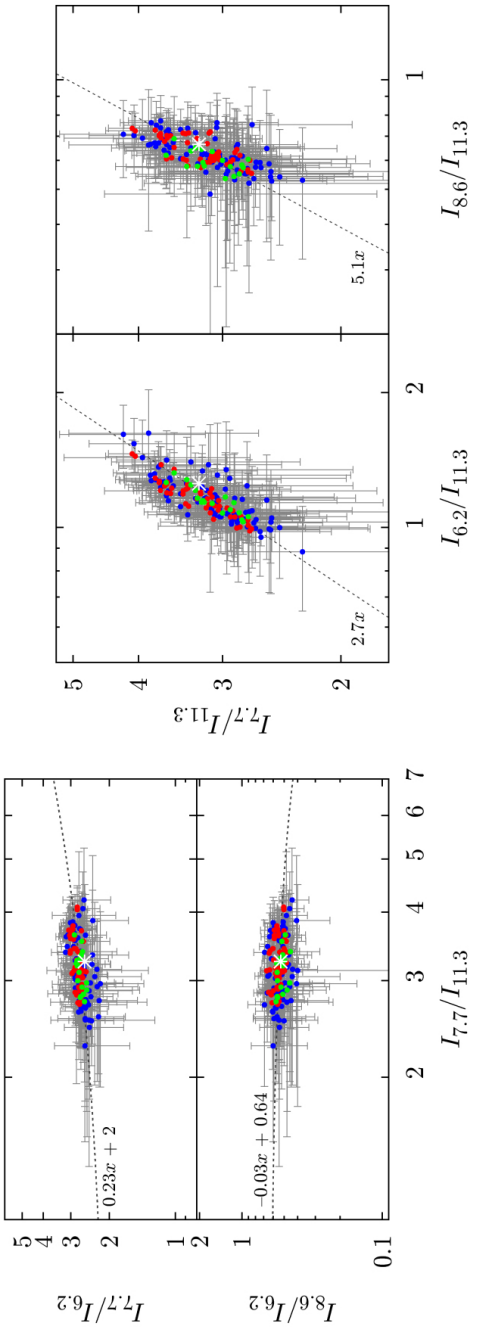

Figure 3.11. PAH band intensity ratios within NGC 4449. The dashed lines indicate the lines of best fit. The symbols are colour-coded according to the regions indicated in Fig. 3.4 and the white asterisk denotes the global value.

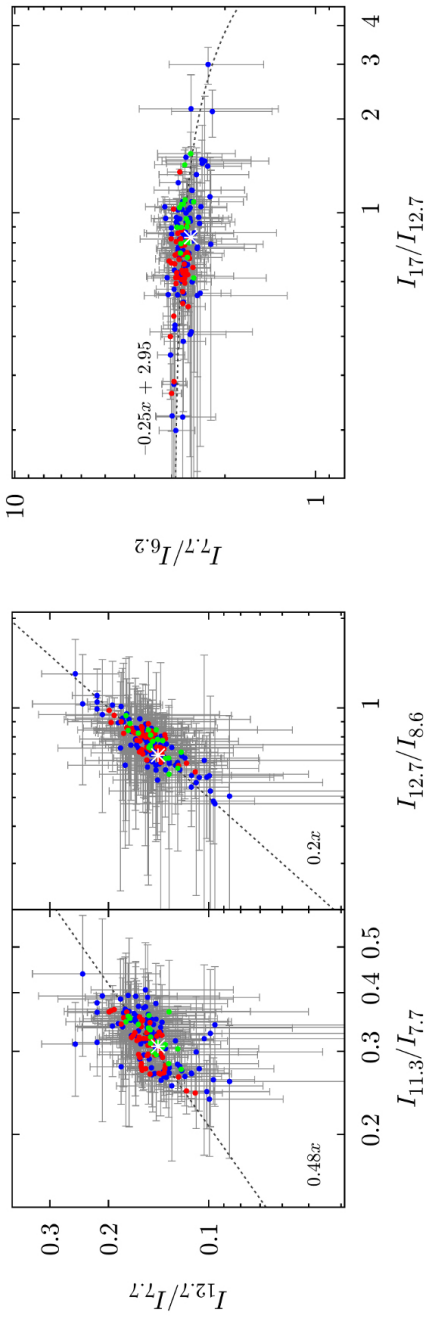

Figure 3.12. 12.7 and 17 μm PAH band intensity ratios within NGC 4449. The dashed lines indicate the lines of best fit. The symbols are colour-coded according to the regions indicated in Fig. 3.4 and the white asterisk denotes the global value.

In Fig. 3.12 we present plots of longer wavelength band ratios. The plot of $I_{12.7}/I_{7.7}$ vs. $I_{11.3}/I_{7.7}$ shows a weak correlation, suggesting that $I_{12.7}/I_{7.7}$ only weakly depends on ionization. The ratios $I_{12.7}/I_{7.7}$ and $I_{12.7}/I_{8.6}$ are strongly correlated, while $I_{7.7}/I_{6.2}$ shows no variation with $I_{17}/I_{12.7}$. These results reaffirm the common origin of the bands centred at 6.2, 7.7 and 8.6 μm. Additionally, $I_{17}/I_{12.7}$ shows a large dynamic range, which may reflect the presence of regions abundant in larger PAH molecules, as well as regions deficient in larger molecules. The maps of $I_{17}/I_{6.2}$ and $I_{17}/I_{12.7}$ in Fig. 3.10 show that the highest ratios are located away from the brightest H II regions. Therefore, it may be postulated that these sites in NGC 4449 have suitable conditions for the growth of large particles.

3.5.2 Fine-structure lines

Fig. 3.13 shows maps of fine-structure FIR emission in NGC 4449. The integrated line fluxes are given in Table 3.3.

Out of the five FIR lines observed in NGC 4449, [C II]$_{158}$ is the brightest globally, followed by [O III]$_{88}$ at half of the [C II]$_{158}$ luminosity and [O I]$_{63}$ at one third of the [C II]$_{158}$ luminosity. The coverage of [N II]$_{122}$ and [O I]$_{146}$ is limited to the centre of NGC 4449 and we note that their average S/N is low, as indicated in the caption of Fig. 3.13.

[C II]$_{158}$, [O III]$_{88}$ and [O I]$_{63}$ all peak in the centre, in the SW and in the N of NGC 4449. These regions are also the brightest Hα sites in NGC 4449. Compared with [C II]$_{158}$, the emission from [O III]$_{88}$ and [O I]$_{63}$ is more localised and peaks sharply near the centre and in the SW. [O III]$_{88}$ is equally bright in all three regions with local intensities reaching approximately 125 per cent of [C II]$_{158}$. Qualitatively, [O III]$_{88}$ and [O I]$_{63}$ arise primarily from more active regions associated with the Hα emission, while [C II]$_{158}$ is also detected in more quiescent regions. This is expected, as O III has a high ionization potential, while [O I]$_{63}$ has a high critical density (cf. Fig. 3.1). Therefore, [O I]$_{63}$ and [O III]$_{88}$ are expected to provide cooling in the high density or high ionization regimes, respectively. [C II]$_{158}$, on the other hand, is expected to provide cooling mainly in diffuse regions with intermediate conditions.

3.5.3 The origin of the [C II]$_{158}$ emission

The [C II]$_{158}$ emission may arise from neutral as well as ionized phases of the ISM (e.g. Heiles 1994, Kaufman et al. 2006). In extragalactic studies these phases are often mixed within a single telescope beam; for example the 11.″5 PSF of *Herschel*/PACS at 158 μm probes $\sim$200 pc at the distance of NGC 4449. Verifying the origin of the [C II]$_{158}$ emission can be aided by another tracer of ionized gas, such as [N II]$_{122}$. In our *Herschel*/PACS maps (Fig. 3.13), [N II]$_{122}$ is detected with 2σ significance only near the centre of NGC 4449, where the density of ionized gas is $\sim 200\,\mathrm{cm}^{-3}$ (Fig. 3.7).

If [C II]$_{158}$ comes from ionized regions, then for $n_\mathrm{e} \sim 200\,\mathrm{cm}^{-3}$ a ratio [C II]$_{158}$/[N II]$_{122}$ of 0.6–0.8 is expected (e.g. Oberst et al. 2006, Croxall et al. 2012). However, near the centre [C II]$_{158}$ is brighter than [N II]$_{122}$ by a factor of $\sim$ 50 (see Fig. 3.13). In Fig. 3.14 we present a map of the [C II]$_{158}$ emission with the CO(1–0) contours from Böttner et al. (2003), suggesting that the main molecular gas reservoirs coincide spatially with the peaks of [C II]$_{158}$. Together, these results suggest that in the centre of NGC 4449 the [C II]$_{158}$ emission arises primarily from the PDRs.

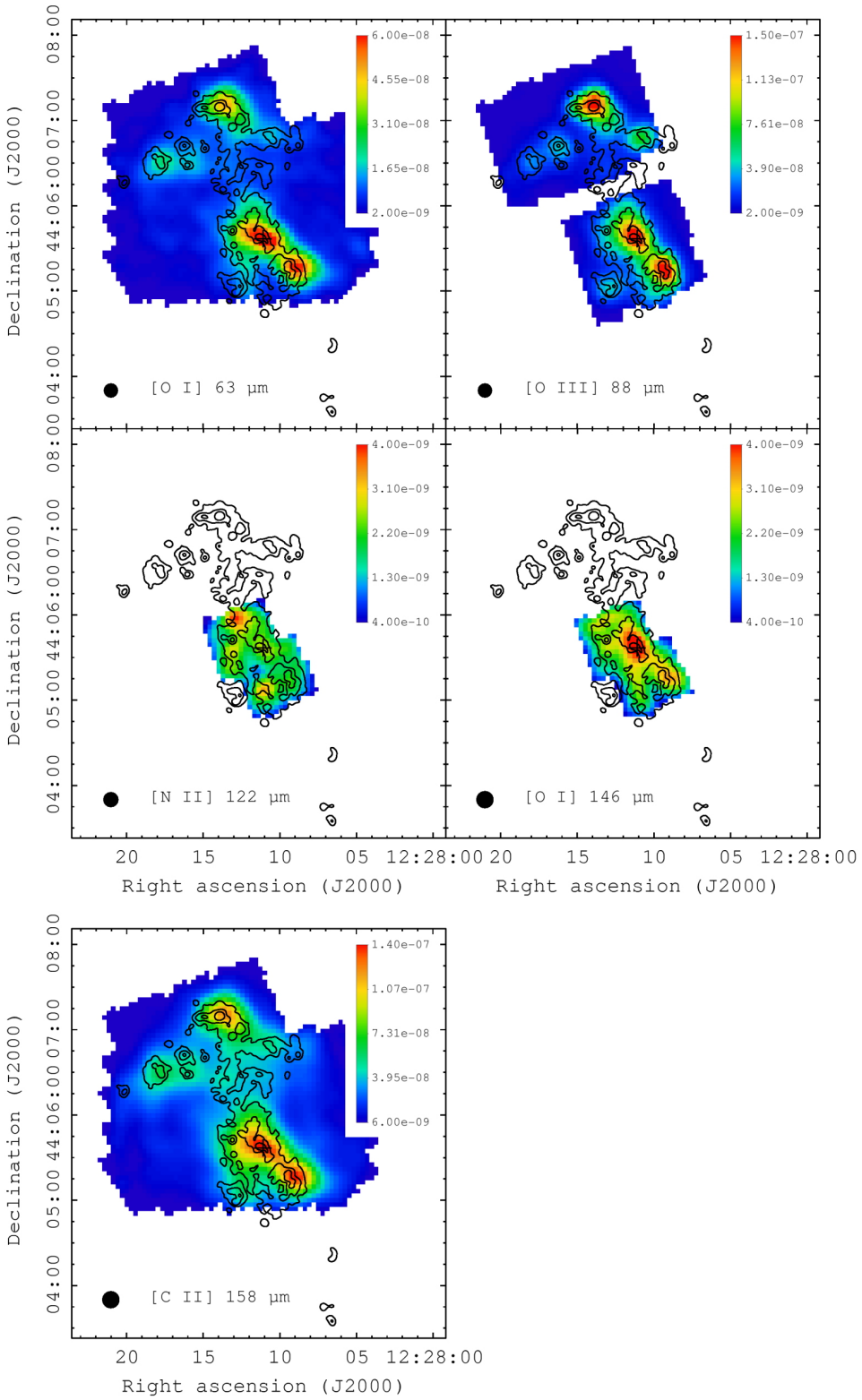

Figure 3.13. Maps of the fine-structure emission lines [O I]$_{63}$, [O III]$_{88}$, [N II]$_{122}$, [O I]$_{146}$ and [C II]$_{158}$ obtained from *Herschel*/PACS observations of NGC 4449. Fluxes are given in units of W m^{-2} sr^{-1} and the mean flux uncertainties are 40, 30, 160, 90 and 10 per cent, respectively. The FWHM of the telescope beam are indicated by filled circles. Contours enclose the brightest 70, 40 and 16 per cent of the total Hα emission, and the cross denotes the optical centre of the galaxy.

Line	Flux $[10^{-14} \times \mathrm{W\,m^{-2}}]$
[O I] 63 μm	0.62 ± 0.01
[O III] 88 μm	0.97 ± 0.02
[N II] 122 μm	0.019 ± 0.003
[O I] 146 μm	0.022 ± 0.001
[C II] 158 μm	1.96 ± 0.01

Table 3.3. Integrated fluxes of FIR lines in the *Herschel*/PACS observations of NGC 4449 shown in Fig. 3.13.

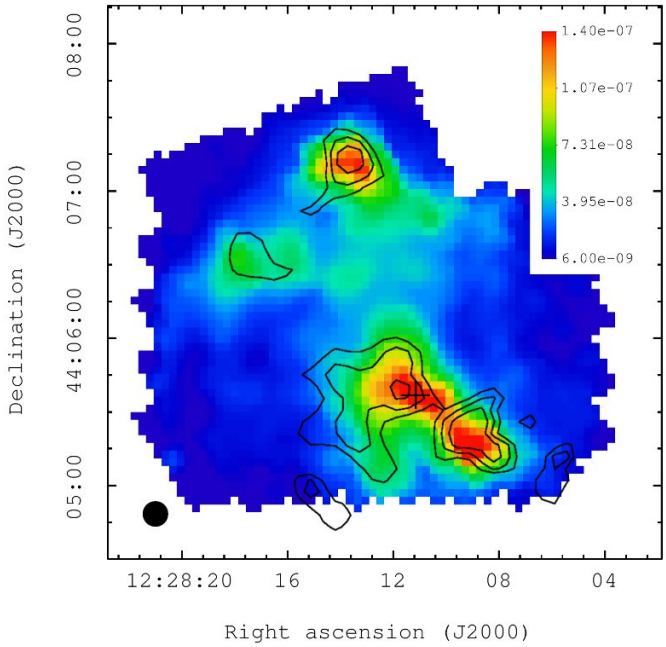

Figure 3.14. Map of the fine-structure emission line $[\mathrm{C\ II}]_{158}$ with CO(1–0) contours from Böttner et al. (2003). Fluxes are given in units of W m^{-2} sr^{-1} and the cross denotes the optical centre of the galaxy.

3.5.4 Heating and cooling in the ISM

In order to compare the relative importance of $[\mathrm{O\,I}]_{63}$, $[\mathrm{O\,III}]_{88}$ and $[\mathrm{C\,II}]_{158}$ as coolants within NGC 4449, we convolved the observations to a common resolution of 12″ and remapped onto a common grid using standard IDL routines and tools available as part of NASA's HEAsoft package (v6.7; released on 2009-08-19). The resulting maps were filtered leaving pixels with S/N of 1.75, 2 and 5 or better for $[\mathrm{O\,I}]_{63}$, $[\mathrm{O\,III}]_{88}$ and $[\mathrm{C\,II}]_{158}$, respectively.

The ISM heating processes can be traced by the PAH emission or the total FIR emission. Since the coverage of the map of total PAH emission in Fig. 3.9 is limited, we used an IDL script prepared by V. Lebouteiller to obtain a map of PAH emission from a background-subtracted 8 μm *Spitzer*/IRAC map corrected for stellar contamination, which was estimated by extrapolating background-subtracted *Spitzer*/IRAC maps at 3.5 μm and 4.6 μm (e.g. Helou et al. 2004, Marble et al. 2010). A fraction of the total PAH emission falling within the 8 μm *Spitzer*/IRAC band was estimated at 0.292 by analysing the global spectrum of NGC 4449 (Fig. 3.3) with MILES (Mid-Infrared Line Extraction Software) written by F. Galliano. Therefore, a high-resolution map of PAH emission was constructed by subtracting extrapolated stellar emission from the 8 μm map, and applying a correction of a factor of 3.42 to account for all PAH emission. The resolution of this map was degraded to a PSF of 12″ to allow direct comparison with the $[\mathrm{O\,I}]_{63}$, $[\mathrm{O\,III}]_{88}$ and $[\mathrm{C\,II}]_{158}$ maps.

When convolved to the same resolution and pixel scale, the pattern of emission in the PAH map derived from *Spitzer*/IRAC was found to be identical to the pattern of the total PAH intensity obtained from spectral decomposition of *Spitzer*/IRS observations with PAHFIT (Fig. 3.9). However, we found that the fluxes in the map derived from *Spitzer*/IRAC were larger by a median factor of 2.55 than the corresponding fluxes derived from *Spitzer*/IRS. This arises from the different treatment of the continuum emission in the two methods. In Fig. 3.9 the total PAH intensity is computed from a sum of best-fitting Drude profiles representing individual PAH features, whereas the map derived from *Spitzer*/IRAC takes into account the shape of the underlying continuum. Since the *Spitzer*/IRAC map offers a higher resolution and a better spatial coverage, it is preferred in this analysis.

To study the details of ISM heating and cooling we selected five regions of interest, which are shown in Fig. 3.15. Plots of $[\mathrm{O\,I}]_{63}/I_{\mathrm{PAH}}$, $[\mathrm{O\,III}]_{88}/I_{\mathrm{PAH}}$ and $[\mathrm{C\,II}]_{158}/I_{\mathrm{PAH}}$ trace the relative importance of $[\mathrm{O\,I}]_{63}$, $[\mathrm{O\,III}]_{88}$ and $[\mathrm{C\,II}]_{158}$ in cooling of the ISM on the physical scale of ~ 220 pc and are shown in Fig. 3.16.

The plots in Fig. 3.16 show a significant scatter in the individual lines as well as their combinations relative to the PAH emission. The observed ranges of ratio values for $[\mathrm{O\,I}]_{63}/I_{\mathrm{PAH}}$, $[\mathrm{O\,III}]_{88}/I_{\mathrm{PAH}}$ and $[\mathrm{C\,II}]_{158}/I_{\mathrm{PAH}}$ are 0.4–1, 0.5–4 and 0.015–4 per cent, respectively. For $([\mathrm{O\,I}]_{63} + [\mathrm{O\,III}]_{88})/I_{\mathrm{PAH}}$, $([\mathrm{O\,I}]_{63} + [\mathrm{C\,II}]_{158})/I_{\mathrm{PAH}}$, $([\mathrm{O\,III}]_{88} + [\mathrm{C\,II}]_{158})/I_{\mathrm{PAH}}$ and $([\mathrm{O\,I}]_{63} + [\mathrm{O\,III}]_{88} + [\mathrm{C\,II}]_{158})/I_{\mathrm{PAH}}$ the ranges are 1–4, 2–5, 2–6 and 2.5–7.

None of the plots in Fig. 3.16 show a tight correlation and a flat line of best fit. The best linear fit was obtained for $[\mathrm{C\,II}]_{158}/I_{\mathrm{PAH}}$, with a correlation coefficient r of -0.69. On the other hand, $[\mathrm{O\,III}]_{88}/I_{\mathrm{PAH}}$ shows no correlation with the PAH emission ($r = -0.013$) but with a large scatter of values. Combined plots of relative strengths of any two lines or all three lines do not show an improved correlation with I_{PAH}. This suggests that none of $[\mathrm{O\,I}]_{63}$, $[\mathrm{O\,III}]_{88}$, $[\mathrm{C\,II}]_{158}$ or their combinations fully account for all cooling on a linear distance scale of ~ 220 pc.

In comparison, a recent study of LMC-N11B by Lebouteiller et al. (2012) showed a flat

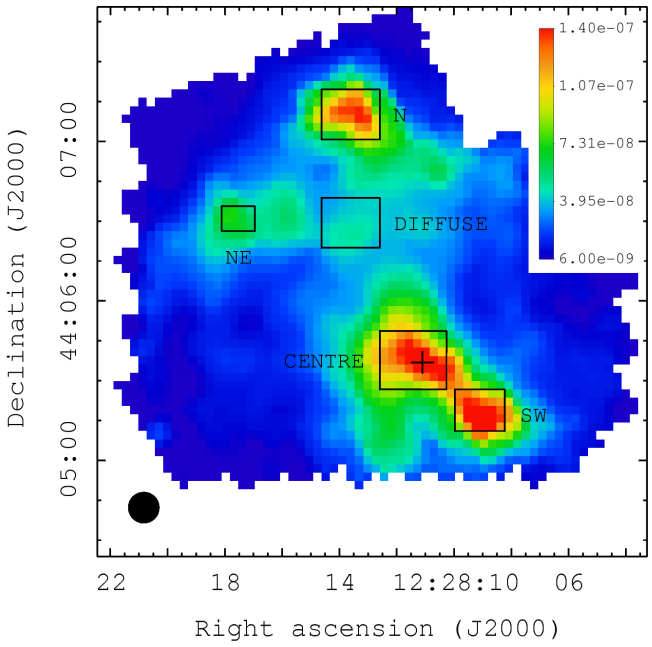

Figure 3.15. Regions of interest in NGC 4449 overlaid on top of a map of $[\mathrm{C\ II}]_{158}$. Fluxes are given in units of W m^{-2} sr^{-1} and the cross denotes the optical centre of the galaxy.

distribution of $([\mathrm{O\ I}]_{63} + [\mathrm{C\ II}]_{158})/I_{\mathrm{PAH}}$ across two decades in the PAH intensity. Since the observation FWHM of 12″ for N11B translates to 3 pc in linear distance, the individual high and low density PDRs, as traced by $[\mathrm{O\ I}]_{63}$ and $[\mathrm{C\ II}]_{158}$, can be fully resolved. Therefore, the flat distribution of $([\mathrm{O\ I}]_{63} + [\mathrm{C\ II}]_{158})/I_{\mathrm{PAH}}$ suggests that $[\mathrm{O\ I}]_{63}$ and $[\mathrm{C\ II}]_{158}$ dominate ISM cooling in N11B.

Fig. 3.16 shows that in NGC 4449 the different ISM phases are not resolved by our observations. However, dominant coolants may be determined locally for some of the regions shown in Fig. 3.15. These regions, except the diffuse region, also concide with peaks of Hα emission and with peaks of CO(1–0) tracing molecular gas (Figs. 3.13 and 3.14). While regions SW and NE offer too few pixels for a statistically significant analysis, we performed linear regression fits to pixels in the centre and in region N.

If cooling can be described fully by one or more species, then a regression fit is expected to be flat and tight (r and σ both close to 0). For the central region the lowest values of r and σ were obtained for $[\mathrm{O\ III}]_{88}/I_{\mathrm{PAH}}$ with $r = -0.09$ and $\sigma = 0.002$, whereas for region N $r = 0.09$ and $\sigma = 0.005$ were obtained for $([\mathrm{O\ III}]_{88} + [\mathrm{C\ II}]_{158})/I_{\mathrm{PAH}}$.

The distribution of emission in the diffuse region, on the other hand, shows a steep slope in all plots in Fig. 3.16, suggesting the presence of another important coolant, e.g. H_2 or diffuse CO, operating in this environment.

These results suggest that $[\mathrm{O\ III}]_{88}$ plays an important role in cooling in the central region of NGC 4449. In the N the cooling is best described by $[\mathrm{O\ III}]_{88} + [\mathrm{C\ II}]_{158}$, while in the diffuse region another coolant dominates the cooling processes on the physical scale probed by our observations.

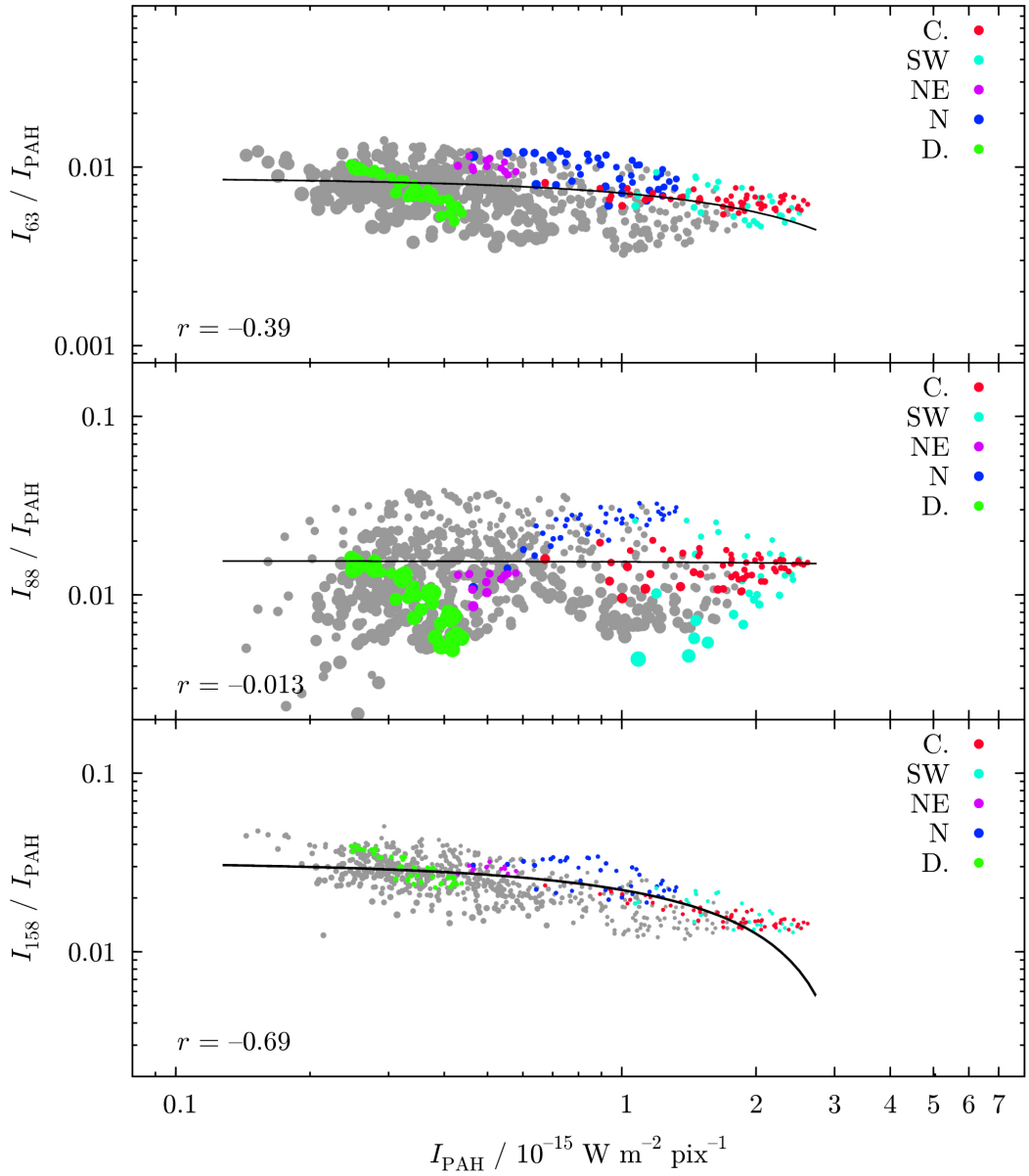

Figure 3.16. Plots of the cooling line intensities relative to the total PAH emission $I_{\rm PAH}$ within NGC 4449. The resolution of the data is 12″ (∼ 220 pc) and the pixel size is 3.″1. Symbol sizes are proportional to the overall uncertainty and the correlation coefficients for linear regression fits are indicated in bottom left corners of each plot. The central and the diffuse regions in Fig. 3.15 are abbreviated as 'C.' and 'D.'. *(continued on next page)*

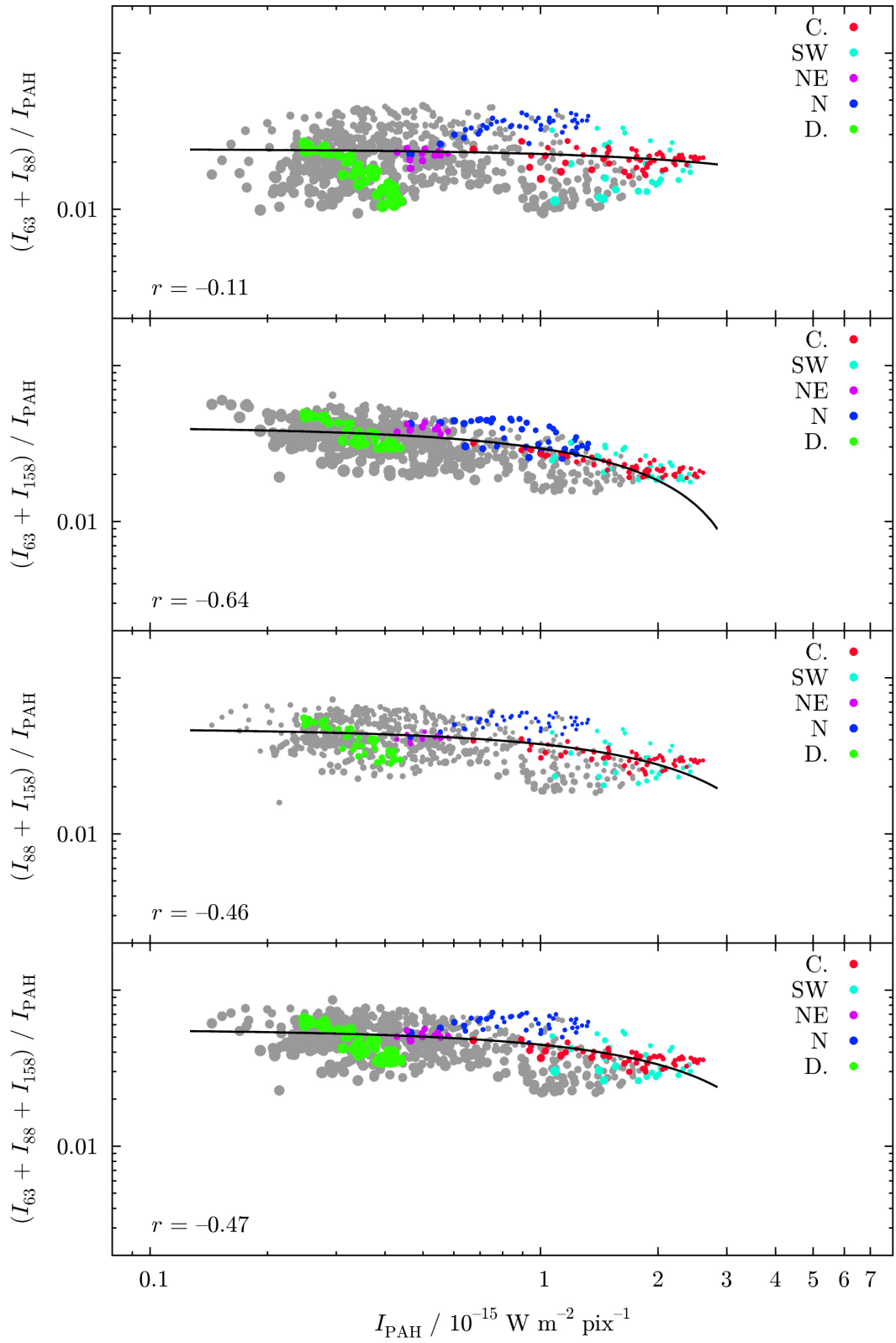

Figure 3.16. *(continued from previous page)*

3.5.5 Physical conditions

The physical conditions in PDRs can be described by the density of neutral gas n_0 and the strength of the ambient FUV radiation field G expressed in units of the Habing field G_0 (Habing 1968), where $G = 1.7G_0$ is the average Galactic FUV ISRF (Draine 1978). The observed fine-structure FIR line intensities can be compared with the PDR models of Kaufman et al. (1999, 2006) to infer n_0 and G locally. In particular, the ratio $[\mathrm{C\,II}]_{158}/[\mathrm{O\,I}]_{63}$ and the ratio of $[\mathrm{O\,I}]_{63} + [\mathrm{C\,II}]_{158}$ to the total FIR luminosity I_{FIR} can effectively constrain the n_0–G parameter space (e.g. Wolfire et al. 1990).

To use the $([\mathrm{O\,I}]_{63} + [\mathrm{C\,II}]_{158})/I_{\mathrm{FIR}}$ diagnostic, we constructed a map of I_{FIR} from *Herschel*/PACS and *Herschel*/SPIRE photometry described in Section 2.2.3. These data were supplemented by *Spitzer*/MIPS observations at 24 μm provided by Bendo et al. (2012b). The photometric and spectroscopic observations were degraded to a resolution of $40''$ and remapped onto common grid. At every pixel, the spectral energy distribution (SED) consisting of photometric measurements at 24, 70, 100, 160, 250, 350 and 500 μm was integrated between 24 and 500 μm to give the observed I_{FIR}. A map of I_{FIR} is presented in Fig. 3.17. The properties of dust emission are further discussed in Section 3.6. Additionally, the maps of $[\mathrm{O\,I}]_{63}$ and $[\mathrm{C\,II}]_{158}$ were filtered leaving pixels with S/N of 3 and 8 or better, respectively.

The map of the total PAH emission described in Section 3.5.4 was similarly degraded and remapped to allow direct comparison with I_{FIR}. In Fig. 3.18 we present a correlation plot showing that I_{FIR} and I_{PAH} are strongly correlated. The resolution of the data is equivalent to ~ 700 pc in linear distance, and therefore the ISM phases giving rise to the PAH emission and the phases giving rise to the emission from large grains are mixed within a single beam. A strong correlation is expected from similar ISRFs from the same star-forming processes interacting with the PAHs and larger grains on similar time-scales.

The available set of diagnostic lines and diagnostic ratios is presented in Fig. 3.19 and maps of the best-fitting neutral gas densities n_0 and FUV field strengths G, obtained from the PDR models of Kaufman et al. (1999, 2006), are shown in Fig. 3.20. The strongest FUV fields are predicted for the bright Hα regions near the centre and in the N of NGC 4449, with G reaching ~ 50 G_0 and ~ 40 G_0 there, respectively. Neutral gas densities in these two regions are predicted to be ~ 1000 cm^{-3}.

Quite noticeable in both maps is a stripe of lower G and higher n_0 intersecting a quieter Hα region in the East–West direction. In the bottom panel of Fig. 3.20 the contours of the atomic gas (H I) emission from the cold neutral phase in this region appear to follow the enhanced gas density in the warm neutral phase (n_0). The enhanced n_0 appears to drop in the NW, with the opposite behaviour being observed for G. On the whole, no spatial correlation between G or n_0 and H I is observed.

Fig. 3.20 can be compared with Fig. 3.21, which shows the spatial distribution of $([\mathrm{O\,I}]_{63} + [\mathrm{C\,II}]_{158})/I_{\mathrm{PAH}}$ and $([\mathrm{O\,I}]_{63} + [\mathrm{C\,II}]_{158})/I_{\mathrm{FIR}}$. The map of $([\mathrm{O\,I}]_{63} + [\mathrm{C\,II}]_{158})/I_{\mathrm{FIR}}$ shows the same dataset as the one presented in Fig. 3.19. The distribution of ratio values shown in Fig. 3.21 reaffirms the strong correlation between I_{PAH} and I_{FIR} visible in Fig. 3.18.

Although the distributions of $([\mathrm{O\,I}]_{63} + [\mathrm{C\,II}]_{158})/I_{\mathrm{PAH}}$ and $([\mathrm{O\,I}]_{63} + [\mathrm{C\,II}]_{158})/I_{\mathrm{FIR}}$ in Fig. 3.21, as well as Figs. 3.20 and 3.21 in their entirety were obtained independently, they show a remarkable similarity in their features. In particular, the regions of high $([\mathrm{O\,I}]_{63} + [\mathrm{C\,II}]_{158})/I_{\mathrm{PAH}}$ and high $([\mathrm{O\,I}]_{63} + [\mathrm{C\,II}]_{158})/I_{\mathrm{FIR}}$ form an extended arc around the centre of NGC 4449, which coincides with regions of enhanced n_0 and reduced G. This suggests that

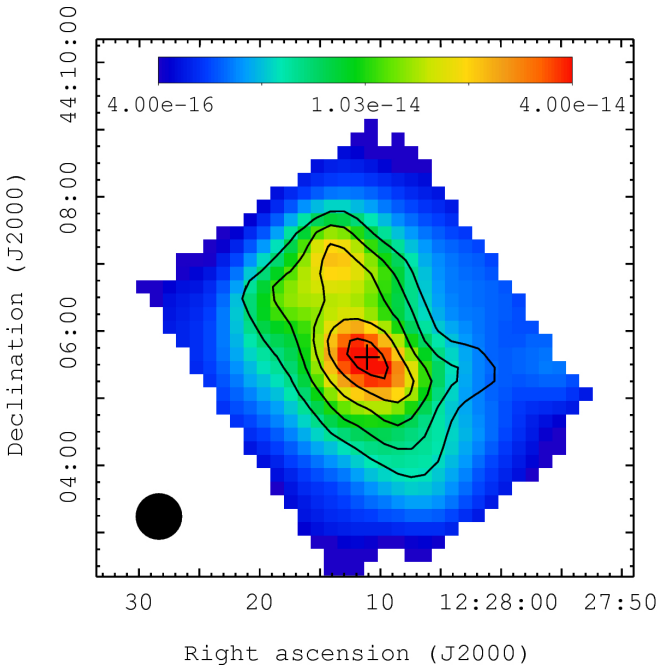

Figure 3.17. Map of the total FIR intensity in units of $\mathrm{W\,m^{-2}\,pix^{-1}}$, with the temperature of the coolest dust component as contours in steps of 24, 26, 28, 30 and 32 K, derived from modified blackbody fits to *Herschel*/PACS and *Herschel*/SPIRE photometry in the FIR (see Section 3.6). The cross denotes the optical centre of the galaxy.

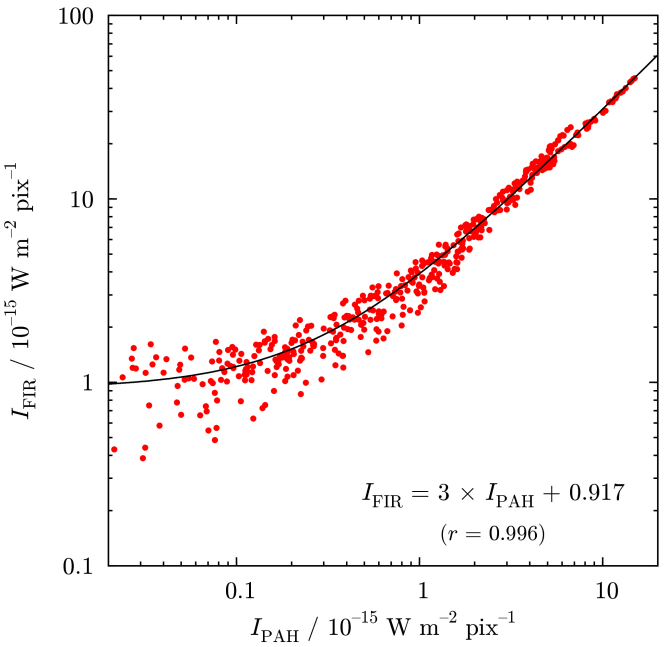

Figure 3.18. Correlation between the observed total FIR intensity I_{FIR} and the total PAH intensity I_{PAH} at a resolution of 40″. Each point represents one 10″ × 10″ pixel. I_{FIR} was obtained by integrating broadband observations from *Spitzer*/MIPS, *Herschel*/PACS and *Herschel*/SPIRE between 24 and 500 μm. I_{PAH} was obtained from *Spitzer*/IRAC observations corrected for stellar emission.

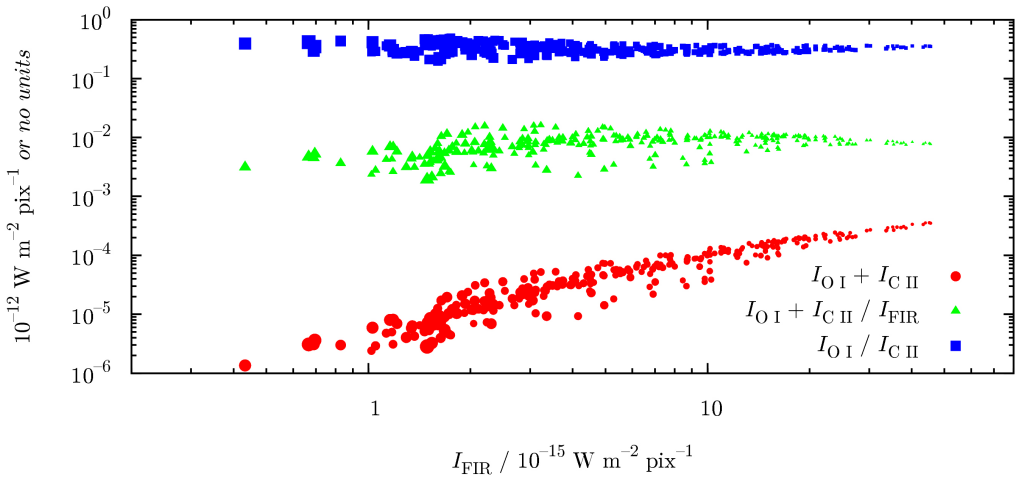

Figure 3.19. Plot of diagnostic line intensities and diagnostic line ratios within NGC 4449 at a resolution of 40″.

the PDRs there are characterised by higher gas density in the warm neutral ISM phase, a relatively soft ISRF and a high efficiency of ISM heating.

The heating efficiency from dust grains is expected to decrease for charged grains due to a higher Coulomb barrier (e.g. Bakes & Tielens 1994, Malhotra et al. 2001). This implies an increase of the heating efficiency for mostly neutral grains residing in regions with low G. Therefore, the significantly higher efficiencies in the arc visible in Figs. 3.20 and 3.21 are expected from the reduced strength of the ISRF, which itself results from reduced recent star formation activity (cf. Figs. 3.4 and 3.23). Higher photoelectric efficiences may also indicate larger optical depths and, consequently, the presence of intervening gas clouds (cf. Habart et al. 2001).

Both within and across galaxies H I is well correlated with recent star formation (e.g. Kennicutt 1989, Kennicutt et al. 2007). Therefore, the complicated morphology of H I emission, the lack of spatial correlation between H I and Hα near the centre of NGC 4449, and the lack of spatial correlation between H I and G or n_0, may result from the three-dimensional distribution of H I. We note that the region with enhanced n_0 coincides with a steep gradient of H I, while the Hα-bright regions in the N and NE coincide with peaks of H I. Therefore, it is possible that H I in the N and NE belongs to the same dynamical system as the Hα emission there, whereas the prominent H I features and the associated CO emission near the centre (cf. Fig. 3.14) partially result from cold atomic gas which is seen in projection. This hypothesis is strongly supported by the kinematic studies of Valdez-Gutiérrez et al. (2002), who found that the NE regions exhibit solid-body rotation, while the SE regions show abrupt velocity gradients. Additionally, the inner disc of H I is counter-rotating reflecting the likely interaction with the galaxy DDO 125 in the past (e.g. Hunter et al. 1999, Theis & Kohle 2001).

Overall, our results point to high densities of gas well shielded from hard ionizing radiation, which together create suitable conditions for the future formation of new stars.

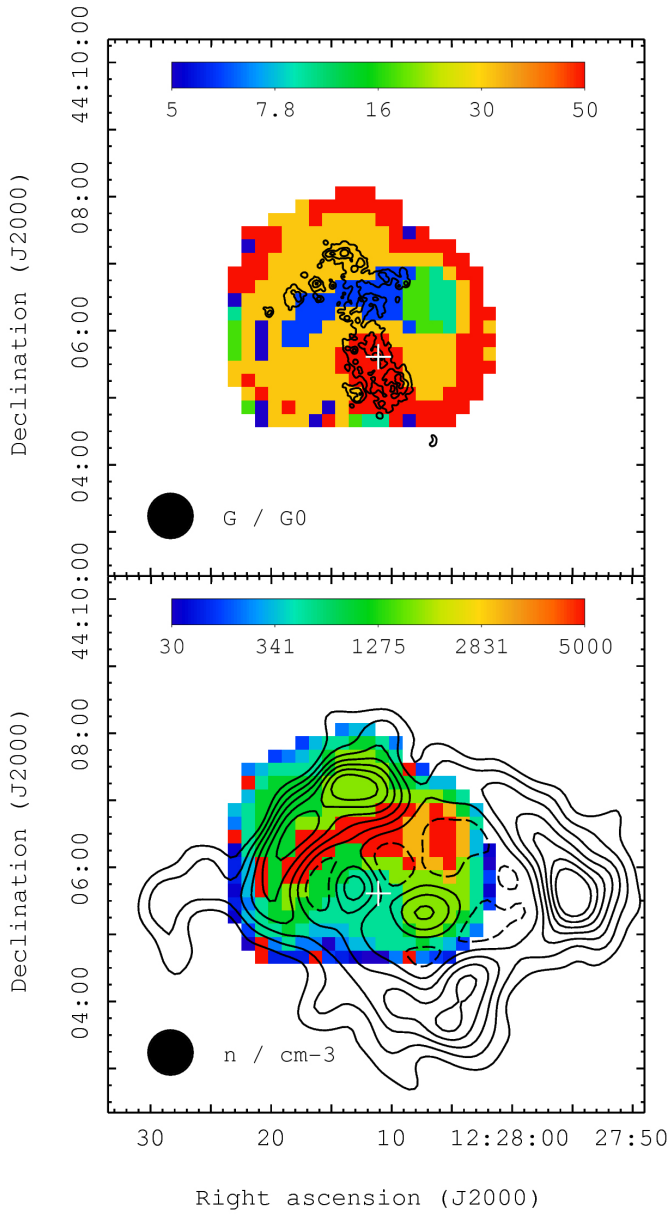

Figure 3.20. Maps of the best-fitting FUV field strengths G in units of G_0 (Habings; Habing 1968; top) and neutral gas densities n_0 in units of cm^{-3} (bottom) obtained from the PDR models of Kaufman et al. (1999, 2006) using the data in Fig. 3.19. The outer pixels are associated with significant uncertainties. Contours enclose the brightest 70, 40 and 16 per cent of the total Hα emission (top) or the emission of H I 21 cm, where the dashed H I contours indicate minima (bottom). The cross denotes the optical centre of the galaxy.

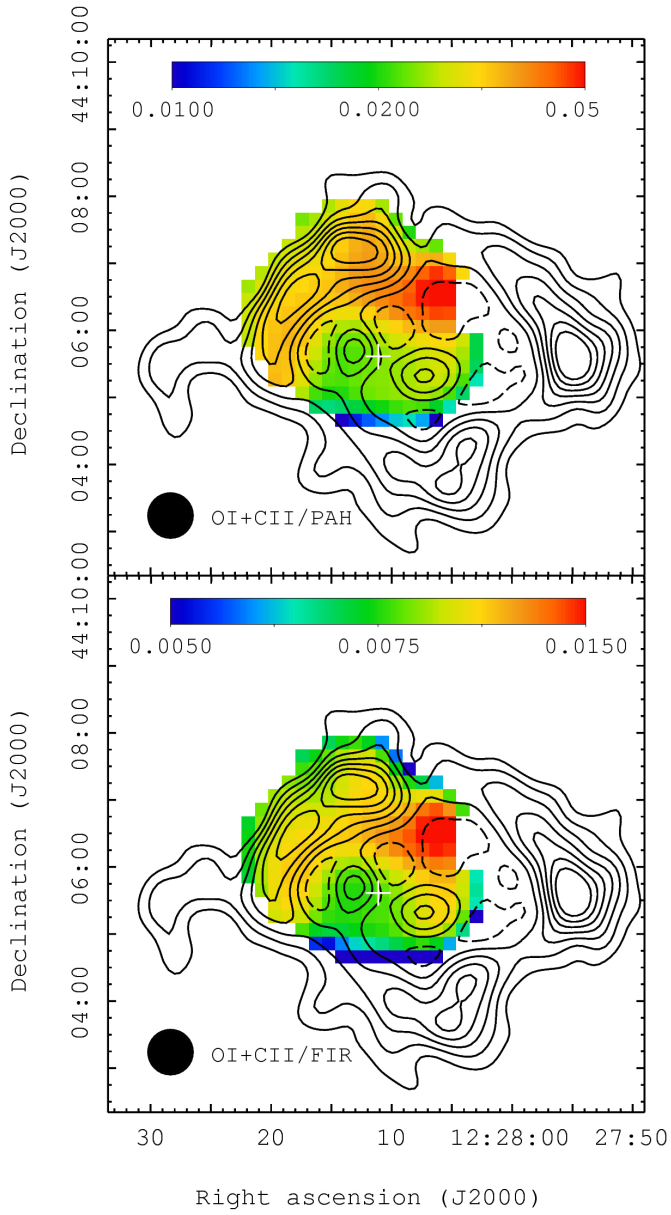

Figure 3.21. Maps of ($[\mathrm{O\,I}]_{63}$ + $[\mathrm{C\,II}]_{158}$)/I_{PAH} (top) and ($[\mathrm{O\,I}]_{63}$ + $[\mathrm{C\,II}]_{158}$)/I_{FIR} (bottom). I_{PAH} was obtained from *Spitzer*/IRAC observations corrected for stellar emission. I_{FIR} was obtained by integrating broadband observations from *Spitzer*/IRS, *Herschel*/PACS and *Herschel*/SPIRE between 24 and 500 μm. Contours enclose the emission of H I 21 cm, where the dashed H I contours indicate minima, and the cross denotes the optical centre of the galaxy.

3.6 Far-infrared dust emission

The multiwavelength *Spitzer* and *Herschel* observations used to construct a map of the total FIR intensity can be analysed further to reveal general properties of dust in the ISM of NGC 4449. The photometric FIR observations described in Section 3.5.5 were fitted with a modified blackbody function in the form $S_\lambda \propto \lambda^{-\beta} B_\lambda(T)$, where β is the dust emissivity index, $B_\lambda(T)$ is the Planck function and T represents the average dust temperature. We used the CMPFIT package (v.1.2; Markwardt 2009) to compute best-fitting modified blackbody (mbb) temperature $T_{\rm mbb}$ and β at every pixel. A single modified blackbody profile was found unsuitable for fitting 24 and 70 μm together with the remaining bands, and these bands were excluded from the final fits. This suggests a broad range of dust temperatures and a possible contribution from stochastically heated very small dust grains emitting at 24 and 70 μm (cf. Draine & Li 2001, Marengo et al. 2010). Additionally, the weighting of the 100 μm flux was dynamically adjusted based on the S/N of the data, to ensure that only the coolest dust component is fitted.

A map illustrating the results from the fits at 632 positions covering an area of $5'.6 \times 4'.6$ is presented in Fig. 3.17. The total $I_{\rm FIR}$ for NGC 4449 is estimated at $(340 \pm 20) \times 10^{-14}$ W m^{-2}. The distributions of $I_{\rm FIR}$ and of $T_{\rm mbb}$ closely resemble the optical morphology of NGC 4449. However, the best-fitting values of β do not vary linearly with $I_{\rm FIR}$ or $T_{\rm mbb}$. Fig. 3.22 shows the correlation plots of the three parameters. The emissivity index β varies between ~ 1.3 and ~ 2.5, and approaches $\beta = 1.5$ at higher $I_{\rm FIR}$, but generally shows no significant correlation with $I_{\rm FIR}$. However, β is more tightly related to $T_{\rm mbb}$ with a linear correlation coefficient of -0.82 and a slope of -0.058. An anti-correlation between β and the best-fitting dust temperature $T_{\rm dust}$ was observed previously in Galactic studies and may reflect the intrinsic physical and chemical properties of the dust grains present (e.g. Désert et al. 2008 and references therein).

The dust emissivity index β alone can be interpreted in terms of the size of emitting dust grains, where $\beta \sim 0$ corresponds to larger grains and $\beta \sim 2$ corresponds to smaller grains in the ISM (e.g. Miyake & Nakagawa 1993; also see Section 4.4). Globally, $\beta \approx 1.5$ is observed across a range of galaxies, with lower emissivities postulated for metal-poor objects with weak ISRF (e.g. Boselli et al. 2012 and references therein). Fig. 3.22 shows that $\beta \approx 1.5$ well characterises almost one decade of $I_{\rm FIR}$, with a larger scatter observed at lower $I_{\rm FIR}$. Some environments at low $I_{\rm FIR}$ and low $T_{\rm mbb}$ suggest $\beta \approx 0$–1, which may suggest suitable conditions for the growth of larger grains. Since Fig. 3.22 does not show a clear trend towards lower values of β, we suggest that a similar analysis be performed on high S/N observations of a closer object, such as the LMC, to draw more firm conclusions.

3.7 Star formation rates

The prominent neon lines [Ne II]$_{12.8}$ and [Ne III]$_{15.6}$ (Fig. 3.3) are important coolants in H II regions (e.g. Burbidge et al. 1963) and can be used to estimate the recent SFR. Ho & Keto (2007) demonstrated a tight correlation between [Ne II] + [Ne III] and Brα, and derived an empirical formula relating the SFR to the total luminosity of [Ne II] + [Ne III].

The spatially resolved spectral fits obtained in Section 3.5.1 can be used to map star formation rates in NGC 4449. Although the [Ne II]$_{12.8}$ line is blended with the 12.7 μm PAH complex in our low resolution spectra, the results for other nebular lines (Table 3.2) generally

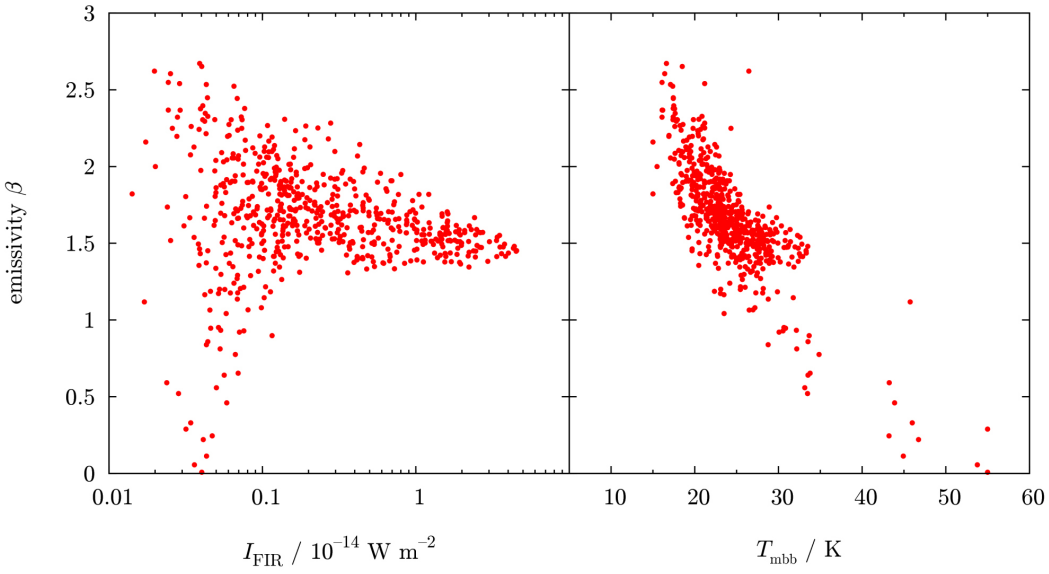

Figure 3.22. Plots of the emissivity β vs. the total FIR intensity $I_{\rm FIR}$ (left) and β vs. the temperature of the coolest dust component $T_{\rm mbb}$ (right) derived from modified blackbody fits to *Herschel*/PACS and *Herschel*/SPIRE photometry in the FIR.

show a good agreement between the fluxes derived from PAHFIT by spectral decomposition and those obtained from individual Gaussian fits. Therefore, we converted the [Ne II] + [Ne III] fluxes to SFRs assuming that individual [Ne II] line fluxes are correctly recovered by PAHFIT and adopting the ionization fractions $f_{(\rm Ne^+/Ne)} = 0.75$ and $f_{(\rm Ne^{2+}/Ne)} = 0.1$ (Ho & Keto 2007). The resulting map of SFR within NGC 4449 is presented in Fig. 3.23.

Using the formulation of Ho & Keto (2007) and the measurements in Table 3.2 the global SFR is estimated at 0.8–0.9 $\rm M_\odot\,yr^{-1}$. The integrated SFR within the blue regions in Fig. 3.4 is 0.42 ± 0.02 $\rm M_\odot\,yr^{-1}$ and the corresponding average projected SFR is 0.32 ± 0.01 $\rm M_\odot\,yr^{-1}\,kpc^{-2}$. The main sources of uncertainty in our derived SFRs are systematic: the uncertainties in recovering the [Ne II] line flux from a blend of features and the choice of the ionization fractions. Nevertheless, the global SFR derived from [Ne II] + [Ne III] is consistent with the range 0.3–1 $\rm M_\odot\,yr^{-1}$ obtained using other indicators (Hunter et al. 1986; Thronson et al. 1987; Hunter et al. 1999; corrected for $D = 3.8$ Mpc). Based on this range of global values we estimate the uncertainty in our star formation rates as 40 per cent.

Also indicated in Fig. 3.23 are contours of the ratio $[\rm S\,IV]_{10.5}/[\rm S\,III]_{18.7}$ constructed from the observations in Fig. 3.6. Since the ionization potentials to obtain $\rm S^{3+}$ and $\rm S^{2+}$ are 34.83 eV and 23.33 eV, respectively, their ratio traces the hardest radiation fields arising from the most active star-forming regions. While [S IV]/[S III] traces similar regions to [Ne III]/[Ne II], the former is derived from unblended lines directly from reduced data and thus preferred for this analysis. Unfortunately, the PSF of *Spitzer*/IRS and the S/N obtained at 18.7 μm mean that only in the central region of the galaxy can the ratio be reliably calculated.

Schaerer & Stasińska (1999) present models which can be used to convert the observed ratios to average ages of the underlying stellar populations. Based on their models, ratios greater than 0.7 for [S IV]/[S III] and greater than 1.4 for [Ne III]/[Ne II] consistently point to a population approximately 0–4 Myr old, with higher ratios suggesting a greater mass of the initial starburst. This result strongly indicates the presence of young massive stars in the

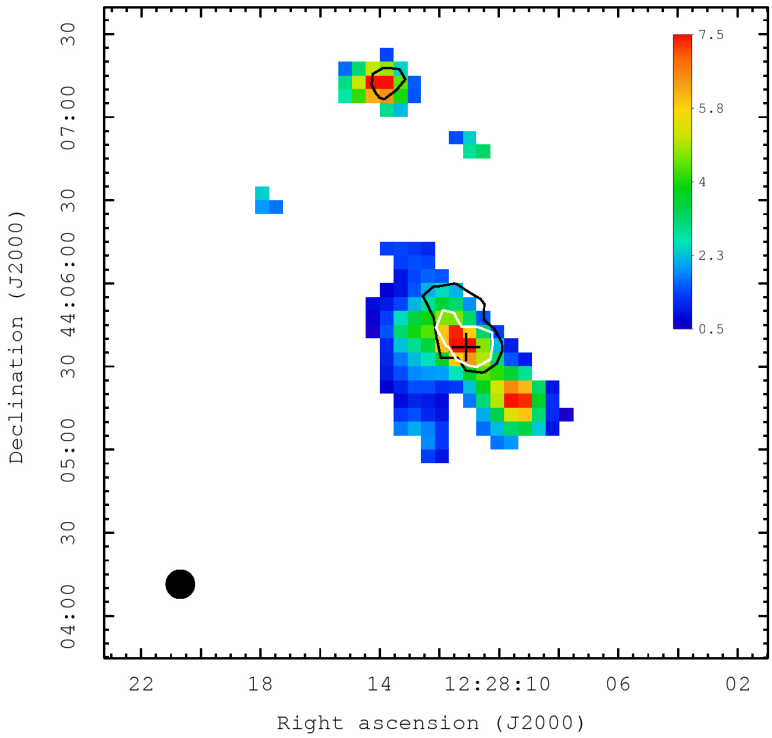

Figure 3.23. Map of the star formation rate in NGC 4449 in units of $10^{-3}\,M_{\odot}\,yr^{-1}\,pix^{-1}$ as traced by [Ne II]$_{12.8}$ + [Ne III]$_{15.6}$ according to the empirical relation of Ho & Keto (2007). The map was constructed using line intensities obtained from fitting the *Spitzer*/IRS observations (Fig. 3.4) with PAHFIT at every pixel. The uncertainty is estimated at 40 per cent. White area indicates regions with insufficient S/N for this analysis. Black contours enclose regions with [Ne III]/[Ne II] ≥ 1.4 and white contours enclose a region with [S IV]/[S III] ≥ 0.7 near the galaxy centre. The FWHM of 10″ is indicated by a filled circle and the cross denotes the optical centre of the galaxy.

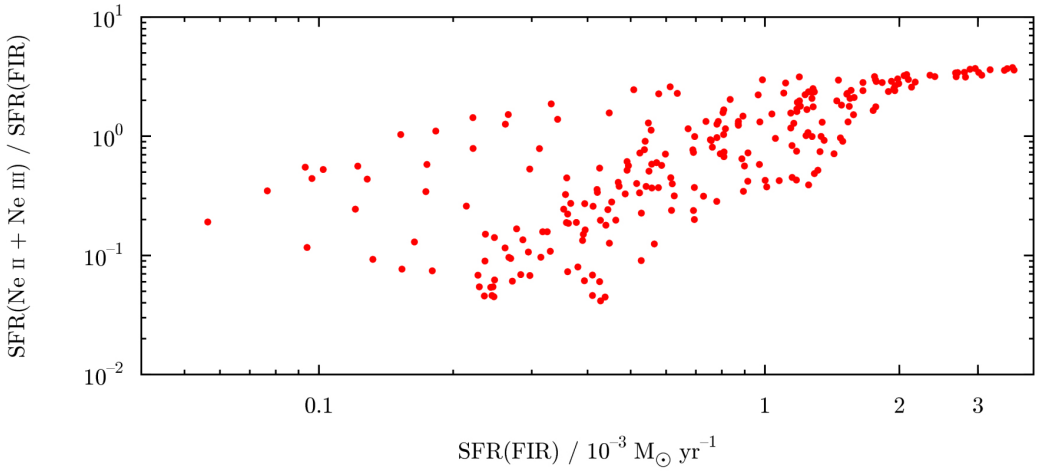

Figure 3.24. Comparison of SFR($[\mathrm{Ne\,II}]_{12.8}$ + $[\mathrm{Ne\,III}]_{15.6}$) with SFR($L_{\mathrm{FIR}}$). This plot was obtained from Figs 3.17 and 3.23 converted to a common resolution and pixel scale.

centre of NGC 4449, suggested previously by Martin & Kennicutt (1997) from the detection of broad Wolf-Rayet $\mathrm{He\,II}_{\lambda4686}$ and $\mathrm{C\,IV}_{\lambda\lambda5808}$ lines.

The map of the total luminosity in the FIR shown in Fig. 3.17 can also be used to estimate the SFRs. We used the calibrations of Kennicutt (1998) to convert L_{FIR} to SFRs. The resolution of the map in Fig. 3.23 was degraded to 40″ and remapped to allow a direct comparison with Fig. 3.17. The integrated SFR(L_{FIR}) for NGC 4449 is estimated at 0.27 ± 0.01 $\mathrm{M_\odot\,yr^{-1}}$. This is slightly lower than the estimate of 0.28 ± 0.01 $\mathrm{M_\odot\,yr^{-1}}$ based on the entire 8–1000 μm range and a single global SED, which includes additional global *Planck* measurements at 550 and 850 μm (see Section 2.4.2). Unfortunately, *Planck* observations offer insufficient resolution to be taken into account in our spatially resolved study, but considering our results from Section 2.4.2 the contribution of flux longwards of 500 μm to the global I_{FIR} and, consequently, to the global SFR(L_{FIR}) can be estimated at 6 per cent.

The plot in Fig. 3.24 shows that within NGC 4449 both SFR($[\mathrm{Ne\,II}]_{12.8}$ + $[\mathrm{Ne\,III}]_{15.6}$) and SFR($L_{\mathrm{FIR}}$) are well correlated, for SFR(L_{FIR}) $\gtrsim 2 \times 10^{-3}$ $\mathrm{M_\odot\,yr^{-1}}$. However, the correlation breaks down at lower SFRs, which is not unexpected. Both neon lines come from H II region species requiring relatively high ionization potentials and are produced through radiative de-excitation within H II regions. The total FIR luminosity, on the other hand, is produced by thermal emission from dust grains residing mostly outside the ionized regions. Therefore, the two tracers not only originate from different physical environments but may also trace the star formation processes on different time-scales. At higher SFRs, the two tracers are well correlated, but at lower SFRs the total FIR luminosity should be used together with an additional tracer to give more consistent estimates (e.g. Kennicutt et al. 2009).

3.8 Conclusions

In this work, we studied spatially resolved spectroscopic observations of NGC 4449. The available *Spitzer* data in the MIR covered the optical body of NGC 4449 and provided a spectral range of 5.2–38 μm (Figs. 3.2 and 3.4). In the FIR, the observations acquired by *Herschel* covered the majority of line emission from $[\mathrm{O\,I}]_{63}$, $[\mathrm{O\,III}]_{88}$ and $[\mathrm{C\,II}]_{158}$ and also covered the central region in $[\mathrm{N\,II}]_{122}$ and $[\mathrm{O\,I}]_{146}$ (Fig. 3.13).

We analysed the emission from H II regions (Section 3.4), as well as the PAH emission and the FIR line emission from the PDRs (Section 3.5). Additionally, we used photometric observations ranging from 24 μm to 500 μm to construct SEDs and to obtain a map of the total FIR intensity $I_{\rm FIR}$ at 632 positions within NGC 4449 (Section 3.6). Together, our results give valuable insight into the ionized and the warm neutral phases of the ISM in NGC 4449.

Nebular emission lines can effectively probe conditions in the H II regions. We showed that, averaged over $\sim$260 pc regions, the electron density near the centre of NGC 4449 reaches $\sim$300 cm^{-3}, with the densities falling to $\sim$20 cm^{-3} at the edges of its optical body. The high electron density regions are associated with a hard ISRF and very recent star formation activity reaching $\sim 7.5 \times 10^{-3}$ M$_\odot$ yr^{-1} locally. It is likely that the young stars inferred from our models in Section 2.4.2 reside mainly in these regions.

The PAH emission originates from small dust grains forming part of neutral ISM phases. The distribution of the total PAH emission follows the Hα contours at the resolution of our observations. Our results confirmed that the PAH bands centred at 6.2, 7.7 and 8.6 μm are tied together and, relative to the 11.3 μm complex, probe PAH ionization. We found a deficit of ionized PAHs near the centre of NGC 4449, which we interpret in terms of geometry, which is not resolved by our observations, or more efficient self-shielding resulting from a relatively higher metallicity and dust abundance.

We examined ratios of the individual cooling lines to the total PAH intensity to study ISM heating and cooling within NGC 4449. At a resolution of 220 pc none of the cooling lines described the ISM cooling consistently within the entire galaxy. However, we found that [O III]$_{88}$ peaks sharply and dominates the cooling in the most prominent Hα regions. Our results suggest that [O III]$_{88}$ + [C II]$_{158}$ describe well the ISM cooling to the N of the centre. In the noticeably more diffuse regions ISM cooling is likely to be dominated by another coolant. Overall, our results show that [O I]$_{63}$, [O III]$_{88}$ and [C II]$_{158}$ do not describe the ISM cooling globally, possibly due to mixing of different ISM phases within the telescope beam.

The FIR fine-structure gas emission and the FIR dust emission were compared with the models of Kaufman et al. (1999, 2006) and used to derive general properties of the PDRs. We found a stripe of enhanced neutral gas density ($\sim 5 \times 10^3$ cm^{-3}) and reduced strength of the ISRF ($\sim$ 5 G$_0$), which correlates spatially with an arc of enhanced heating efficiency around the centre of NGC 4449. Our results suggest a reservoir of gas in intervening clouds in this region, which may host future star formation activity.

Our modified blackbody fits to the FIR continuum suggest a spread in emissivities β between 1.5 and 2.5, with β approaching 1.5 for the brightest FIR regions. We note an anti-correlation between β and the temperature of the coolest dust component, which is likely to reflect intrinsic physical and chemical properties of dust.

We note two general limitations in our spatially resolved study of the ISM in NGC 4449. Firstly, the resolution of our data did not allow us to resolve individual H II regions or PDRs, and therefore our spatial analysis is contaminated by a mixture of ISM phases within a single telescope beam. Studies of closer objects, such as the LMC, are needed to supplement our FIR view of the ISM on smaller distance scales. Secondly, apparent spatial correlations with H I or CO may result from projection effects, and atomic or molecular gas traced by this emission does not necessarily form part of the environments around the PDRs probed by our observations. Similarly, other ISM coolants may operate in diffuse environments. The ionizing radiation traced by Hα is less prone to this effect due to the generally higher spatial resolution of observations at optical wavelengths.

4 Dust formation in the ejecta of Type Ibc supernovae

4.1 Introduction

Interstellar dust takes the form of small particles and is one of the major components of the ISM in galaxies. In Chapter 1 we discussed the likely sources of dust, namely the outflows from the asymptotic giant branch (AGB) stars and the ejecta from type II supernova explosions. Current estimates of dust formation rates in the outflows of AGB stars ($\sim 5 \times 10^{-5}\,\mathrm{M}_{\odot}\,\mathrm{yr}^{-1}$ of dust for the entire LMC, Matsuura et al. 2009) and in young type II supernova ejecta ($\sim 10^{-3}\,\mathrm{M}_{\odot}$ per type II supernova, Szalai & Vinkó 2013) are too low, however, to explain the inferred masses of dust in early Universe, or high-redshift, galaxies and dust growth in the ISM is often invoked (e.g. Draine 2009, Michałowski et al. 2010, Dwek et al. 2011b). In search of other possible sources of dust or dust formation mechanisms in the early Universe, observations of supernovae of types other than type II should be examined.

Supernovae are grouped into the hydrogen-deficient type I and the hydrogen-rich type II (e.g. Matheson et al. 2001). Neither type is homogeneous, but the type Ia and Ibc subclasses are of particular interest. Type Ia supernovae are explosions of mass-accreting white dwarfs exceeding the Chandrasekhar mass (e.g. Hillebrandt & Niemeyer 2000), whereas type Ibc and type II supernovae result from collapse of a Chandrasekhar-mass iron core inside a more massive progenitor (e.g. Woosley & Bloom 2006). Thus, type Ia and type Ibc explosions are similar in their deficiency of hydrogen but have fundamentally different origins (e.g. Porter & Filippenko 1987, Filippenko et al. 1990). The possible net contribution of dust formed in the different types of supernovae is a subject of debate. Ejecta of type II supernovae have been extensively studied and are believed to condense moderate amounts of dust (e.g. Sugerman et al. 2006, Meikle et al. 2007, Kotak et al. 2009, Meikle et al. 2011, Fabbri et al. 2011), with only recent *Herschel* observations and related models suggesting more substantial amounts (Matsuura et al. 2011, Wesson et al. in prep.). On the other hand, recent observations of the $\sim$400 year-old type Ia supernovae Tycho and Kepler show no evidence for net dust formation (Gomez et al. 2012a), which supports the expectation that in type Ia supernovae newly formed dust grains do not survive in the shocked gas (e.g. Nozawa et al. 2011 and references therein). The long evolution times of type Ia progenitors similarly make type Ia supernovae unlikely candidates for the main dust source in the early Universe (e.g. Yoshii et al. 1996).

Supernovae of type Ibc collectively refer to type Ib, type Ic and the mixed type Ib/c. These supernova types tend to be associated with H II and high surface brightness regions, and are believed to originate from Wolf-Rayet stars or massive interacting binaries (e.g. Georgy et al. 2009, Smartt 2009, Leloudas et al. 2010, Dessart et al. 2011). They are also sometimes linked to gamma ray bursts (GRBs; e.g. Woosley & Bloom 2006, Modjaz et al.

2008, Modjaz et al. 2011). Dust formation in such supernovae has been modelled in detail only for SN 2006jc (Mattila et al. 2008; Tominaga et al. 2008; Sakon et al. 2009), although general implications for dust formation were noted in numerous other studies (e.g. Hunter et al. 2009 and references therein). In the case of SN 2006jc, only 0.7–3 $\times 10^{-4}$ $M_\odot$ of dust has so far condensed in the ejecta, while a further 3–8 $\times 10^{-3}$ $M_\odot$ could have originated from mass loss from the progenitor.

Overall, the dust masses inferred from the FIR emission of supernova ejecta depend on the assumed dust composition, the amount of pre-existing dust, and the degree of clumpiness of the ejecta (e.g. Ercolano et al. 2007, Mattila et al. 2008, Fabbri et al. 2011, Matsuura et al. 2011, Wesson et al. in prep.). Also, only trace amounts of dust are expected to survive the reverse shock in higher-density environments (Bianchi & Schneider 2007). These factors give rise to large uncertainties in estimates of the net dust formation by supernovae.

In this work, we estimate the dust mass formed in the less well-studied type Ibc supernovae. We present estimates based on archival photometric data acquired by the *Spitzer Space Telescope* (Werner et al. 2004).

4.2 Observations

Spitzer is well equipped to study supernovae. Its InfraRed Array Camera (IRAC) covers the wavelength range of 3.2 to 9.2 μm in four channels centred at 3.6, 4.5, 5.8 and 8 μm (Fazio et al. 2004). Since idealised black body emission of hot dust of temperature $\sim$ 300–800 K peaks in this wavelength range, *Spitzer*/IRAC observations are of particular interest for studies of newly condensed dust (e.g. Fox et al. 2009). The associated point spread functions (PSFs) of 1.″7–2.″0 (IRAC Instrument Handbook; Laine 2013) translate to $\sim$ 150 pc in projected distance for a nearby host galaxy at 15 Mpc, thus allowing a more detailed study of the explosion sites as well as the surrounding environments.

This study was limited to type Ibc supernovae that were observed by *Spitzer* at epochs of presumed dust formation. Given that *(i)* in type II explosions, dust emission is detected broadly between day 300 and day 1000 after explosion (e.g. Wooden et al. 1993) and *(ii)* *Spitzer*/IRAC was in full operation between 2003 and 2009 (Mahoney et al. 2010), our selection criteria were:

1. supernova discovered between 2000 and 2009,
2. host galaxy within a distance of 35 Mpc (PSF $\lesssim$ 300 pc),
3. host galaxy observed by *Spitzer*/IRAC at least once between 2003 and 2009, and after explosion.

We used the Asiago Supernova Catalogue (Barbon et al. 1984, 1989, 1999) to select 17 type Ibc supernovae observed across 26 epochs by *Spitzer*/IRAC, as reported in the Spitzer Heritage Archive (SHA; Wu et al. 2010). For three supernovae, namely SN 2005V, SN 2006jc and SN 2007gr, comparison pre-explosion *Spitzer* observations exist.

Table 4.1 lists all SNe in our sample (column 1), their type (column 2), date of detection (column 3), coordinates (columns 4 and 5), host galaxy (column 6), distance to host galaxy (column 7), distance reference (column 8) and additional notes (column 9). A false-colour image of SN 2007gr, taken only 17 days after detection, is presented in Fig. 4.1.

SN	Type	Date	RA (J2000) [hh mm ss]	DEC (J2000) [dd mm ss]	Host	D [Mpc]	Reference*	Notes
2000 ds	Ib	2000-10-10	09 11 36.28	+60 01 43.3	NGC 2768	20.8	(1)	
2001 ci	Ic	2001-04-25	10 01 57.21	+55 41 14.0	NGC 3079	16.5	(2)	
2002 ap	Ic	2002-02-06	01 36 23.85	+15 45 13.2	M 74	9.3	(3)	broad-lined[a]
2002 ji	Ib/c	2002-11-30	11 22 53.15	+16 35 10.0	NGC 3655	26.42	(4)	
2003 H	Ib	2003-01-08	06 16 25.68	−21 22 23.8	NGC 2207	35	(5)	Ca-rich[b]
2003 id	Ic	2003-09-16	02 21 35.70	−05 31 51.0	NGC 895	35.3	(6)	
2003 jg	Ib/c	2003-10-24	09 45 37.91	−31 11 21.0	NGC 2997	12.2	(7)	
2004 C	Ic	2004-01-12	11 27 29.72	+56 52 48.2	NGC 3683	35	(2)	
2004 bm	Ic	2004-04-25	10 52 35.33	+22 56 05.5	NGC 3437	26.1	(2)	
2004 cc	Ic	2004-06-10	12 36 34.40	+11 14 32.8	NGC 4568	16.1	(8)	
2005 E	Ib	2005-01-13	02 39 14.34	+01 05 55.0	NGC 1032	34	(9)	Ca-rich[c]
2005 V	Ib/c	2005-01-30	06 18 38.28	+78 21 28.8	NGC 2146	14.5	(10)	
2005 at	Ic	2005-03-05	19 09 53.57	−63 49 22.8	NGC 6744	7.08	(2)	
2005 cz	Ib	2005-07-17	12 37 27.85	+74 11 24.5	NGC 4589	20.4	(11)	
2005 kl	Ic	2005-11-25	12 24 35.68	+39 23 03.5	NGC 4369	21.6	(12)	
2006 jc	Ib/c	2006-10-09	09 17 20.78	+41 54 32.7	UGC 4904	25.8	(13)	type Ibn[d]
2007 gr	Ic	2007-08-28	02 43 27.98	+37 20 44.7	NGC 1058	9.29	(14)	

* distance references: (1) Proctor et al. (2009); (2) Tully et al. (2008); (3) Hendry et al. (2005); (4) Sanders et al. (2003); (5) Elmegreen et al. (2001); (6) Hogg et al. (2007); (7) Hess et al. (2009); (8) Komugi et al. (2008); (9) Perets et al. (2010); (10) Greve et al. (2006); (11) Jensen et al. (2003); (12) Méndez-Abreu et al. (2008); (13) Pastorello et al. (2007); (14) Hunter et al. (2009).

[a] Maurer & Mazzali (2010); [b] Perets et al. (2010); [c] Anderson & James (2009); [d] Chugai (2009)

Table 4.1. Sample of 17 nearby supernovae observed by *Spitzer*/IRAC.

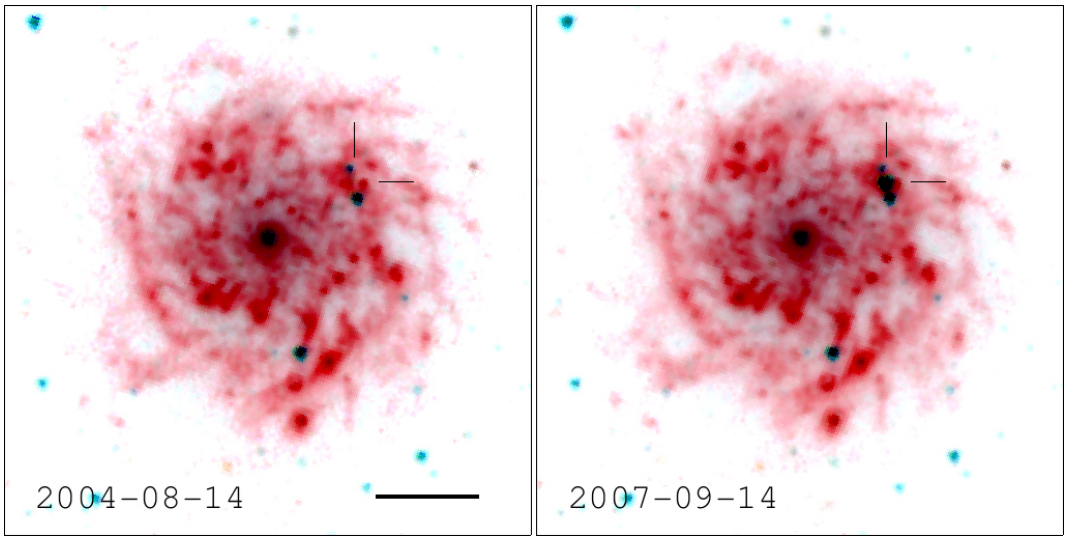

Figure 4.1. False-colour *Spitzer*/IRAC images of NGC 1058 before (left) and after the discovery of SN 2007gr on 28 Aug 2007 (right). The *Spitzer*/IRAC channels at 8 μm, 4.5 μm and 3.6 μm are shown in red, green and blue. North is up, east is to the left. The images are centred at $02^{\rm h}43^{\rm m}30\overset{\rm s}{.}0$, $+37^\circ20'29''$ (J2000), and the horizontal bar is $0\overset{'}{.}5$ in length (1.35 kpc).

We used Level 2 data products, also known as post-Basic Calibrated Data (PBCD) products, processed by the *Spitzer* pipeline and provided by the SHA. The pipeline software version was S18.7.0, except for Astronomical Observation Request (AOR) 14458624 (S18.5.0) and AOR 25631744 (S18.18.0). In the case of SN 2002ap we used the available reduced observations (S14.0.0) from the *Spitzer* Infrared Nearby Galaxies Survey (SINGS; Kennicutt et al. 2003).

Classification

The Asiago Supernova Catalog contains 234 entries for supernovae of type Ib or type Ic detected between 2000 and 2009. In this period and excluding the intermediate subclass Ib/c, type Ic supernovae were more abundant than type Ib by a factor of 1.9. Overall, the 280 type Ibc entries amounted to 9 per cent of the total, while the type Ia and type II entries corresponded to 61 and 30 per cent of the total, respectively. In a volume-limited sample the distribution is 21, 29 and 50 per cent, respectively, over a similar period (Smartt et al. 2009).

In many instances the exact supernova classification as a type Ib or a type Ic is uncertain, which may lead to a classification as the intermediate type Ib/c. Moreover, the initial classification may change once more detailed observations become available (see, e.g. Leloudas et al. 2011). We note that our conclusions in this study are based on the initial classifications, which were verified from the literature where possible; suitable annotations have also been included in Table 4.1.

4.3 Measurements

The images of supernovae listed in Table 4.1 are presented in Appendix B and were visually inspected for a detection. Where aperture photometry was feasible, smaller apertures were preferred in busy environments. We performed manual measurements for observations show-

ing no detections, or for detections where standard aperture photometry could not be used. In three supernovae, where pre-explosion galaxy images were available, aperture photometry was also performed on galaxy-subtracted images. In instances of non-detection, we used measurements on a nearby faint source to estimate the 3σ upper limits. We also attempted to measure absolute background levels for all non-detections. Finally, for all measurements we applied suitable aperture correction factors, as given in the IRAC Instrument Handbook. We used Starlink GAIA (v4.4.0) for all measurements.

In particularly busy environments we estimated the upper limit from noise statistics following the formalism of Fabbri (2011). The upper limit can be estimated by considering the probability that legitimate signal is concealed within a noisy background, and therefore the 3σ upper limit can be expressed as $3\sigma_{\rm a}\sqrt{N_{\rm a}}$, where $\sigma_{\rm a}$ is the standard deviation of flux density per pixel and $N_{\rm a}$ is the number of pixels within the measurement aperture.

Uncertainties in most measurements were dominated by the uncertainty in background subtraction due to high and varying backgrounds. We included the photometric calibration uncertainty at 4 per cent, which is twice the estimated uncertainty for carefully reduced data (Reach et al. 2005).

All flux measurements for the sample are given in Table 4.2 and comments on individual measurements can be found in Appendix B.

General properties of the sample

Based on Table 4.2 and the additional information presented in Appendix B, we report three detections and 14 non-detections at 8 μm. Out of the 14 non-detections, six explosions took place in low-IR background environments and six explosions took place in high-IR background environments. One non-detection, namely SN 2003id, shows distinct emission, which is however less than 3σ. In the case of SN 2004bm, another coinciding dust source is likely to be responsible for the observed emission. This classification is presented in Table 4.3, where the most relevant properties and measurements are also quoted.

Table 4.3 shows that two out of three of our detections at 8 μm are of type Ic. All three detections took place in busy or crowded environments, between $0.2R_{25}$ and $0.4R_{25}$ from the host galaxy centre in projected distance, where R_{25} is defined as a radius at which the B-band surface brightness of the host galaxy falls below 25 mag arcsec^{-2}. All the detections were found between day 17 and day 569 since discovery.

Six supernovae, which were non-detections, took place in a low absolute background environment, between $0.1R_{25}$ and $1.4R_{25}$ from the host galaxy centre in projected distance. The observations were made between day 222 and day 2237. Four out of six of these supernovae were of type Ib.

The other six supernovae, which were non-detections, took place in a high absolute background environment, between $0.03R_{25}$ and $0.20R_{25}$ from the host galaxy centre in projected distance. The observations were made between day 365 and day 1075. Four out of six of these supernovae were of type Ic. We note that where background measurements were possible, the absolute background levels near the explosion sites were remarkably similar.

SN	Epoch*	AOR†	$t_{\rm exp}$ / s	F_ν / μJy				$F_\nu(50\,{\rm kpc})^\ddagger$ / Jy
				3.6 μm	4.5 μm	5.8 μm	8 μm	8 μm
2000 ds	2237	18031872	46.8	≤ 12.7	≤ 20.8	≤ 14.1	≤ 21.2	≤ 3.7
2001 ci	1075	4331264	10.4	≤ 693	≤ 499	≤ 1320	≤ 3460	≤ 380
	2404	22000896	26.8	...	≤ 501	...	≤ 4340	≤ 470
	2799	25631744	1.2	≤ 476	≤ 205	≤ 5550	≤ 15700	...
2002 ap	903	5513728	26.8	24.6 ± 1.2	27.8 ± 3.2	≤ 58.7	≤ 82.1	≤ 2.8
2002 ji	748	10796288	46.8	≤ 13.6	≤ 13.2	≤ 228	≤ 834	≤ 230
2003 H	776	11114752	26.8	≤ 83.6	≤ 61.8	≤ 453	≤ 1250	≤ 610
2003 id	314	11775488	26.8	≤ 7.4	18.1 ± 2.6	≤ 15.5	≤ 60.9	≤ 30.3
	489	10553344	26.8	7.2 ± 1.2	≤ 12.8	≤ 28.5	≤ 63.3	≤ 31.6
2003 jg	419	10797568	46.8	≤ 229	≤ 164	≤ 569	≤ 1600	≤ 95
2004 C	480	10798080	46.8	2000 ± 500	1300 ± 300	...	...	...
2004 bm	236	11997440	26.8	≤ 208	≤ 139	1710 ± 350	4970 ± 620	1350 ± 170
	377	11997184	26.8	≤ 229	≤ 147	1490 ± 440	...	...
	767	14458624	26.8	≤ 220	≤ 141	1690 ± 240	4040 ± 390	1100 ± 110

(continued on next page)

Table 4.2. *Spitzer*/IRAC observations and measurements of post-explosion fluxes for the sample of 17 supernovae of types Ib, Ic and Ib/c. See Appendix B for more details. *(continued on next page)*

SN	epoch*	AOR†	$t_{\rm exp}$ / s	F_ν / μJy				$F_\nu(50\,{\rm kpc})^\ddagger$ / Jy
				3.6 μm	4.5 μm	5.8 μm	8 μm	8 μm
(continued from previous page)								
2004 cc	365	10530560	10.4	≤ 427	...	≤ 1720	...	...
		10530816	10.4	...	≤ 345	...	≤ 4760	≤ 490
2005 E	222	14457344	26.8	≤ 3.7	≤ 3.3	≤ 20.2	≤ 51	≤ 24
	388	14457600	26.8	≤ 3.3	≤ 7.6	≤ 53.5	≤ 36	≤ 17
2005 V	989	22000384	26.8	...	≤ 35000	...	...	...
2005 at	569	18285312	26.8	81 ± 20	89 ± 10	175 ± 33	370 ± 90	7.4 ± 1.8
2005 cz	496	18035456	46.8	...	≤ 51	≤ 33	≤ 20	≤ 3.3
2005 kl	941	21760512	26.8	≤ 290	≤ 240	≤ 690	≤ 1700	≤ 320
2006 jc	210	21268224	26.8	501 ± 20	652 ± 26	712 ± 30	654 ± 27	174 ± 7
	412	23113472	26.8	40.8 ± 2.9	96 ± 5.3	179 ± 8	234 ± 10	62.3 ± 2.7
	582	23113728	26.8	3.2 ± 0.6	14.6 ± 1.1	44.1 ± 2.3	78.8 ± 4.5	21.0 ± 1.2
2007 gr	17	24200704	26.8	4720 ± 190	3720 ± 150	2530 ± 100	1620 ± 70	55.9 ± 2.4

* day since discovery; † *Spitzer* Astronomical Observation Request; ‡ flux density scaled to the distance of 50 kpc

Table 4.2. *(continued from previous page)*

The distribution of supernova types in Table 4.3 suggests that supernovae of type Ic are more likely to be detected in the MIR and are more likely to take place in a high-background environment. None of the type Ib supernovae in our sample were detected, but our limited results suggest that they are more likely to take place in a low-background environment. From Table 4.3 it is evident that the type Ib and type Ic supernovae in our sample are found in significantly different environments. Overall, we note that the type Ibc supernovae in our sample are found close to the host galaxy centre, at a median projected radius of $0.2R_{25}$.

Two supernovae, namely, SN 2002ap (Ic) and SN 2005E (Ib), were discovered in remote parts of their host galaxies and were observed on day 903 and day 222, respectively. Because of the low absolute backgrounds and the reduced confusion from the surrounding environment, the estimates derived from these observations may provide the most reliable constraints on dust formation at day $\sim$ 200 for type Ib and at day $\sim$ 900 for type Ic supernovae. The non-detection of SN 2005E on day 222 with no visible emission shows that this supernova was significantly fainter at 8 μm than type II supernovae at similar epochs (e.g. Fabbri et al. 2011). SN 2002ap, on the other hand, was observed on day 903, which is well after the initial decline in brightness and before rebrightening after $\sim$ 1000 days observed for some type II supernovae (e.g. SN 2004et; Sahu et al. 2006, Kotak et al. 2009).

4.4 Spectral energy distributions

Figure 4.2 shows SEDs of three supernovae, SN 2005at, SN 2006jc and SN 2007gr which were detected in three or more wavebands. Corresponding temperatures were obtained from fitting a blackbody, or a modified blackbody function in the form $S_\lambda \propto \lambda^{-\beta} B_\lambda(T)$, where $B_\lambda(T)$ is the Planck function. We used the CMPFIT package (v.1.2; Markwardt 2009) to compute best-fitting temperatures for a blackbody ($\beta = 0$) and a modified blackbody with $\beta = 1$. Table 4.4 shows the best-fitting temperatures along with the total χ^2 values for the two cases. We found that using a modified blackbody with $\beta = 1$ gave a better fit to day 412 and day 582 fluxes for SN 2006jc.

The dust masses can be estimated from the observed temperatures and the observed IR fluxes (Li 2005):

$$M_\mathrm{d} = 2.23 \times 10^8 \times \frac{F_\nu}{\mathrm{Jy}} \times \left(\frac{D}{\mathrm{Mpc}}\right)^2 \times \left(\frac{\kappa_\nu}{\mathrm{cm^2\,g^{-1}}}\right)^{-1} \times \left(\frac{B_\nu(T_\mathrm{d})}{\mathrm{J\,m^{-2}}}\right)^{-1} \tag{4.1}$$

where F_ν is the observed flux density at 8 μm, and D is the distance to the host galaxy.

The dust grain opacity κ_ν is highly dependent on frequency, dust composition, grain size distribution as well as grain shape (Li 2005; Purcell 1969). The opacity of small amorphous grains is predicted to vary as λ^{-1} (Seki & Yamamoto 1980) with a theoretical limit of λ^{-2} (Li 2003), resulting in an overall theoretical range $\beta \approx$ 0–2. Physically, $\beta \sim 0$ corresponds to environments such as circumstellar discs, with large dust grains absorbing as greybodies, while $\beta \sim 2$ is more typical of smaller grains in the ISM (e.g. Miyake & Nakagawa 1993). Therefore, for small grains the Planck function $B_\nu(T_\mathrm{d})$ in Eq. 4.1 is evaluated at the best-fitting modified blackbody temperature T_d obtained for $\beta = 1$.

The opacity κ_ν can be expressed as $\frac{3Q_\mathrm{abs}}{4\rho a}$, where Q_abs is the absorption efficiency of dust grains and ρ is the density. For small grains with $a \lesssim 0.1\lambda$ the quantity Q_abs/a is independent of the grain radius a (e.g. Hildebrand 1983, Draine & Lee 1984). For graphitic dust with

SN	Type	$D^{\star}$ [Mpc]	Field†	$r/R_{25}{}^{\ddagger}$	Epoch§	$S_{5.8}$ [mJy kpc^{-2}]	S_{8} [mJy kpc^{-2}]
			Detections				
2005 at	Ic	7.08	crowded	0.22	569	...	...
2006 jc	Ib/c	25.8	crowded	0.38	210	...	...
2007 gr	Ic	9.29	crowded	0.32	17	...	...
			Non-detections – low background				
2000 ds	Ib	20.8	busy	0.13	2237	0.5	1.5
2002 ap[a]	Ic	9.3	sparse	0.90	903	...	...
2002 ji	Ib/c	26.42	busy	0.52	748	1.7	7.9
2003 H	Ib	35	crowded	0.40	776	2.3	5.3
2005 E	Ib	34	sparse	1.39	222	...	1.2
2005 cz	Ib	20.4	busy	0.09	496	2.8	2.0
			Non-detections – high background				
2001 ci	Ic	16.5	busy	0.11	1075	45	120
2003 jg	Ib/c	12.2	busy	0.06	419	31	93
2004 C	Ic	35	busy	0.20	480	...	...
2004 cc	Ic	16.1	busy	0.09	365	33	97
2005 V	Ib/c	14.5	busy	0.03	989	...	...
2005 kl	Ic	21.6	crowded	0.15	941	32	80
			Non-detections – other				
2003 id[b]	Ic	35.3	crowded	0.34	314	...	...
2004 bm[c]	Ic	26.1	busy	0.11	236	...	...

* distance to host galaxy
† the surrounding field is busy if the background is high and smoothly varying, the field is crowded if the background is not smoothly varying and contains unresolved features
‡ projected distance from host galaxy centre as a fraction of R_{25}, the radius at which the B-band surface brightness falls below 25 mag arcsec^{-2} (R_{25} data from de Vaucouleurs et al. 1991, Corwin et al. 1994 and Nordgren et al. 1997)
§ earliest *Spitzer*/IRAC observation given in days since discovery
[a] observations are part of the SINGS programme (Kennicutt et al. 2003)
[b] faint emission visible, but less than 3σ
[c] the observed emission is constant across three epochs suggesting non-supernova origin; see text for more details

Table 4.3. Summary of results for the sample and measurements of absolute *Spitzer*/IRAC 5.8 and 8 μm background levels for non-detections. Non-detections are grouped into low absolute background and high absolute background cases. Uncertain or inconclusive cases are grouped as other non-detections. See Appendix B for more details.

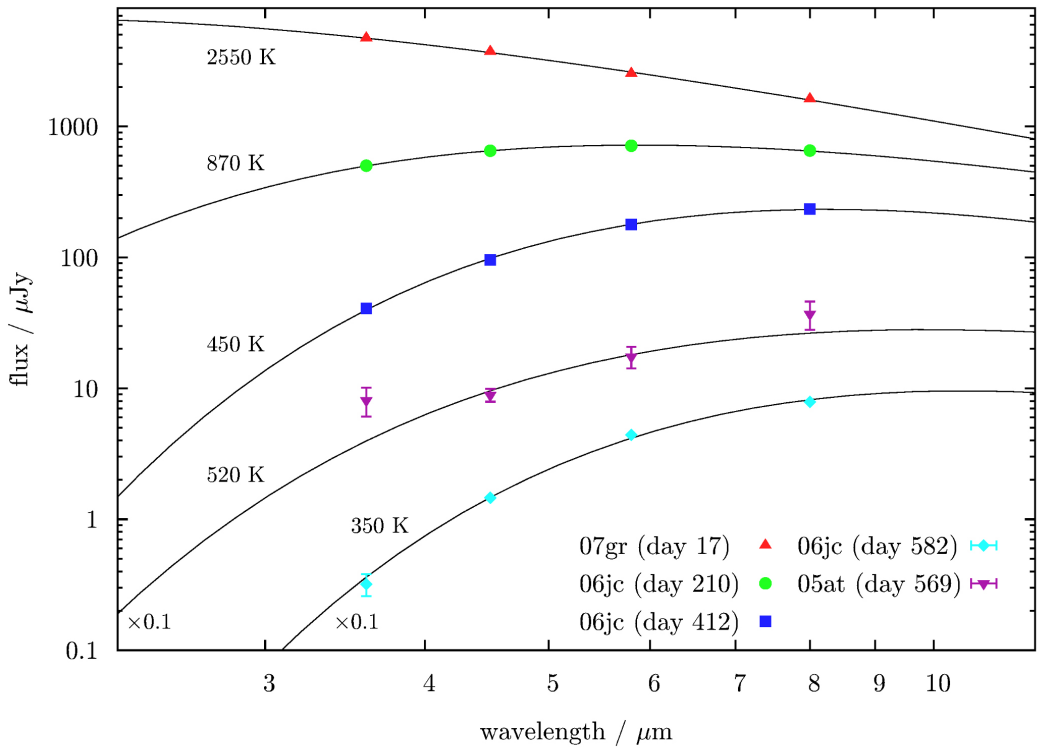

Figure 4.2. Spectral energy distributions of three supernovae at five epochs, as observed in the MIR by *Spitzer*/IRAC. Blackbody fits (solid lines) and best-fitting temperatures ($T_{\mathrm{(m)bb}}$) are also indicated. The data and the lines of best fit for SN 2005at (day 569) and SN 2006jc (day 582) were scaled by a factor of 0.1 for clarity. Uncertainties smaller than the symbol size are not shown.

SN	Type	Epoch*	T_{bb} [K]	$T_{\mathrm{mbb}}(\beta = 1)$ [K]
2005at	Ic	569	520 ± 60 [$\chi^2 = 6.1$]	(430 ± 40) [$\chi^2 = 7.2$]
2006jc	Ib/c	210	870 ± 20 [$\chi^2 = 0.1$]	(650 ± 10) [$\chi^2 = 5.3$]
		412	(540 ± 20) [$\chi^2 = 1.3$]	450 ± 10 [$\chi^2 = 0.3$]
		582	(400 ± 20) [$\chi^2 = 5.6$]	350 ± 20 [$\chi^2 = 2.1$]
2007gr	Ic	17	2550 ± 250 [$\chi^2 = 0.8$]	(1200 ± 50) [$\chi^2 = 7.2$]

* day since discovery

Table 4.4. Best-fitting blackbody temperatures (T_{bb}) or modified blackbody temperatures (T_{mbb}) for three supernovae at five epochs. The corresponding total χ^2 values are indicated in square brackets.

SN	Epoch*	T_d [K]	M_mbb [$10^{-5}\,\mathrm{M}_\odot$]	M_87A [$10^{-5}\,\mathrm{M}_\odot$]
2005at	569	430	19^{+0}_{-14}	20
2006jc	210	650	100^{+20}_{-60}	3.7
	412	450	130^{+40}_{-70}	11
	582	350	140^{+60}_{-70}	61

* day since discovery

Table 4.5. Graphitic dust masses derived from *Spitzer*/IRAC 8 μm fluxes and modified blackbody temperatures (M_mbb) and dust masses derived from *Spitzer*/IRAC 8 μm fluxes assuming dust formation properties of SN 1987A (M_87A; Table 4.7). Variations resulting from the choice of the reference wavelength and the assumed dust species are indicated as uncertainties.

$\rho = 2.25\,\mathrm{g\,cm^{-3}}$ and $Q_\mathrm{abs}(\lambda = 8\ \mu\mathrm{m},\ a = 0.01\ \mu\mathrm{m})/a = 1.2 \times 10^3\ \mathrm{cm^{-1}}$ the opacity evaluates to $\kappa_{8\,\mu\mathrm{m}} = 400\ \mathrm{cm^2\,g^{-1}}$ (Draine 1985).

Table 4.5 presents dust masses derived using Eq. 4.1 for graphite. We repeated our calculations for $\lambda = 5.8$ μm, as well as for silicate dust (Draine 1985). The resulting differences in the derived dust masses are indicated in Table 4.5 as uncertainties. SN 2007gr was not included in the calculations because a temperature of $\sim$ 2600 K is much higher that the condensation temperature of dust grains (1000–2000 K; e.g. Salpeter 1977, Todini & Ferrara 2001).

SN 2004bm

The detections attributed to SN 2004bm (Table 4.2) are high compared to similar detections of other supernovae. The available images at UV, optical and NIR wavelengths from *GALEX* and SDSS were inspected and showed that the point-like emission seen at the *Spitzer* wavebands (Figure B.1) does not have a counterpart at shorter wavelengths. We fitted blackbody and modified blackbody profiles to the 4.6 μm upper limit and the 5.8 and 8 μm detections for days 236 and 767. The resulting fits were better for a modified blackbody with $\beta = 1$ and suggested a dust temperature of $\sim$ 250 K for both epochs. Since a temperature decrease was not observed between day 236 and day 767, and fluxes remained approximately constant across three epochs (Table 4.2), we conclude that it is likely that pre-existing dust makes a significant contribution to the observed 5.8 and 8 μm fluxes. As noted in Appendix B, SN 2004bm is located near the centre of NGC 3437 where significant uncertainties arise from background subtraction. Overall, our results suggest that the observed emission does not originate from SN 2004bm.

4.5 Mid-infrared fluxes and dust masses

In dust studies of type II supernovae, photometric as well as spectroscopic data have been used to model the dust emission in the MIR in order to derive the mass of dust formed in the ejecta (e.g. Section 4.4, but also see Wooden et al. 1993, Sugerman et al. 2006, Ercolano et al.

Epoch	$F_{8.38}$ [Jy]	$M_{\rm dust}$ (Wooden et al. 1993) Large grains $[10^{-5}\,{\rm M}_\odot]$	Graphite* $[10^{-5}\,{\rm M}_\odot]$	$M_{\rm dust}$ (Ercolano et al. 2007) Am. carbon† $[10^{-5}\,{\rm M}_\odot]$	Graphite† $[10^{-5}\,{\rm M}_\odot]$
60	46.50 ± 4.29	0.06	...	...	...
260	24.18 ± 1.34	1.08	...	...	...
415	$12.85 \pm 0.65^\ddagger$	0.17	2.4	...	...
615	8.86 ± 0.65	3.67	31	21	54
775	$1.02 \pm 0.23^\ddagger$	5.93	50	31	60

* clumpy model; † middle of the range for smooth and clumpy models; ‡ interpolated

Table 4.6. SN 1987A ESO 8.38 μm fluxes (Bouchet et al. 1989; Bouchet & Danziger 1993) and derived dust masses. The shaded area indicates the values adopted in this study.

2007, Meikle et al. 2007, Mattila et al. 2008, Kotak et al. 2009, Meikle et al. 2011, Fabbri et al. 2011). Due to the scarcity of late-time photometric and spectroscopic observations of type Ibc supernovae in the MIR, a similar approach for these supernovae is not feasible for all supernovae in our sample. Instead, we compared the photometric measurements at 8 μm for our sample with similar measurements of well-studied type II supernovae at similar epochs. The ratio of the observed absolute IR fluxes was used to scale from the dust mass derived for type II supernovae at a given epoch.

Table 4.6 provides a summary of the dust masses derived for SN 1987A in the LMC (e.g. Waldrop 1987). The estimates presented in Table 4.6 depend on the degree of clumpiness and the chemical composition of dust. In this work, we adopt for days 60 and 260 estimates tabulated by Wooden et al. (1993) and computed for large grains. For days 415, 615 and 775, we adopt their estimates computed for a clumpy graphite model, which are consistent with the results of Ercolano et al. (2007). We note that the 8 μm lightcurve of another well-studied type II supernova, SN 2004et, closely follows that of SN 1987A and the derived dust masses for SN 1987A and SN 2004et are similar at corresponding epochs (e.g. Fabbri et al. 2011, Kotak et al. 2009).

For this analysis we selected only those detections and upper limits at 8 μm which can impose useful constraints, i.e. those that lie within a factor ~ 100 of the lighcurve of SN 1987A. Figure 4.3 shows the selected measurements, scaled to the LMC distance of 50 kpc (Inno et al. 2013) and plotted together with the 8 μm lightcurve of SN 1987A (Bouchet et al. 1989; Bouchet & Danziger 1993).

Figure 4.3 shows detections of SN 2005at (Ic), SN 2006jc (Ib/c) and SN 2007gr (Ic) at five epochs and 3σ upper limits of SN 2003id (Ic), SN 2003jg (Ib/c), SN 2005E (Ib) and SN 2005cz (Ib) at six epochs. Overall, type Ib supernovae appear to be fainter than SN 1987A and type Ic supernovae appear to be comparable to SN 1987A at 8 μm.

The relative brightnesses of the scaled measurements shown in Figure 4.3 compared to the corresponding measurements of SN 1987A can be used to extrapolate from dust mass estimates for SN 1987A to derive estimates for dust formation in supernovae of type Ibc. Table 4.7 presents dust masses derived from the measurements shown in Table 4.2, using SN 1987A fluxes from Bouchet et al. (1989) and Bouchet & Danziger (1993), and the dust emission models of Wooden et al. (1993), implicitly assuming that the dust formation and destruction mechanisms in type Ibc ejecta are similar to those in type II ejecta.

Table 4.7 provides upper limits to the amount of dust formed for type Ib ejecta of 1–

$4 \times 10^{-5}\,M_{\odot}$, based on three epochs, at days 200–500. The dust mass estimate for the type Ic ejecta is $\sim 30 \times 10^{-5}\,M_{\odot}$, also based on three epochs, at days 500–600. The estimate for SN 2006jc (type Ib/c) is 4–$60 \times 10^{-5}\,M_{\odot}$ between days ~ 200 and ~ 600.

We emphasise that due to very limited observational data in the MIR, these dust mass estimates were determined indirectly, based on representative dust mass models for SN 1987A and assuming the general properties of SN 1987A. The number of non-detections at early epochs in busy fields (e.g. SN 2003jg and SN 2004cc), and, especially, the non-detection of SN 2005E at day 222 in a sparse field (Table 4.3) suggest that not only do type Ibc ejecta in our sample not produce enhanced MIR emission that could be attributed to enhanced dust formation, but SN 2005E, SN 2005at and SN 2005cz are in fact intrinsically fainter than SN 1987A in the MIR. Since type Ibc supernovae are typically more energetic than type II supernovae (e.g. Dessart et al. 2011, Salas et al. 2013) and dust may not survive as easily in dense environments (Bianchi & Schneider 2007), the net amount of dust injected into the ISM may be significantly lower than the estimate presented in Table 4.7.

In comparison with our calculations presented in Table 4.5, the estimates based on the properties of SN 1987A are significantly lower, except for SN 2005at, for which the estimate for graphitic dust is consistent with the estimate derived from SN 1987A.

We note that the dust masses shown in Table 4.5 were derived using Eq. 4.1 and through the best-fitting blackbody temperature take into account the shape of the MIR emission. While those estimates are better founded on the MIR observations than the estimates based only on the 8 μm flux, it must be emphasised that a range of results can obtained depending on the assumed optical properties of dust. More reliable results can be obtained using radiative transfer models taking into account physical properties of each individual supernova.

SN 2006jc

SN 2006jc has been the subject of extensive studies. It was discovered in UGC 4904 on 9 Oct 2006 as a type Ib/c supernova (Nakano et al. 2006; Itagaki et al. 2006). Early-time optical observations and associated UV and X-ray detections suggested the interaction of the supernova shock with a dense shell of He-rich material deposited by a proposed progenitor Wolf-Rayet star (Foley et al. 2007; Immler et al. 2008; Pastorello et al. 2008; Anupama et al. 2009; Chugai 2009). Photometric observations showed a decline in NIR brightness and drop in temperature from ~ 3000 K to ~ 1000 K between days 36 and 180, which together with the asymmetric and blueshifted He I emission lines suggested formation of hot dust as early as at day 50–100 (Di Carlo et al. 2008; Smith et al. 2008; Anupama et al. 2009). Models including MIR observations were interpreted as pointing to early amorphous carbon condensation, at temperatures 600–1000 K, on days 40–60 after the explosion, followed by the condensation of silicates until day ~ 200 (Mattila et al. 2008; Nozawa et al. 2008; Tominaga et al. 2008; Sakon et al. 2009).

If all the dust is assumed to have formed after the explosion, the estimated dust masses at day ~ 200 range from 7–$800 \times 10^{-5}\,M_{\odot}$ (Sakon et al. 2009; Nozawa et al. 2008; Mattila et al. 2008). Our derived dust masses of 4–$60 \times 10^{-5}\,M_{\odot}$ (Table 4.7) and our calculations suggesting 100–$140 \times 10^{-5}\,M_{\odot}$ for days 210–582 (Table 4.5) are broadly consistent with these estimates.

However, Mattila et al. (2008) suggested that the bulk of the observed MIR emission at later epochs can be explained as an IR echo from a pre-existing dust mass of $800 \times 10^{-5}\,M_{\odot}$

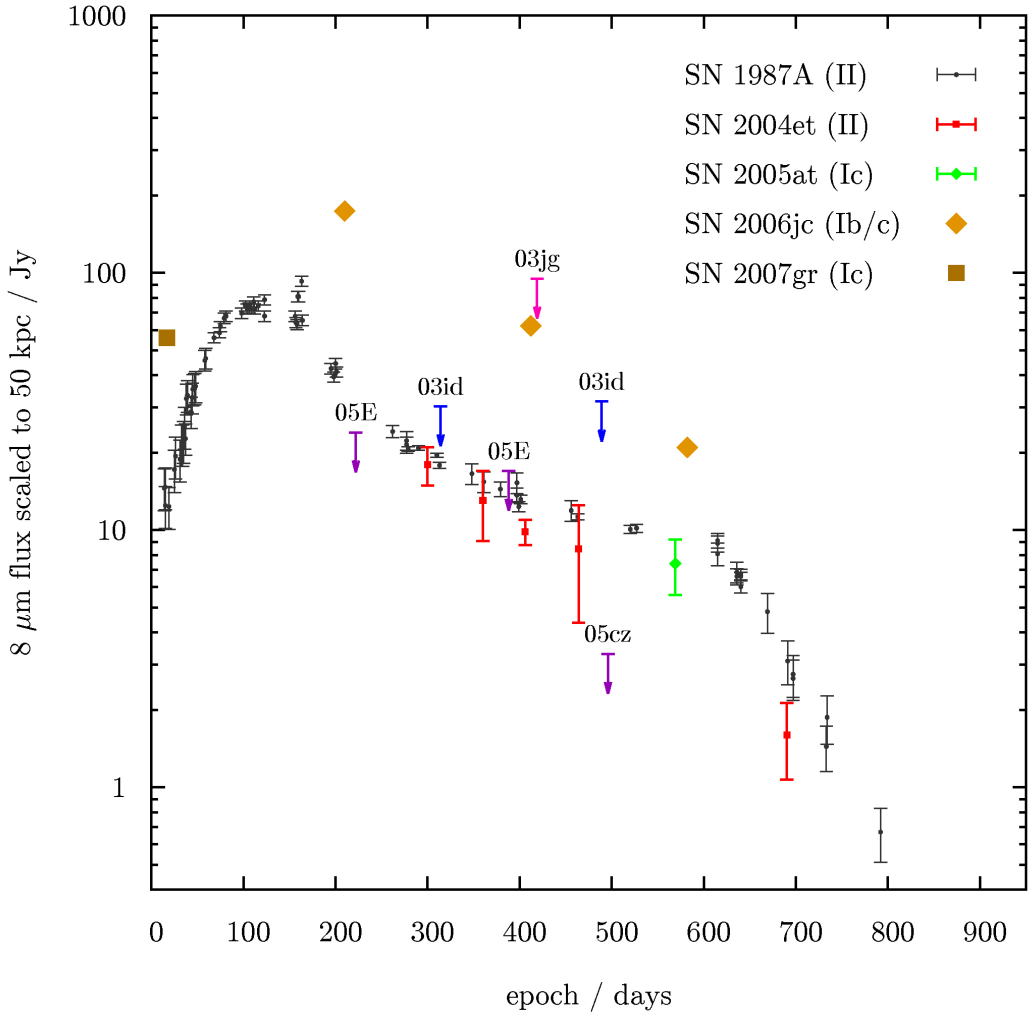

Figure 4.3. Detections and upper limits at 8 μm scaled to 50 kpc for seven supernovae of types Ib, Ic and Ib/c. Only the most constraining upper limits are shown. The 8 μm lightcurve of SN 1987A (Bouchet et al. 1989; Bouchet & Danziger 1993) and of SN 2004et (Fabbri et al. 2011) are shown for comparison. The arrows denoting 3σ upper limits are colour-coded according to supernova types: Ib in purple (05E and 05cz), Ic in blue (03id) and Ib/c in pink (03jg). The uncertainties for SN 2006jc and SN 2007gr are comparable with the symbol sizes.

SN	Type	Epoch*	$F(50\,\mathrm{kpc})_8$ † [Jy]	$F(87\mathrm{A})_{8.38}$ ‡ [Jy]	Background	M_{dust} [$10^{-5}\,\mathrm{M}_\odot$]
			Fainter than SN 1987A			
2005 E	Ib	222	≤ 24	35.4 ± 1.7	low	≤ 0.6
		388	≤ 17	14.0 ± 0.9	low	≤ 2.6
2005 at	Ic	569	7.4 ± 1.8	9.2 ± 0.4	detection	20
2005 cz	Ib	496	≤ 3.3	10.6 ± 0.3	low	≤ 4.4
			Brighter than SN 1987A			
2006 jc	Ib/c	210	174 ± 7	38.7 ± 1.8	detection	3.7
		412	62.3 ± 2.7	12.9 ± 0.6	detection	11
		582	21.0 ± 1.2	9.0 ± 0.5	detection	61
2007 gr	Ic	17	55.9 ± 2.4	13.0 ± 2.0	detection	...
			Brighter or fainter than SN 1987A			
2003 id	Ic	314	≤ 30	17.8 ± 0.5	^{a}	≤ 2.6
		489	≤ 32	10.7 ± 0.3	^{a}	≤ 39
2003 jg	Ib/c	419	≤ 95	12.8 ± 0.7	high	≤ 22

* day since discovery
† *Spitzer*/IRAC 8 μm flux scaled to the distance of 50 kpc
‡ corresponding interpolated ESO 8.38 μm flux measured for SN 1987A (Bouchet et al. 1989; Bouchet & Danziger 1993)
^{a} faint supernova emission visible, but less than 3σ

Table 4.7. Dust masses derived for type Ibc ejecta. Dust masses were estimated by applying a factor of $F(50\,\mathrm{kpc})_8/F(87\mathrm{A})_{8.38}$ to dust mass estimates for SN 1987A from Wooden et al. (1993), interpolated to the epoch of observation.

produced in the wind of a Wolf-Rayet progenitor, in which case a significant fraction of the dust mass estimated for SN 2006jc (Tables 4.5 and 4.7) may have been formed in stellar outflows from the progenitor rather than in the supernova ejecta. Our dust mass estimates for other supernovae similarly assume that all their dust has formed in the ejecta.

Environments

Type Ic supernovae have been suggested to trace H II regions, implying that they originate from higher mass progenitors than type II or type Ib supernovae (Anderson & James 2008). Similarly, Kelly et al. (2008) found that type Ic supernovae are more likely than other supernova types to be associated with the brightest regions in their host galaxies, possibly also associated with slightly higher metallicites (Leloudas et al. 2011).

The background measurements for the non-detections in our sample, presented in Table 4.3, confirm that type Ib and type Ic supernovae are found in different environments. Our limited results also confirm that the type Ic supernovae are associated with bright, high-background environments, which are close to the host galaxy centre.

4.6 Conclusions

Based on photometric observations in the MIR acquired with *Spitzer*/IRAC, we examined a sample of 17 type Ibc supernovae to estimate the mass of dust that may have formed in the ejecta, by assuming that they are similar to SN 1987A in their dust formation properties.

The observed 8.38 μm fluxes together with published dust models for SN 1987A were used to compute dust masses or upper limits for seven type Ibc supernovae for which *Spitzer*/IRAC 8 μm data were available. Additionally, the SEDs of two supernovae at four epochs were constructed and dust masses estimated using a simple model.

We found that out of the four type Ib supernovae in our sample, none were detected at 8 μm and all took place in low absolute infrared background environments. We note in particular that no emission was visible in SN 2005E at day 222 in a sparse field and the 3σ upper limit for SN 2005cz at day 496 is a factor of ~ 3 lower than the brightness of SN 1987A at this epoch. Therefore, our results suggest that type Ib supernovae are fainter in the MIR than type II supernovae at similar epochs. The upper limit to the dust masses produced in type Ib ejecta is estimated at $\sim 4 \times 10^{-5}\,\mathrm{M}_{\odot}$ by day ~ 500.

Nine supernovae in our sample were of type Ic, of which two were detected at 8 μm. For the non-detections, most explosions took place in high absolute infrared background environments. We found that the 8 μm emission of the type Ic supernovae is comparable to that expected from the lightcurve of SN 1987A, which suggests similar yields of dust. Together with our calculations for SN 2005at, the dust mass produced in type Ic ejecta is estimated at $\sim 20 \times 10^{-5}\,\mathrm{M}_{\odot}$ by day ~ 500.

Our sample included four supernovae of the intermediate class Ib/c, of which one was detected at 8 μm. For the non-detections, most explosions took place in high absolute infrared background environments. The measurements of SN 2006jc suggest that type Ib/c supernovae are generally brighter than type II. Together with our calculations shown in Table 4.5, we estimate the dust mass produced by day ~ 600 to be 60–140 $\times 10^{-5}\,\mathrm{M}_{\odot}$, but we note that the 8 μm emission may be contaminated by emission from pre-existing dust (cf. Mattila et al. 2008).

Overall, these results are low compared to $\sim 1\,\mathrm{M}_{\odot}$ per supernova required to account for all dust in the early Universe (e.g. Dwek et al. 2011b), but late-time dust growth similar to that in SN 1987A (Matsuura et al. 2011) cannot be ruled out.

5 Conclusions and future work

In this work, we have studied dust and star formation in NGC 4449, as well as the dust formation in type Ibc supernovae.

In Chapter 2 we presented a complete SED of NGC 4449 from the FUV to the sub-mm, including new observations acquired by *Herschel*. In Section 2.3.5 we modelled global dust formation to find the likely chemical composition of dust in the ISM of NGC 4449. Our analysis of the global optical spectrum presented in Section 2.3.4 suggests an early onset of star formation approximately 12 Gyr ago.

These results were used as constraints in constructing a photoionization and radiative transfer MOCASSIN model of NGC 4449. The iterative scheme presented in Section 2.3.7 allowed us to infer the presence of a very young stellar population with a mass of 3×10^6 $M_\odot$. Our detailed spectroscopic *Spitzer* data presented in Section 3.7 indicate that these young populations reside primarily in the centre, in the SW and in the N of NGC 4449. The derived global recent star formation rate is 0.4 $M_\odot\,yr^{-1}$, in agreement with previous estimates.

We note that our scheme is particularly suitable for deriving integrated properties of galaxies, such as the total mass of dust, the total mass of stars and the total stellar luminosity. The spatial distribution of the nebular emission, of the PAH band emission and of the fine-structure line emission presented in Chapter 3 reveal that NGC 4449 is a complex and dynamic system and confirm that a spherically-symmetric model, which assumes one ISM phase, cannot be reliably used to study the inner structure of this galaxy.

In comparison with similar galaxies, the overall dust to gas ratio derived for NGC 4449 in Section 2.4.2 is extremely low, which supports our hypothesis from Section 3.5.5 that the atomic and molecular gas is partially disconnected from the H II regions and PDRs probed by our observations. The stripe of enhanced neutral gas density and reduced ISRF strength to the north of the optical centre of NGC 4449 inferred from the PDR models of Kaufman et al. (1999, 2006) coincide with an arc of enhanced heating efficiency and also with a gradient in atomic gas density, and may contain a reservoir of gas which may host future star formation activity.

The PAH emission discussed in Section 3.5.1 shows that the bands centred at 6.2, 7.7 and 8.6 μm are tied together and, relative to the 11.3 μm complex, probe PAH ionization. We note a deficit of ionized PAHs near the centre of NGC 4449. Since ionized PAHs are found in regions with lower ISRF, it is possible that ionized PAHs near the centre are mixed with a considerable mass of coinciding neutral PAHs. Alternatively, the PDRs near the centre may offer more efficient self-shielding resulting from a relatively high metallicity and dust abundance.

In Section 3.5.4 we presented the balance of heating and cooling within NGC 4449 at a resolution of 220 pc. Our results showed that none of the observed FIR cooling lines described the ISM cooling consistently within the galaxy. However, $[O\,III]_{88}$ dominates the cooling in the most prominent H II regions, and $[O\,III]_{88}$ + $[C\,II]_{158}$ well describe the ISM cooling in the north. In a diffuse region to the north of the centre, ISM cooling is likely to be dominated by

another coolant at the resolution of our observations. Our results suggest that the different ISM phases, where the individual coolants operate, are likely to be mixed within the telescope beam.

In addition, we examined a sample of individual supernovae and found that the estimated dust masses produced by day ~ 600 are too low to consider type Ibc supernovae as major dust producers in the early Universe. In particular, in Section 4.3 we report the detection of two type Ic, one type Ib/c but no type Ib supernovae from our sample. Our limited sample also indicates that type Ib and type Ic supernovae may take place in significantly different environments.

Future work

The wealth of spatially resolved data presented in Chapter 3, together with the integrated properties of NGC 4449 presented in Chapter 2 create a unique opportunity to construct a fully three-dimensional MOCASSIN model of this galaxy. A low resolution model with grid refinements near the most prominent star-forming regions is computationally feasible.

At the same time, higher spectral resolution global optical observations would allow a more accurate analysis of the older stellar populations. The old stellar populations could then be incorporated into the three-dimensional models as an underlying diffuse stellar component, separate from localised H II regions formed by young populations. Such a model could highlight the differences in the stellar populations and in the dust content across a number of regions within NGC 4449.

The interpretation of our results could be greatly aided through accurate metallicity determinations across the disc of NGC 4449. The deficit in the $I_{7.7}/I_{11.3}$ PAH band ratio near the centre as well as the arc of enhanced heating efficiency may be correlated with metallicity. Similarly, high resolution observations in H I or CO may uncover neutral gas components clearly associated with the arc. Although individual PDRs are not resolved in our data, the balance of gas heating and cooling could be studied further with additional cooling lines included, for example [S III]$_{33.5}$.

Applications in galaxy studies

We have noted that a spherically-symmetric model of a galaxy can be used to estimate its global parameters. In particular, the derived global properties of stellar populations can be considered reliable because they are matched against line emission from ionized gas.

However, in models which include a careful treatment of gas, the distribution of stars and the three-dimensional physical and chemical structure of a galaxy are necessarily simplified due to computational and observational limitations (Fig. 5.1, top). This results in an 'onion skin' view of a galaxy, with individual layers representing the different physical environments required to match all observables (also see Section 2.4.3). On the other hand, models reproducing the observed stellar emission are not constrained by the associated emission from ionized and neutral gas (Fig. 5.1, bottom). Therefore, current models simplify either geometry or physical and chemical composition, thus inevitably limiting their interpretative power.

The importance of spatially-resolved analysis of gas emission within galaxies is evident from the results presented in Section 3.5.4. While the observations have insufficient resolution to fully explain the energy balance in the ISM of NGC 4449, the nature of the trends visible in

Fig. 3.16 may be interpreted with the aid of three-dimensional models. Such models could be analysed at a range of resolutions to show if any of the visible trends may be attributed to the intrinsic geometry or to observational factors, such as the instrumental resolution.

The three-dimensional distribution of stars and star clusters within a galaxy forms a filamentary structure, with the interconnected H II regions and PDRs and isolated clouds of cool molecular gas (cf. Fig. 1.1). Therefore, in constructing three-dimensional representations of galaxies, the classical ISM structure around a star shown in Fig. 1.2 is no longer adequate, as in reality PDRs and molecular clouds are illuminated from all directions. For this reason, complete models of galaxies including stars, gas and dust treated in a self-consistent way pose a computational challenge.

The first step in addressing this challenge could be to apply the existing modelling tools locally to assemble a galaxy bottom-up, adopting closed star-free volumes of gas as building blocks. Defining the building blocks in this way allows PDRs to be carefully separated from naturally spherical H II regions around stars or star clusters. The PDRs and the molecular gas could then be readily modelled with the recently introduced three-dimensional PDR code 3D-PDR (Bisbas et al. 2012). Together with a treatment of H II regions and post-processing with a radiative transfer code to account for the presence of interstellar dust, such a scheme could be the first attempt to construct a complete model of a galaxy.

The integrated emission resulting from a library of similar models could in turn be used to interpret spectrophotometric observations at high redshifts, where no spatial information is available. While *fitting* the integrated SED with a number of templates may be compared to constructing an 'onion skin' model, more valuable insight to the physical and chemical makeup of a galaxy may be achieved by selecting the best-*matching* model instead. With the on-going development of three-dimensional codes and the continuous increase in the available computing power, such schemes may soon become computationally feasible.

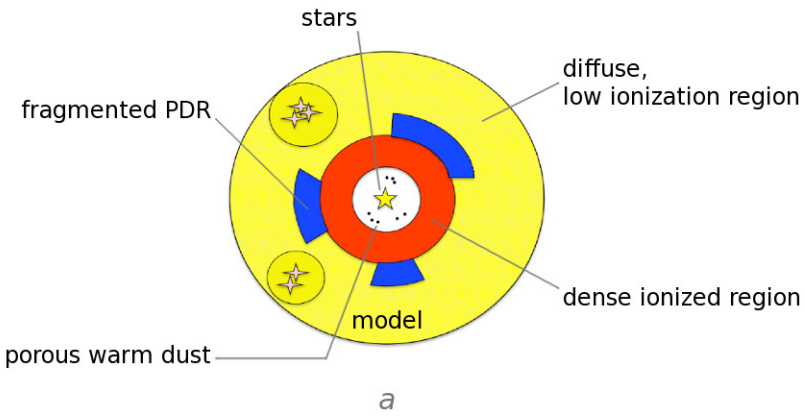

Figure 5.1. Examples of current models of galaxies. In models describing the gas content of a galaxy, the physical structure is necessarily simplified *(a)*. Models accurately describing the distribution of stars and dust within a galaxy are not matched against the observed gas emission *(b)*. The images show models of the galaxies Haro 11 (Cormier et al. 2012) and NGC 4565 (De Looze et al. 2012), respectively.

Acknowledgements

This work was made possible through funding provided by the UCL's Institute of Origins which was created to 'promote world-leading research into the Origins and Evolution of the Universe, the basis of life and how we came to exist'.

I would like to offer special thanks to my supervisors, Prof Mike Barlow (UCL) and Prof Mat Page (UCL/MSSL), for sharing their knowledge and experience and for their support throughout my time at UCL.

List of abbreviations

2MASS Two Micron All Sky Survey
AGB asymptotic giant branch
AOR [*Spitzer*] Astronomical Observation Request
CCD charge-coupled device
CCSN core-collapse supernova
DGR dust to gas ratio
DGS Dwarf Galaxy Survey
ESO European Southern Observatory
FIR far-infrared
FOV field-of-view
FUV far-ultraviolet
FWHM full width at half maximum
IFU integral field unit
IMF initial mass function
IRAC [*Spitzer*] InfraRed Array Camera
IRS [*Spitzer*] InfraRed Spectrograph
ISM interstellar medium
ISRF interstellar radiation field
LMC Large Magellanic Cloud
MIPS Multiband Imaging Photometer for *Spitzer*
MIR mid-infrared
MOCASSIN MOnte CArlo SimulationS of Ionized Nebulae
NIR near-infrared
NUV near-ultraviolet
PACS [*Herschel*] Photodetector Array Camera and Spectrometer
PAH polycyclic aromatic hydrocarbons
PDR photo-dissociation region
PSF point spread function
S/N signal to noise
SDSS Sloan Digital Sky Survey
SED spectral energy distribution
SFH star formation history
SFR star formation rate
SN supernova
SPIRE [*Herschel*] Spectral and Photometric Imaging REceiver
SSP single stellar population
UVOT [*Swift*] Ultraviolet/Optical Telescope

A Photometry of extended sources with Swift/UVOT

The work described in this chapter was published in MNRAS as Appendix A to 'A multi-wavelength study of the Magellanic-type galaxy NGC 4449 – I. Modelling the spectral energy distribution, the ionization structure and the star formation history' (see Chapter 2).

A.1 Introduction

The Ultraviolet/Optical Telescope (UVOT; Roming et al. 2005) is one of three instruments on board *Swift* (Gehrels et al. 2004) designed to detect and observe gamma-ray bursts and their afterglows in seven optical and ultraviolet bands. To this end, the instrument is sensitive to single-photon events and the data reduction software has been tailored to point-source observations. However, with its FOV of $17' \times 17'$, the UVOT can also be of interest for studies of extended sources. Although this FOV is considerably smaller to that of *GALEX* (Martin et al. 2005), the UVOT offers a higher angular resolution, with PSFs of only $2\farcs4$–$2\farcs9$ for the three UV bands (*uvw2*, *uvm2* and *uvw1*) covering a comparable wavelength range to one of the two *GALEX* bands (Fig. A.1; Morrissey et al. 2005; Breeveld et al. 2010).

Obtaining reliable photometric measurements for extended sources poses a technical challenge, which is inherent to the design of the UVOT. The signal from each incoming photon is electronically multiplied to generate a splash of photons at the CCD stage of the UVOT detector, and the centroid of the splash gives positional information to a sub-CCD-pixel accuracy. However, the photon-counting detector has a readout rate of ~ 90 s^{-1}, which leads to systematic undercounting ('coincidence loss' or 'pile-up') when two or more photons arrive in a similar location on the detector within one frame. In such case, the photons are not only counted as one, but the detection is also misplaced by the centroiding algorithm. At count rates of ~ 10 s^{-1} this effect results in a 10 per cent loss in the number of counts (Poole et al. 2008).

High-background cases of point-source observations can be viewed as close analogues of extended sources. A range of background levels was investigated in the models of Breeveld et al. (2010), who showed that backgrounds higher than ~ 0.07 s^{-1} per unbinned image pixel can no longer be fully corrected for coincidence loss without introducing an additional linear correction factor at each affected pixel. This limiting count rate was used by Hoversten et al. (2011) in their analysis of M81 to highlight regions for which coincidence loss is significant. Those regions in M81 coincided with point-like star-forming knots and could be corrected individually as point sources in the low background regime. However, NGC 4449 is a dwarf starburst galaxy, where the star formation activity, comparable to that of M81 (Gordon et al. 2004), is localised in a relatively small volume of space. The UV count rates in NGC 4449 are high throughout the galaxy, as illustrated in Fig. A.2, making a similar approach not

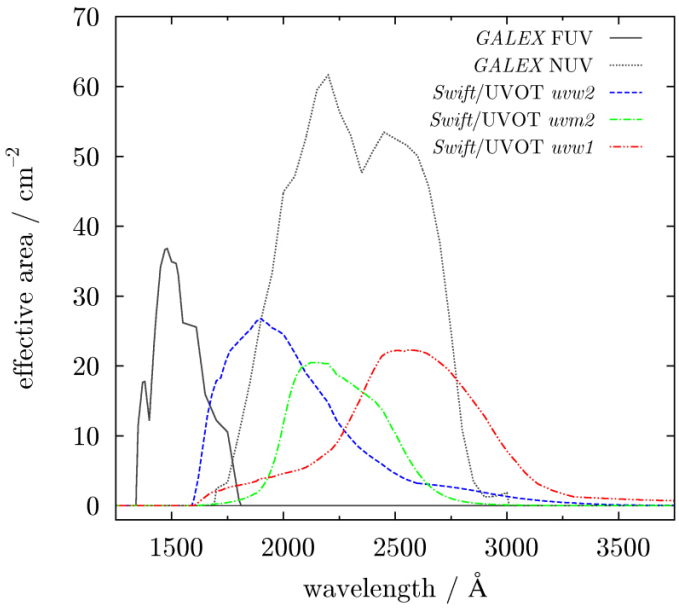

Figure A.1. Broad-band effective passbands for UV observations with *GALEX* and *Swift*.

feasible.

Any method of obtaining photometry must take into account the variation of emission across the UVOT image, as areas with higher count rates suffer from a greater coincidence loss and require a greater correction. However, coincidence loss cannot be corrected for on a pixel-by-pixel basis because the counts in neighbouring pixels are not independent of each other. The position of each count in the image is calculated from a photon splash over five or more physical CCD pixels. Consequently, all counts within the same CCD pixel (64 image pixels) have been detected through similar photon splashes over the same area of the CCD. In the coincidence loss regime individual detections in a particular area on the detector are not independent of each other and should be considered collectively for coincidence loss correction.

A.2 Isophotal correction

We used NASA's HEAsoft (v6.7; released on 2009-08-19) to obtain corrected photometry for three UV and three optical bands in NGC 4449. The *white* band was excluded from this study. The task UVOTSOURCE was run repeatedly with two user-defined apertures: one enclosing a region of interest (or 'source') and one defining the background.

The aperture size recommended for UVOT photometry is 5″ (Poole et al. 2008). By default, if the source aperture is greater than 5″, the coincidence loss correction factor is determined from a 5″ circular region at the centre of the user-defined aperture. Consequently, for larger apertures the default procedure is likely to give a significantly biased corrected count rate, depending on features present in the central area of the user-defined aperture. Therefore, it is expected that UVOTSOURCE is generally not applicable 'as-is' to sources of angular extent greater than the size of the standard 5″ aperture.

In the method presented below, the image was divided into regions following suitably

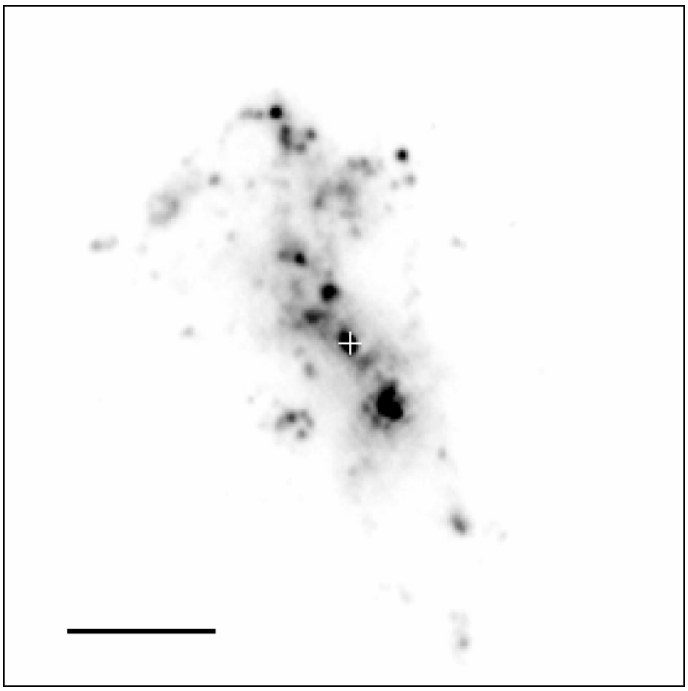

Figure A.2. Regions affected by coincidence loss in the *uvw2*-band image of NGC 4449. White indicates no coincidence loss. North is up, east is to the left. The bar is $1'$ in length and the cross denotes the optical centre of the galaxy.

chosen isophotal contours. The coincidence loss correction factors were determined from representative $5''$ 'test' apertures and applied to correct photon count rates in the corresponding regions. Afterwards, the background was subtracted and the count rates were summed to give the total count rate. An illustration of this isophotal setup is given in Fig. A.3. Region 1 in Fig. A.3 encloses areas with count rates above the threshold of 0.028 s^{-1} per pixel for 2×2 binning, where the effects of coincidence loss become non-negligible (Breeveld et al. 2010; Hoversten et al. 2011). Regions 2–4 in Fig. A.3 enclose areas with count rates of 0.1, 0.2 and 0.3 s^{-1} per pixel. Finally, region 0 is an ellipse enclosing the entire galaxy but not aligned with its optical centre.

Measurements in all individual regions were performed by running the HEAsoft command:

```
uvotsource image=image_sk_coadd.fits \
           expfile=image_ex_coadd.fits \
           srcreg=REGION.reg bkgreg=bkg.reg \
           apercorr=NONE centroid=NO clobber=NO \
           frametime=0.0110329 output=ALL sigma=5 \
           syserr=YES outfile=photometry.fits
```

where `REGION.reg` is a description of *(i)* a test region 0–4, or *(ii)* one of the regions comprising regions 0–4 in Fig. A.3. It is useful to define A, $C_{\mathrm{r(,err)}}$, $C_{\mathrm{test(,err)}}$, f_{test} and $C_{\mathrm{bkg(,err)}}$ based on the following columns in the output FITS table:

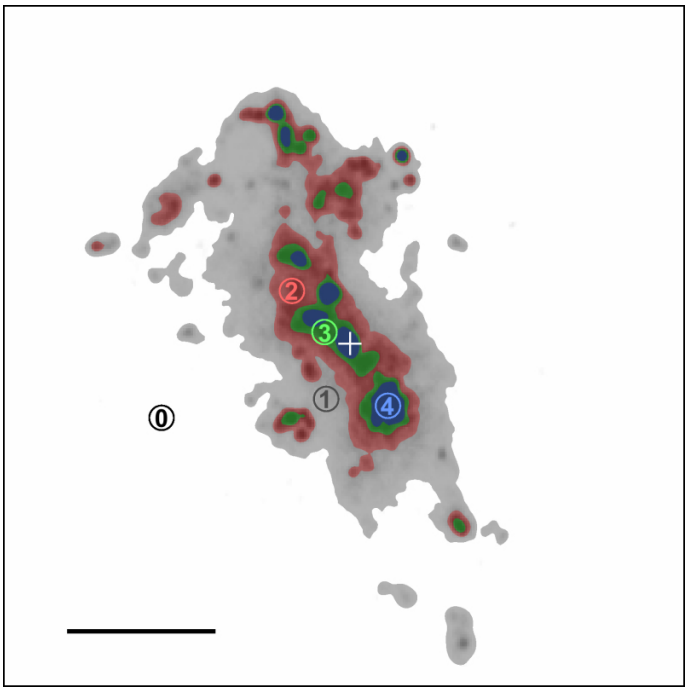

Figure A.3. The isophotal setup for the *uvw2*-band image of NGC 4449. Four isophotal regions numbered 1–4 are shown in grey, red, green and blue, respectively. Region 0, enclosed by an ellipse, and a background aperture defined as an elliptical annulus, both extend beyond the image and are not shown for clarity. The test regions are indicated by 5″ circles. North is up, east is to the left. The bar is 1′ in length and the cross denotes the optical centre of the galaxy.

`SRC_AREA`	area of the source aperture in arcsec^2, A
`RAW_TOT_RATE(_ERR)`	raw count rate (error) in the source aperture, $C_{\mathrm{r}(,\mathrm{err})}$
`COI_TOT_RATE(_ERR)`	corrected count rate (error) in the source aperture, $C_{\mathrm{test}(,\mathrm{err})}$
`COI_STD_FACTOR`	coincidence loss correction factor in the source aperture, f_{test}
`COI_BKG_RATE(_ERR)`	corrected count rate (error) per arcsec^2 in the background aperture, $C_{\mathrm{bkg}(,\mathrm{err})}$.

The values of $C_{\mathrm{test}(,\mathrm{err})}$ and f_{test} were measured from the five test regions. The measurements from individual regions in each of regions 0–4 were combined to obtain integrated measurements for regions 0–4, A_n, $C_{\mathrm{r},n}$ and $C_{\mathrm{r,err},n}$. Since the same background aperture `bkg.reg`, defined as an elliptical annulus, was used in all instances, $C_{\mathrm{bkg}(,\mathrm{err})}$ represents a single measurement. The total corrected and background-subtracted count rate C_{src} was then obtained by summing individually corrected stripes, or 'isophotes':

$$C_{\mathrm{src}} = \sum_{n=0}^{4} C_{\mathrm{src},n}, \tag{A.1}$$

where

$$C_{\mathrm{src},n} = C_{\mathrm{i},n} \times f_{\mathrm{test},n} - C_{\mathrm{bkg}} \times A_{\mathrm{i},n}, \tag{A.2}$$

$$C_{\mathrm{i},n} = \begin{cases} C_{\mathrm{r},n} - C_{\mathrm{r},n+1} & 0 \leq n \leq 3 \\ C_{\mathrm{r},4} & n = 4, \end{cases} \tag{A.3}$$

and

$$A_{\mathrm{i},n} = \begin{cases} A_n - A_{n+1} & 0 \leq n \leq 3 \\ A_4 & n = 4. \end{cases} \tag{A.4}$$

The upper limit to the statistical error in $C_{\mathrm{src},n}$ can be estimated by assuming that the fractional error in the count rate $C_{\mathrm{i},n}$ in each isophotal region is equal to the fractional error in the corrected count rates in the corresponding test region given by $C_{\mathrm{test,err},n}/C_{\mathrm{test},n}$. The errors associated with the corrected count rates for higher correction factors are significantly higher than the Poisson error, as shown by Kuin & Rosen (2008). Both $C_{\mathrm{test,err}}$ and $C_{\mathrm{bkg,err}}$ are binomial errors associated with the corrected count rates (Poole et al. 2008; Kuin & Rosen 2008).

A.3 Results

Detailed measurements in band *uvw2* are presented in Table A.1. These results show that even in region 1 the average count rate per pixel is 0.055 s^{-1}, which is significantly higher than the coincidence loss threshold of 0.028 s^{-1} (Hoversten et al. 2011).

n	$A_{\mathrm{i},n}$ [arcsec^2]	$f_{\mathrm{test},n}$	$C_{\mathrm{i},n}$ [s^{-1}]	$C_{\mathrm{src},n}$ [s^{-1}]
0	130000	1.003	525.6 ± 1.4	409 ± 21
1	8580	1.034	470.2 ± 1.1	479 ± 5
2	2870	1.086	396.8 ± 0.9	428 ± 3
3	747	1.134	181.5 ± 0.5	205 ± 1
4	426	1.494	206.8 ± 0.2	309 ± 1

Table A.1. Detailed photometric measurements for the five isophotal regions in NGC 4449 in band *uvw2* shown in Fig. A.3. $C_{\mathrm{bkg}} = 9.08 \pm 0.03 \times 10^{-4}$ s^{-1} arcsec^{-2}. See Section A.2 for column definitions.

Band	This work			'as-is'
	f_{max}	C_{src} [s^{-1}]	F_{src} [mJy]	F_{src} [mJy]
uvw2/1991Å	1.49	1830 ± 120	175 ± 12	172 ± 12
uvm2/2221Å	1.32	1140 ± 80	189 ± 14	202 ± 14
uvw1/2486Å	1.43	1870 ± 120	202 ± 15	207 ± 14
u/3442Å	1.51	3480 ± 300	249 ± 22	468 ± 40
b/4321Å	1.40	4670 ± 400	463 ± 41	1200 ± 100
v/5410Å	1.18	2270 ± 210	611 ± 57	1250 ± 100

Table A.2. Final count rates C_{src} and fluxes F_{src} in six UVOT bands for NGC 4449. f_{max} gives the maximum correction factor used for each band. For comparison, given on the right are the fluxes in the 'as-is' approach. All fluxes have been corrected for foreground extinction.

The total count rates in all six UVOT bands are given in Table A.2. The corresponding fluxes were obtained using the calibrations of Breeveld (2010), and were subsequently corrected for foreground extinction using $E(B-V) = 0.019$ (Schlegel et al. 1998) and the extinction law of Cardelli et al. (1989) with $R_V = 3.1$.

The uncertainties in the count rates listed in Table A.2 combine *(i)* the binomial errors in each of the test regions 0–4 (Kuin & Rosen 2008) scaled to the area of the corresponding region, *(ii)* the estimated uncertainties due to high background (Breeveld et al. 2010) and *(iii)* the uncertainty resulting from the choice of thresholds for the five regions. For the UV and optical bands, the uncertainties in *(ii)* were estimated at 6 and 8 per cent, respectively. The uncertainties in *(iii)* were found to be at most 2 per cent in all bands. Thus, the statistical and systematic uncertainties in the final fluxes (Table A.2) amount to ~ 7 and ~ 9 per cent overall for the UV and the optical bands.

Table A.2 also gives total fluxes calculated by UVOTSOURCE directly from region 0 in the 'as-is' approach, i.e., ignoring the spatial variations in the correction factors across UVOT images. In bands *uvw2*, *uvm2* and *uvw1* the fluxes agree to within 7 per cent, whereas in the optical bands the discrepancy is more significant. The agreement in the UV bands may suggest that the centre of region 0 probed the global average of the count rate distribution for the UV bands, weighted by the extent of coincidence loss. However, in sources that are

generally fainter in the UV, better agreement in these bands may be expected as the required correction factors are smaller. Although the values of $f_{\max}$ listed in Table A.2 show that the maximum correction factors were high in all bands, the emission in the UV is sharply peaked compared to the more uniform emission in the optical. This suggests that applying corrections to the UV bands is likely to be affected by a smaller systematic uncertainty than applying similar corrections to the optical bands. In general, these results confirm that UVOTSOURCE is not applicable 'as-is' to photometric measurements of extended sources, as expected from Section A.2.

The UV and optical fluxes in Table 2.2 are consistent with those obtained from *GALEX* and SDSS. A plot of the global SED of NGC 4449 in the range 1000–7000 Å is presented in Fig. A.4.

In the UV, the fluxes derived from *GALEX* and *Swift*/UVOT agree very well, but the absolute NUV flux is slightly lower than the corresponding fluxes obtained from *Swift*/UVOT. It should be noted that *GALEX*, in a similar way to *Swift*/UVOT, also suffers from local non-linearities near bright sources. These are more difficult to quantify and are not automatically corrected for (Morrissey et al. 2007). The count rates measured for NGC 4449 in a 3′ diameter aperture (~ 1000 s^{-1} in FUV and ~ 4000 s^{-1} in NUV) suggest that this effect is likely to lower the measured count rates and add a significant systematic uncertainty to the derived *GALEX* fluxes. Therefore, the true *GALEX* FUV and NUV fluxes may be higher and may be associated with larger uncertainties than those shown in Fig. A.4.

A.4 Conclusions

In the method presented above we used the existing understanding of coincidence loss for point-source observations and applied it to obtain photometric measurements for an extended source, NGC 4449, in three UV and three optical *Swift*/UVOT bands. The derived fluxes are in good agreement with the available global *GALEX* and SDSS photometry, with the overall uncertainties estimated at 7 and 9 per cent for the UV and the optical bands.

Extended-source observations with the three narrow UV bands and the small PSFs of *Swift*/UVOT enable more detailed studies of the youngest stellar component in galaxies. Although the uncertainties in our method are comparable with those of *GALEX*, we note that at higher count rates *GALEX* also suffers from non-linearity, which is not corrected for or included in the published uncertainties.

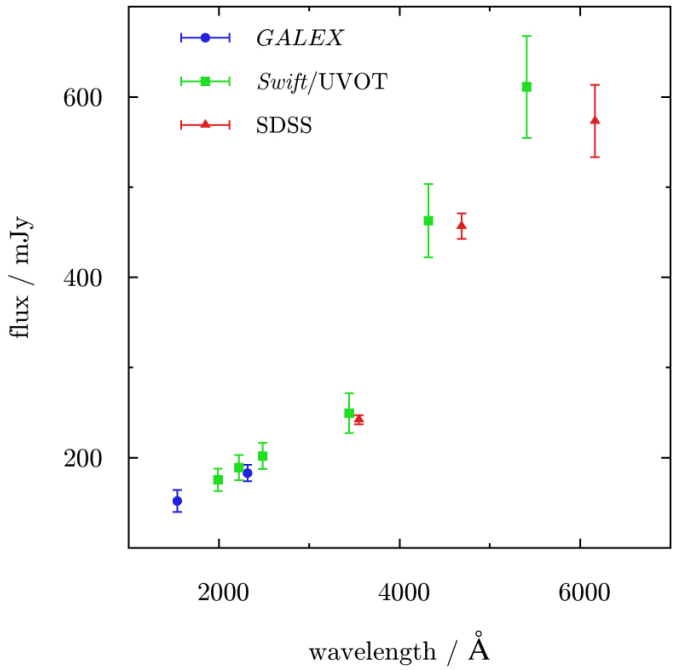

Figure A.4. Global photometry of NGC 4449 with *GALEX*, *Swift*/UVOT and SDSS using data from Table 2.2.

B Comments on individual supernovae

Comments and details on individual *Spitzer*/IRAC observations and relevant measurements are listed below. Aperture photometry was performed with a 3.″6 or a 2.″4 aperture, which correspond to source/background setups with annuli 3/3–7 or 2/2–6, as described in the IRAC Instrument Handbook (Laine 2013). Where not given explicitly, the aperture used for the measurements was 3.″6. All measurements were made using Starlink GAIA (v4.4.0).

Additionally, Figure B.1 shows images of individual supernovae at the earliest epoch observed by *Spitzer*/IRAC.

2000 ds

A source was not visible. The detection location has an elevated but uniform background and is near the bright centre of NGC 2768 (angular separation of 33″, corresponding to a projected distance of 3.3 kpc). The *Spitzer*/IRAC background levels were 1.3, 0.8, 0.5 and 1.5 $\mathrm{mJy\,kpc^{-2}}$ in channels 1, 2, 3 and 4. Upper limits to the supernova flux were derived from a nearby faint detected source.

2001 ci

A source was not visible. The detection location is in the disc of NGC 3079 close to the bright galaxy centre (26″; 2.1 kpc). The FOV of channels 1 and 3 in AOR 22000896 does not cover the supernova location. The background levels were (20, 14, 45, 120), (. . . , 14, . . . , 120) $\mathrm{mJy\,kpc^{-2}}$ for AOR 4331264 and AOR 22000896. Upper limits to the supernova flux were derived from a nearby faint detected source, except for channel 2 in AOR 25631744, for which noise statistics were used (see Section 4.3). Due to low S/N in AOR 25631744, reliable background measurements were not possible and this observation was excluded from further analysis.

2002 ap

The supernova location is in a remote part of M 74 (4.′7, 12.7 kpc; relative to galaxy centre). There was faint emission in channels 1 and 2; for channel 2 measurements from a 3.″6 and a 6″ aperture were averaged. Upper limits to the supernova flux in channels 3 and 4 were derived by averaging measurements on a nearby faint detected source using a 3.″6 and a 6″ aperture. Background measurements in channels 3 and 4 were not possible due to negative absolute background levels resulting from additional pipeline processing of SINGS observations (Kennicutt et al. 2003).

2002 ji

A source was not visible. The supernova location has a high and varying background and is close to the centre of NGC 3655 (24″; 3.1 kpc). The background levels were 0.8, 0.6, 1.7 and 7.9 $\mathrm{mJy\,kpc^{-2}}$. In channels 1, 2 and 4, upper limits to the supernova flux were derived from a nearby faint detected source. The aperture size for all measurements was 2.″4, except for channel 3, where the upper limit was derived by averaging measurements on a nearby faint detected source using a 2.″4 and a 3.″6 aperture.

2003 H

A source was not visible. The supernova location has a high and varying background and is located at the interface between NGC 2207 and IC 2163 (51″, 8.6 kpc; relative to NGC 2207). The background levels were 0.9, 0.6, 2.3 and 5.3 mJy kpc^{-2}. Upper limits to the supernova flux were derived from a nearby faint detected source. The aperture size for all measurements was 2.″4.

2003 id

Faint emission from the supernova was visible, except in AOR 11775488 channel 3. The supernova location has a varying background and is in the outer part of NGC 895 (37″, 6.3 kpc; relative to galaxy centre). Due to bright unresolved sources nearby, standard aperture photometry was not possible. Measurements were obtained manually using 2.″4 apertures. The final flux in AOR 11775488 channel 2 and AOR 10553344 channel 1 were computed by subtracting an averaged sampled background, which was measured using the same aperture. In AOR 11775488 channel 3 the upper limit was estimated using noise statistics. In the remaining observations the measurements were less than 3σ and therefore 3σ upper limits are quoted.

Difference images were constructed by subtracting AOR 10553344 (day 489) from AOR 11775488 (day 314). Faint emission was visible only in channel 2, for which averaged measurements for a 2.″4 and a 3.″6 aperture yielded a source flux of $19 \pm 2\,\mu$Jy, which is consistent with the day 314 and day 489 measurements from direct images.

2003 jg

A source, visible at the position of the supernova, was blended with the bulge of the host galaxy. The supernova location site has a very high background and is near the centre of NGC 2997 (15″; 0.9 kpc). Background levels are 21, 14, 31 and 93 mJy kpc^{-2}. Upper limits to the supernova flux were derived using noise statistics.

2004 C

A source was visible at the position of the supernova in channels 1 and 2, observations in channels 3 and 4 are not usable due to saturation artifacts. The supernova location has a very high background and is near the centre of NGC 3683 (11″; 1.9 kpc). Due to the bright galaxy centre nearby, standard aperture photometry was not possible. Measurements of source and sky were obtained manually using a 2.″4 aperture. Final fluxes were computed by subtracting an averaged sampled background measured using the same aperture.

2004 bm

Faint detections were visible in channels 3 and 4. The supernova location has a high and varying background and is near the centre of NGC 3437 (8″; 1 kpc). Due to the bright galaxy centre nearby, standard aperture photometry was not possible. Measurements were obtained manually using 2.″4 apertures. Final fluxes were computed by subtracting an averaged sampled background, which was measured using the same aperture. In AOR 11997184 a channel 4 measurement was not possible due to saturation artifacts. In AOR 14458624 channel 4 a rectangular $6'' \times 3''$ aperture was used to avoid contamination by saturation artifacts. Background levels in IRAC channels 1 and 2 were (11, 6.8), (11, 7.2) and (11, 7.4) mJy kpc^{-2} for AOR 11997440, AOR 11997184 and AOR

14458624. Upper limits to the supernova flux were derived using noise statistics. The aperture size for all measurements was 2.″4.

Difference images constructed by subtracting AOR 14458624 (day 767) from AOR 11997440 (day 236) and AOR 14458624 (day 767) from AOR 11997184 (day 377) show no detections.

2004 cc

A source was not visible at the supernova location, which has a high and varying background and is near the centre of NGC 4568 (13″; 1 kpc). The supernova location is outside the FOV of channels 2 and 4 of AOR 10530560 and channels 1 and 3 of AOR 10530816. The background levels were 21, 14, 33 and 97 mJy kpc^{-2}. Upper limits to the supernova flux were derived using 2.″4 apertures on a nearby faint detected source.

2005 E

A source was not visible at the supernova location, which is in a remote part of NGC 1032 (2.′3, 22.7 kpc; relative to galaxy centre). The background levels were (0, 0.03, 0, 1.1) and (0.01, 0.04, 0, 1.2) mJy kpc^{-2} for AOR 14457344 and AOR 14457600. Upper limits to the supernova flux were derived from a nearby faint detected source.

Difference images constructed by subtracting AOR 14457600 (day 388) from AOR 14457344 (day 222) show no detections. Faint emission in channel 3 was not considered a detection due to a low S/N.

2005 V

A source was not visible at the supernova location, which has a high and varying background and is near the centre of NGC 2146 (6″; 0.4 kpc) The FOV of channels 1 and 3 did not cover the location of the supernova, while the observation in channel 4 was not usable due to saturation artifacts. The background level in channel 2 was 310 mJy kpc^{-2}. An upper limit to the supernova flux was derived using noise statistics.

In the pre-explosion observation of NGC 2146 (AOR 4328192) the FOV of channels 1 and 3 does not cover the detection site. Difference images were constructed for channels 2 and 4 by subtracting AOR 4328192 (day −328) from AOR 22000384 (day 989). However, measurements could not be made due to saturation artifacts near the centre of this galaxy.

2005 at

A source was visible at the location of the supernova, which is in the disc of NGC 6744 (2.′2, 4.5 kpc; relative to galaxy centre) and has a high and varying background. Due to multiple unresolved sources nearby, standard aperture photometry was not possible. Measurements of source and sky were obtained manually using 2.″4 apertures. Final source fluxes were computed by subtracting an averaged sampled background measured using the same aperture.

2005 cz

A source was not visible at the location of the supernova, which has elevated and varying background and is near the bright bulge of NGC 4589 (8″; 0.8 kpc). The observation in channel 1 was not usable due to saturation artifacts. The background levels were 4.4, 2.8, and 2.0 mJy kpc^{-2} for channels 2, 3 and 4. Upper limits to the supernova flux were derived using noise statistics. The aperture size used for all measurements was 2.″4.

2005 kl

A source was visible at the location of the supernova but was blended with nearby unresolved features. The supernova location has a high and varying background and is near the bright centre of NGC 4369 (10″; 1 kpc). Due to unresolved features nearby, standard aperture photometry was not possible. The background levels were 13, 9.5, 32 and 80 mJy kpc^{-2}. Upper limits to the supernova flux were derived using noise statistics. The aperture size used for all measurements was 2.″4.

2006 jc

A bright detection of the supernova was visible close to the centre of UGC 4904 (14″; 1.7 kpc). Measurements were obtained using standard aperture photometry with a 2.″4 aperture on direct images.

In the pre-explosion image of UGC 4904 (AOR 5532416) the FOV of channels 2 and 4 did not cover the detection site and therefore measurements on difference images could not be used consistently for all bands. Nevertheless, difference images were constructed by subtracting AOR 5532416 (day −892) from AOR 21268224 (day 210), AOR 5532416 (day −892) from AOR 23113472 (day 412) and AOR 5532416 (day −892) from AOR 23113728 (day 582). Supernova flux measurements for channels 1 and 3 obtained using standard aperture photometry were (515 ± 2, 776 ± 7), (50 ± 2, 222 ± 8) and (9.7 ± 0.8, 70 ± 3) μJy for the epochs corresponding to AOR 21268224, AOR 23113472 and AOR 23113728. The uncertainties quoted above result primarily from background subtraction; the uncertainty due to the photometric calibration was not included.

2007 gr

A bright detection of the supernova was visible in all channels. The supernova location has a high and varying background and is in the disc of NGC 1058 (29″, 1.3 kpc; relative to galaxy centre). Measurements were obtained from aperture photometry on difference images constructed by subtracting the pre-explosion observation AOR 4433408 (day −1109) from AOR 24200704 (day 17).

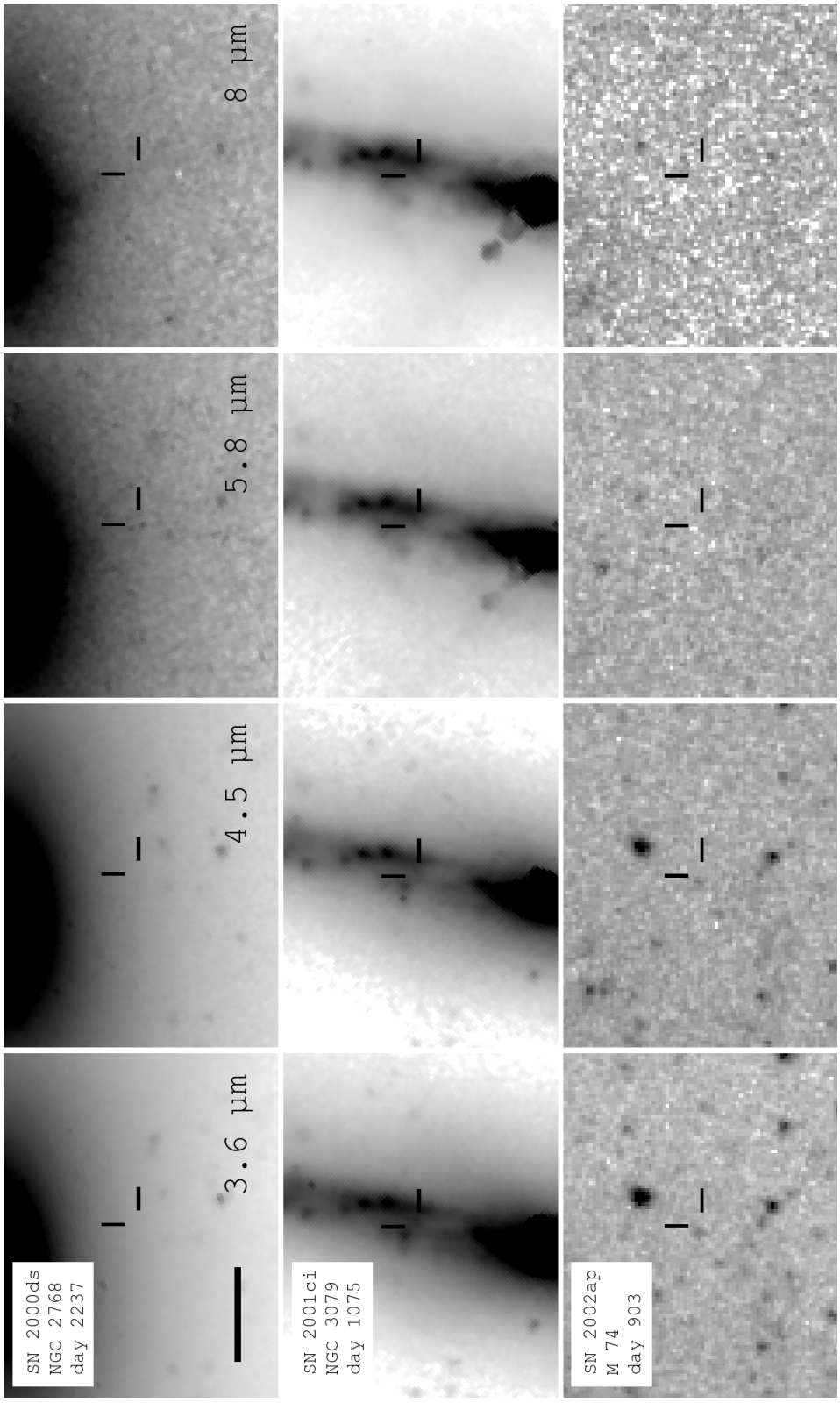

Figure B.1. Images of 17 supernovae in the sample at the earliest epoch observed by *Spitzer*/IRAC. North is up, east is to the left. The bar in the top left image is 20″ in length. *(continued on next page)*

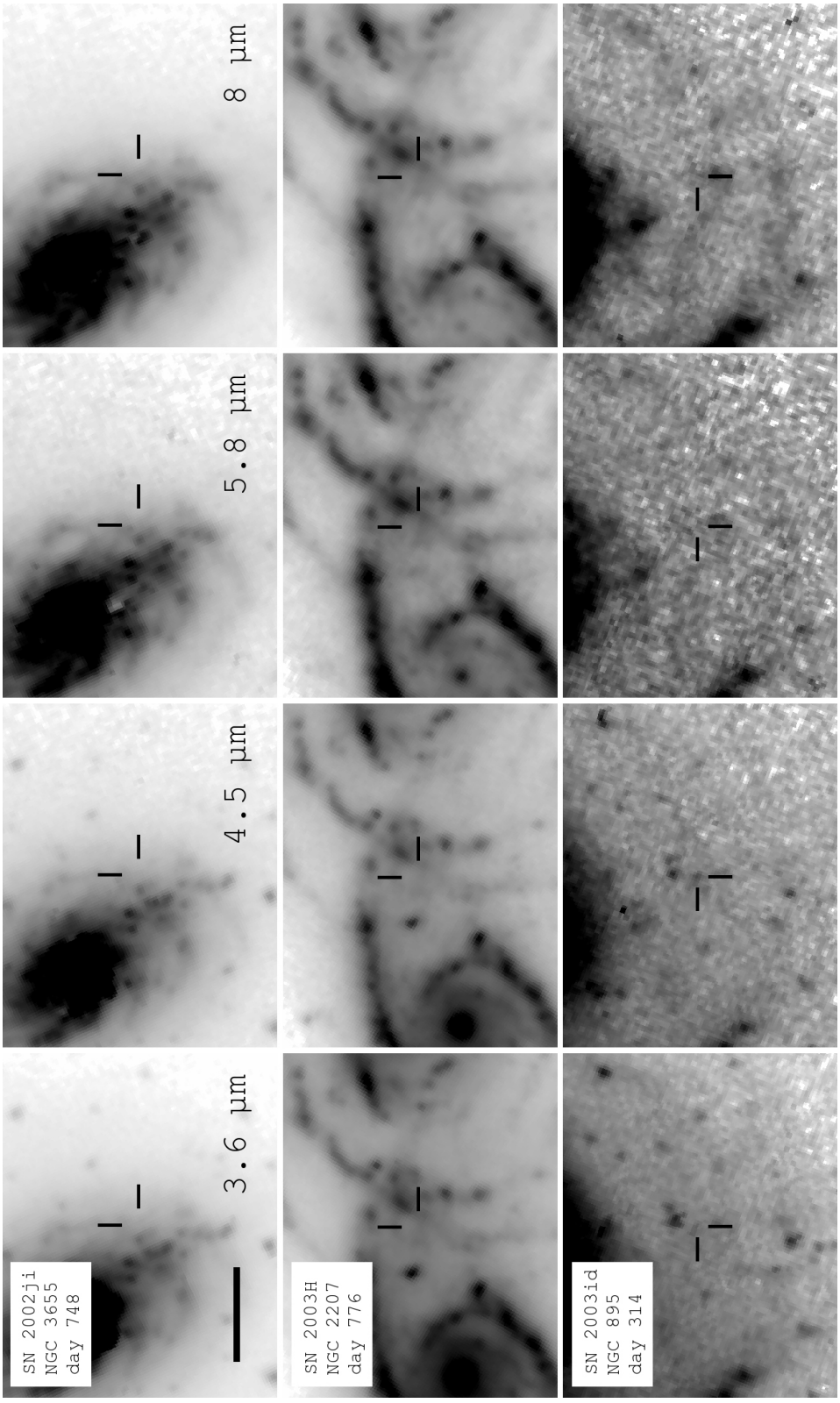

Figure B.1. *(continued from previous page)*

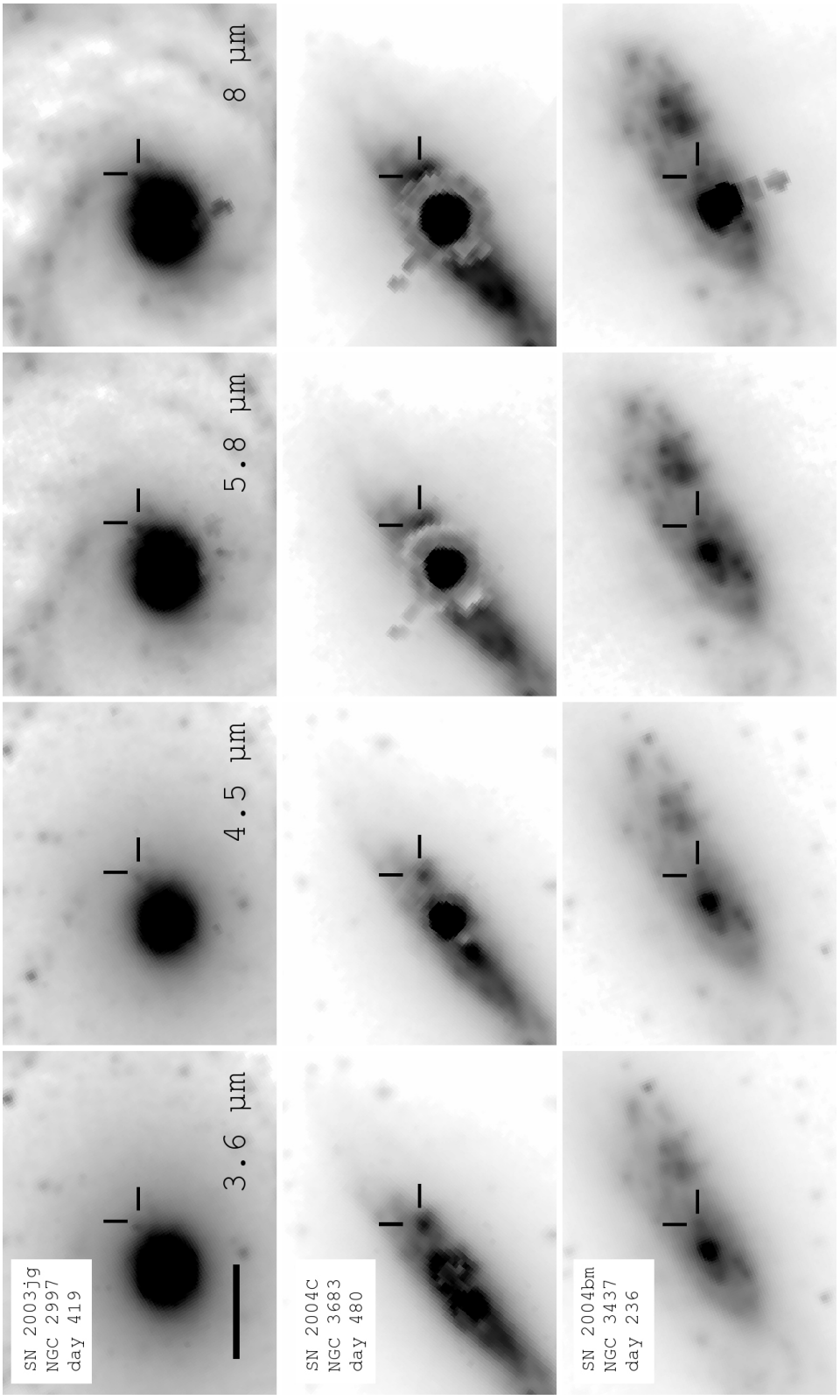

Figure B.1. *(continued from previous page)*

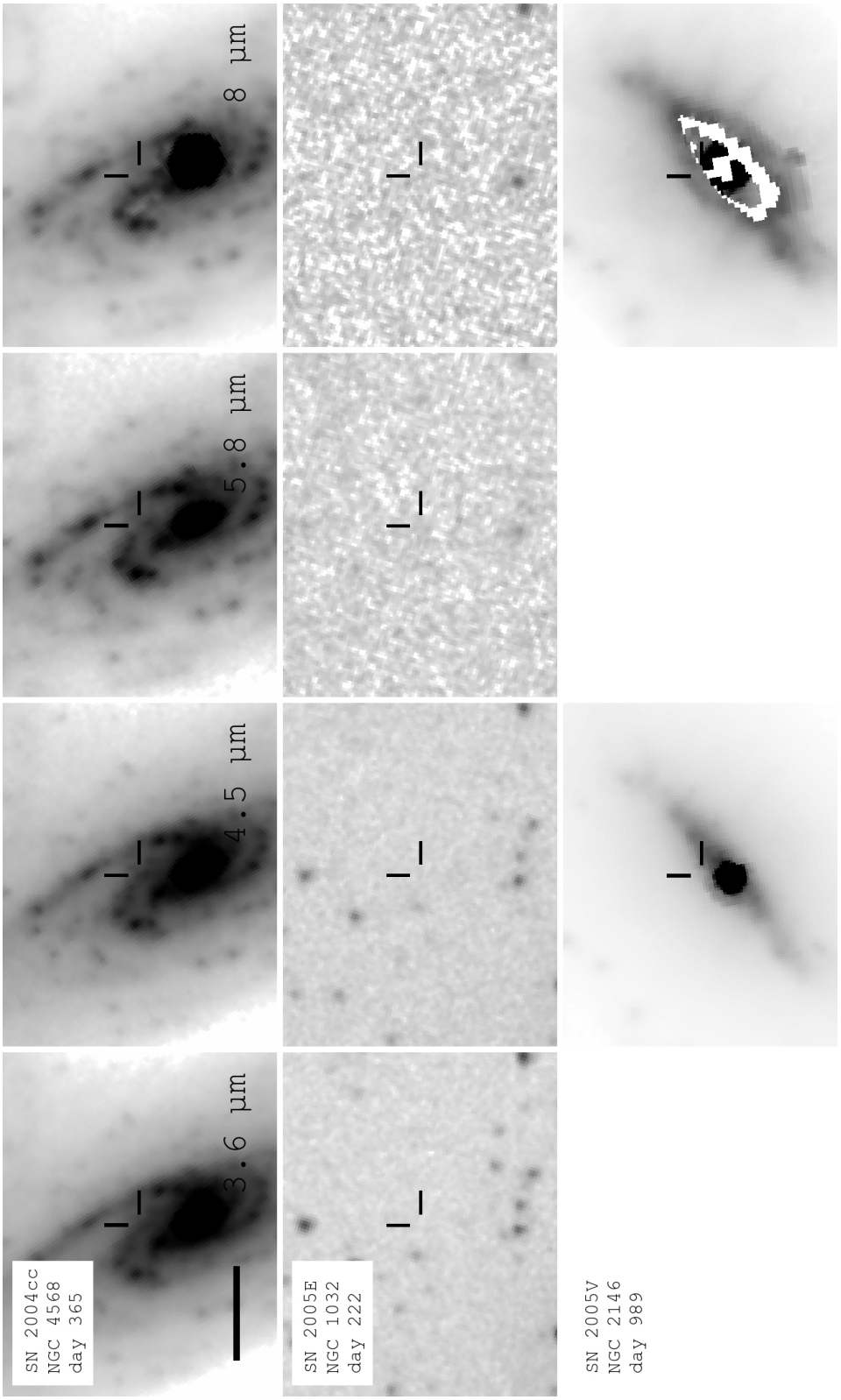

Figure B.1. *(continued from previous page)*

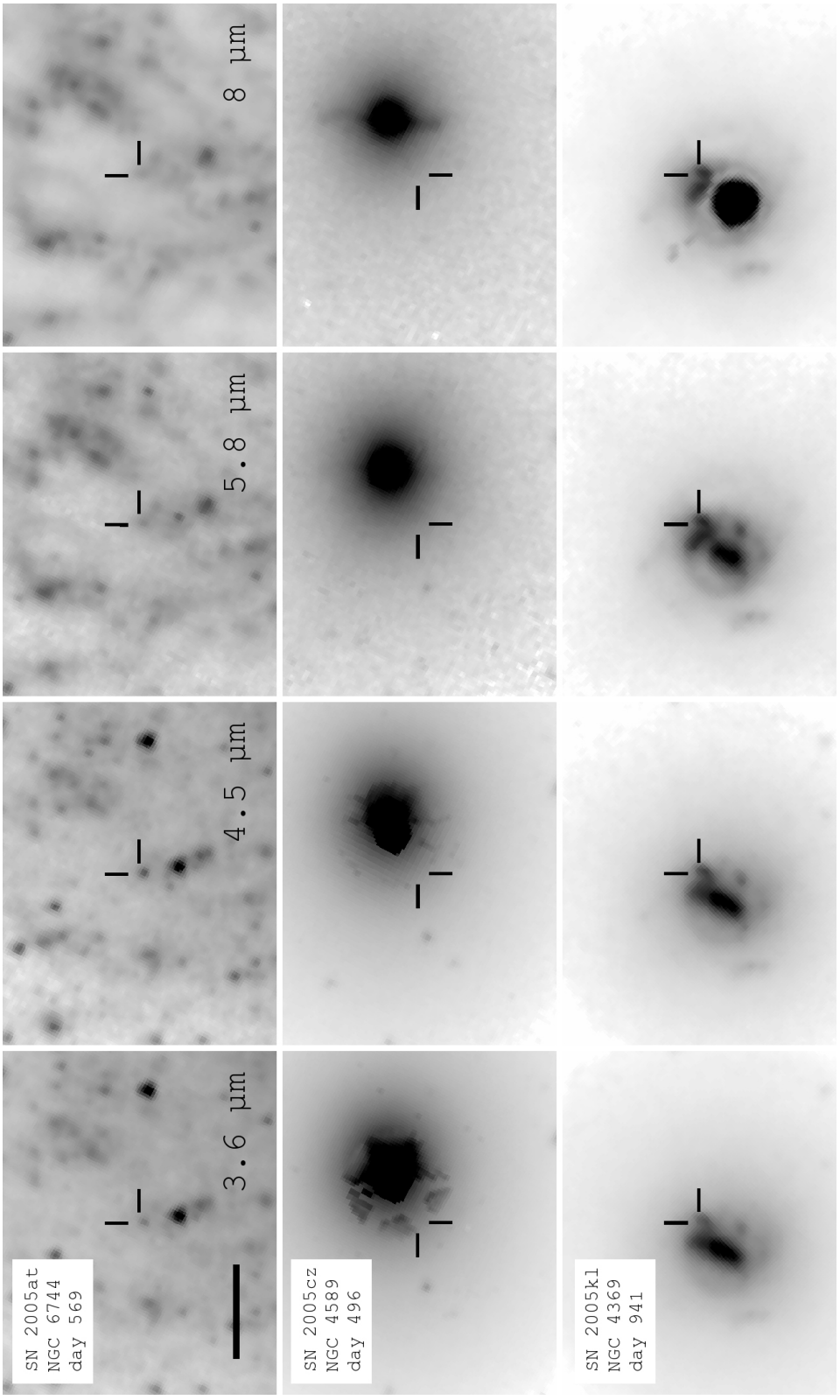

Figure B.1. *(continued from previous page)*

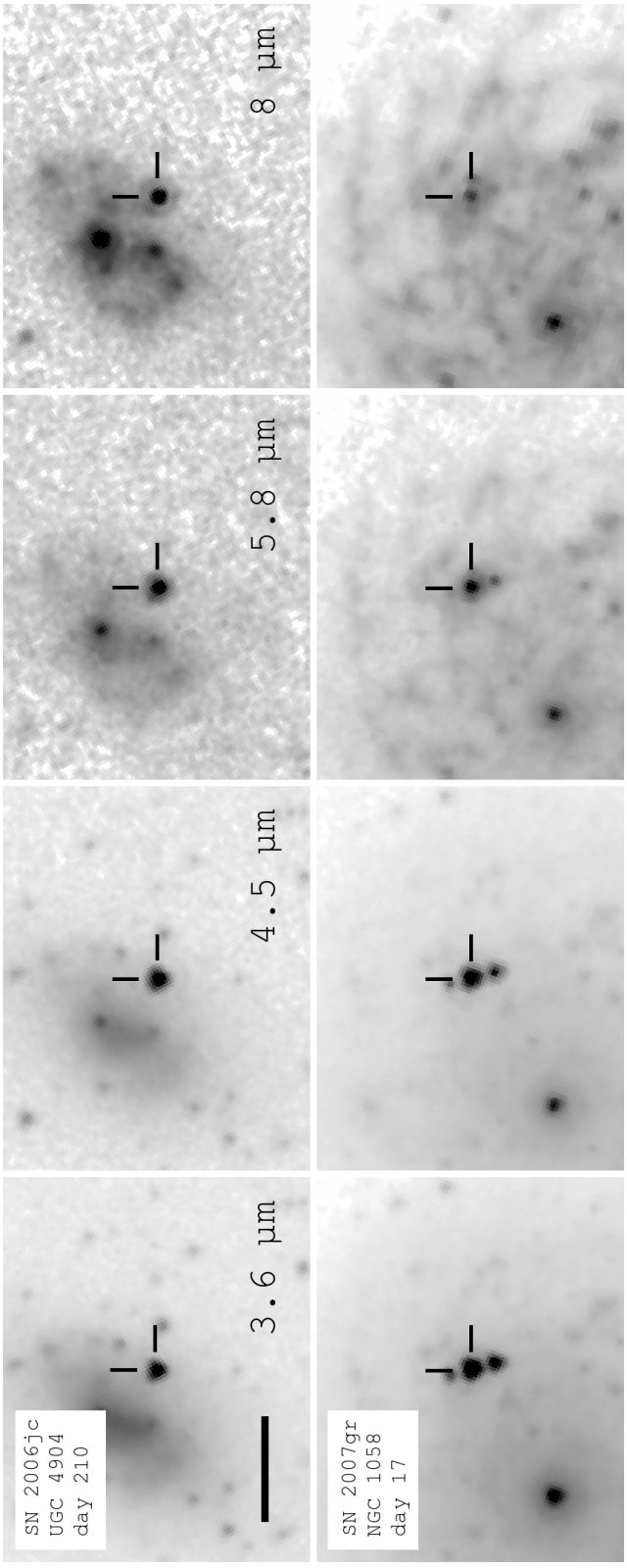

Figure B.1. *(continued from previous page)*

Bibliography

Abel N. P., Ferland G. J., Shaw G., van Hoof P. A. M., 2005, ApJS, 161, 65
Allamandola L. J., Tielens A. G. G. M., Barker J. R., 1985, ApJL, 290, L25
Alloin D., Collin-Souffrin S., Joly M., Vigroux L., 1979, A&A, 78, 200
Amorín R., Pérez-Montero E., Vílchez J. M., Papaderos P., 2012, ApJ, 749, 185
Anderson J. P., James P. A., 2008, MNRAS, 390, 1527
Anderson J. P., James P. A., 2009, MNRAS, 399, 559
Annibali F., Aloisi A., Mack J., Tosi M., van der Marel R. P., Angeretti L., Leitherer C., Sirianni M., 2008, AJ, 135, 1900
Anupama G. C., Sahu D. K., Gurugubelli U. K., Prabhu T. P., Tominaga N., Tanaka M., Nomoto K., 2009, MNRAS, 392, 894
Asari N. V., Cid Fernandes R., Stasińska G., Torres-Papaqui J. P., Mateus A., Sodré L., Schoenell W., Gomes J. M., 2007, MNRAS, 381, 263
Baes M., Dejonghe H., 2000, MNRAS, 313, 153
Baes M. et al., 2010, A&A, 518, L39
Bajaja E., Huchtmeier W. K., Klein U., 1994, A&A, 285, 385
Bakes E. L. O., Tielens A. G. G. M., 1994, ApJ, 427, 822
Barbon R., Buondí V., Cappellaro E., Turatto M., 1999, A&AS, 139, 531
Barbon R., Cappellaro E., Ciatti F., Turatto M., Kowal C. T., 1984, A&AS, 58, 735
Barbon R., Cappellaro E., Turatto M., 1989, A&AS, 81, 421
Barlow M. J., 1987, MNRAS, 227, 161
Barlow M. J., 2009, Prospects for Studies of Stellar Evolution and Stellar Death in the JWST Era. p. 247
Barlow M. J. et al., 2010, A&A, 518, L138
Bastien P., Arcoragi J.-P., Benz W., Bonnell I., Martel H., 1991, ApJ, 378, 255
Bauschlicher Jr. C. W., Peeters E., Allamandola L. J., 2008, ApJ, 678, 316
Bauschlicher Jr. C. W., Peeters E., Allamandola L. J., 2009, ApJ, 697, 311
Begelman M. C., 1985, ApJ, 297, 492
Bendo G. J. et al., 2010, A&A, 518, L65
Bendo G. J. et al., 2012a, MNRAS, 419, 1833
Bendo G. J., Galliano F., Madden S. C., 2012b, MNRAS, 423, 197
Bethe H. A., 1939, Physical Review, 55, 434
Bianchi S., 2008, A&A, 490, 461
Bianchi S., Schneider R., 2007, MNRAS, 378, 973
Bisbas T. G., Bell T. A., Viti S., Yates J., Barlow M. J., 2012, MNRAS, 427, 2100
Blanc G. A., Heiderman A., Gebhardt K., Evans II N. J., Adams J., 2009, ApJ, 704, 842
Boersma C., Bauschlicher C. W., Allamandola L. J., Ricca A., Peeters E., Tielens A. G. G. M., 2010, A&A, 511, A32
Boquien M. et al., 2011, AJ, 142, 111
Boselli A. et al., 2012, A&A, 540, A54
Bothun G. D., 1986, AJ, 91, 507
Böttner C., Klein U., Heithausen A., 2003, A&A, 408, 493
Bouchet P., Danziger I. J., 1993, A&A, 273, 451
Bouchet P., Slezak E., Le Bertre T., Moneti A., Manfroid J., 1989, A&AS, 80, 379
Boulanger F., Boisssel P., Cesarsky D., Ryter C., 1998, A&A, 339, 194
Bowen I. S., 1928, ApJ, 67, 1
Bowen I. S., 1936, Reviews of Modern Physics, 8, 55
Brauher J. R., Dale D. A., Helou G., 2008, ApJS, 178, 280
Breeveld A. A., 2010, SWIFT UVOT CALDB RELEASE NOTE: AB Magnitude System (SWIFT-UVOT-CALDB-16-R01)
Breeveld A. A. et al., 2010, MNRAS, 406, 1687

Bromm V., Coppi P. S., Larson R. B., 1999, ApJL, 527, L5
Brownlee D. et al., 2006, Science, 314, 1711
Bruzual G., Charlot S., 2003, MNRAS, 344, 1000
Bryan G. L., Volk K., Kwok S., 1990, ApJ, 365, 301
Burbidge G. R., Gould R. J., Pottasch S. R., 1963, ApJ, 138, 945
Burkert A., Alves J., 2009, ApJ, 695, 1308
Cardelli J. A., Clayton G. C., Mathis J. S., 1989, ApJ, 345, 245
Chabrier G., 2003, PASP, 115, 763
Chokshi A., Tielens A. G. G. M., Werner M. W., Castelaz M. W., 1988, ApJ, 334, 803
Chugai N. N., 2009, MNRAS, 400, 866
Cid Fernandes R., Mateus A., Sodré L., Stasińska G., Gomes J. M., 2005, MNRAS, 358, 363
Cohen M., Wheaton W. A., Megeath S. T., 2003, AJ, 126, 1090
Cooksy A. L., Blake G. A., Saykally R. J., 1986, ApJL, 305, L89
Cormier D. et al., 2012, A&A, 548, A20
Corwin Jr. H. G., Buta R. J., de Vaucouleurs G., 1994, AJ, 108, 2128
Croxall K. V. et al., 2012, ApJ, 747, 81
Czyzak S. J., Keyes C. D., Aller L. H., 1986, ApJS, 61, 159
De Looze I. et al., 2012, MNRAS, 427, 2797
de Vaucouleurs G., de Vaucouleurs A., Corwin Jr. H. G., Buta R. J., Paturel G., Fouque P., 1991, Third Reference Catalogue of Bright Galaxies
Désert F.-X. et al., 2008, A&A, 481, 411
Dessart L., Hillier D. J., Livne E., Yoon S.-C., Woosley S., Waldman R., Langer N., 2011, MNRAS, 414, 2985
Di Carlo E. et al., 2008, ApJ, 684, 471
Dopita M. A. et al., 2006, ApJ, 647, 244
Draine B. T., 1978, ApJS, 36, 595
Draine B. T., 1985, ApJS, 57, 587
Draine B. T., 2009, in T. Henning, E. Grün & J. Steinacker ed., Cosmic Dust – Near and Far Vol. 414 of Astronomical Society of the Pacific Conference Series, Interstellar Dust Models and Evolutionary Implications. p. 453
Draine B. T., Lee H. M., 1984, ApJ, 285, 89
Draine B. T., Li A., 2001, ApJ, 551, 807
Draine B. T., Li A., 2007, ApJ, 657, 810
Dwek E., 1998, ApJ, 501, 643
Dwek E., Cherchneff I., 2011, ApJ, 727, 63
Dwek E. et al., 2011a, ApJ, 738, 36
Dwek E. et al., 2011b, ApJ, 738, 36
Elmegreen B. G., 2002, ApJ, 577, 206
Elmegreen D. M., Kaufman M., Elmegreen B. G., Brinks E., Struck C., Klarić M., Thomasson M., 2001, AJ, 121, 182
Engelbracht C. W., Rieke G. H., Gordon K. D., Smith J.-D. T., Werner M. W., Moustakas J., Willmer C. N. A., Vanzi L., 2008, ApJ, 678, 804
Ercolano B., Barlow M. J., Storey P. J., 2005, MNRAS, 362, 1038
Ercolano B., Barlow M. J., Storey P. J., Liu X.-W., 2003, MNRAS, 340, 1136
Ercolano B., Barlow M. J., Sugerman B. E. K., 2007, MNRAS, 375, 753
Ercolano B., Wesson R., Bastian N., 2010, MNRAS, 401, 1375
Ercolano B., Young P. R., Drake J. J., Raymond J. C., 2008, ApJS, 175, 534
Fabbri J. et al., 2011, MNRAS, 418, 1285
Fabbri J. N., 2011, PhD thesis, University College London
Fazio G. G. et al., 2004, ApJS, 154, 10
Ferreras I., Charlot S., Silk J., 1999, ApJ, 521, 81
Ferreras I., Cropper M., Kawata D., Page M., Hoversten E. A., 2012, MNRAS, 424, 1636
Ferreras I., Silk J., 2003, MNRAS, 344, 455
Filippenko A. V., Porter A. C., Sargent W. L. W., 1990, AJ, 100, 1575
Fitzpatrick E. L., Massa D., 1986, ApJ, 307, 286
Foley R. J., Smith N., Ganeshalingam M., Li W., Chornock R., Filippenko A. V., 2007, ApJL, 657, L105

Ford G. P. et al., 2013, ApJ, 769, 55
Fox O. et al., 2009, ApJ, 691, 650
Fuentes-Masip O., Castañeda H. O., Muñoz-Tuñón C., 2000, AJ, 119, 2166
Galametz M. et al., 2010, A&A, 518, L55
Galametz M. et al., 2013, MNRAS, 431, 1596
Galametz M., Madden S. C., Galliano F., Hony S., Bendo G. J., Sauvage M., 2011, A&A, 532, A56
Galliano F., Dwek E., Chanial P., 2008a, ApJ, 672, 214
Galliano F., Madden S. C., Jones A. P., Wilson C. D., Bernard J.-P., Le Peintre F., 2003, A&A, 407, 159
Galliano F., Madden S. C., Tielens A. G. G. M., Peeters E., Jones A. P., 2008b, ApJ, 679, 310
Gehrels N. et al., 2004, ApJ, 611, 1005
Georgy C., Meynet G., Walder R., Folini D., Maeder A., 2009, A&A, 502, 611
Giard M., Bernard J. P., Lacombe F., Normand P., Rouan D., 1994, A&A, 291, 239
Goldsmith P. F., Langer W. D., 1978, ApJ, 222, 881
Goldsmith P. F., Langer W. D., Pineda J. L., Velusamy T., 2012, ApJS, 203, 13
Gomez H. L. et al., 2012a, MNRAS, 420, 3557
Gomez H. L. et al., 2012b, ApJ, 760, 96
González J. J., 1993, PhD thesis, University of California, Santa Cruz
González Delgado R. M., Heckman T., Leitherer C., Meurer G., Krolik J., Wilson A. S., Kinney A., Koratkar A., 1998, ApJ, 505, 174
Gordon K. D. et al., 2004, ApJS, 154, 215
Greve A., Neininger N., Sievers A., Tarchi A., 2006, A&A, 459, 441
Griffin M. J. et al., 2010, A&A, 518, L3
Griffin M. J., Lim T. L., 2011 Vol. 52 of EAS Publications Series, Herschel-SPIRE: an update on performance and plans. pp 9–14
Groves B., Dopita M. A., Sutherland R. S., Kewley L. J., Fischera J., Leitherer C., Brandl B., van Breugel W., 2008a, ApJS, 176, 438
Groves B., Nefs B., Brandl B., 2008b, MNRAS, 391, L113
Guseva N. G., Papaderos P., Izotov Y. I., Noeske K. G., Fricke K. J., 2004, A&A, 421, 519
Habart E., Verstraete L., Boulanger F., Pineau des Forêts G., Le Peintre F., Bernard J. P., 2001, A&A, 373, 702
Habing H. J., 1968, Bull. Astron. Inst. Neth., 19, 421
Hanner M., 1988, in M. S. Hanner ed., Infrared Observations of Comets Halley and Wilson and Properties of the Grains Vol. 3004 of NASA Conference Publication, Grain optical properties. pp 22–49
Hartmann L., Ballesteros-Paredes J., Bergin E. A., 2001, ApJ, 562, 852
Hayashi C., Cameron R. C., 1962, ApJ, 136, 166
Heiles C., 1994, ApJ, 436, 720
Helou G. et al., 2004, ApJS, 154, 253
Hendry M. A. et al., 2005, MNRAS, 359, 906
Hermelo I., Lisenfeld U., Relaño M., Tuffs R. J., Popescu C. C., Groves B., 2013, A&A, 549, A70
Hess K. M., Pisano D. J., Wilcots E. M., Chengalur J. N., 2009, ApJ, 699, 76
Hidalgo-Gámez A. M., Ramírez-Fuentes D., 2009, AJ, 137, 169
Hildebrand R. H., 1983, Q. J. R. Astron. Soc., 24, 267
Hill R. S. et al., 1998, ApJ, 507, 179
Hillebrandt W., Niemeyer J. C., 2000, ArA&A, 38, 191
Ho L. C., Keto E., 2007, ApJ, 658, 314
Hogg D. E., Roberts M. S., Haynes M. P., Maddalena R. J., 2007, AJ, 134, 1046
Hony S., 2011, in Charbonnel C., Montmerle T., eds, EAS Publications Series Vol. 51 of EAS Publications Series, Tracing star formation in nearby galaxies. pp 97–105
Hony S., Van Kerckhoven C., Peeters E., Tielens A. G. G. M., Hudgins D. M., Allamandola L. J., 2001, A&A, 370, 1030
Houck J. R. et al., 2004, ApJS, 154, 18
Hoversten E. A. et al., 2011, AJ, 141, 205

Hoyle F., Wickramasinghe N. C., 1970, Nature, 226, 62
Hunter D., 1997, PASP, 109, 937
Hunter D. A., Gillett F. C., Gallagher III J. S., Rice W. L., Low F. J., 1986, ApJ, 303, 171
Hunter D. A., van Woerden H., Gallagher J. S., 1999, AJ, 118, 2184
Hunter D. A., Wilcots E. M., van Woerden H., Gallagher J. S., Kohle S., 1998, ApJL, 495, L47
Hunter D. J. et al., 2009, A&A, 508, 371
Immler S. et al., 2008, ApJL, 674, L85
Inno L. et al., 2013, ApJ, 764, 84
Itagaki K. et al., 2006, IAU Circ., 8762, 1
James B. L., 2009, PhD thesis, University College London
Jensen J. B., Tonry J. L., Barris B. J., Thompson R. I., Liu M. C., Rieke M. J., Ajhar E. A., Blakeslee J. P., 2003, ApJ, 583, 712
Kaler J. B., 1985, ArA&A, 23, 89
Kaufman M. J., Wolfire M. G., Hollenbach D. J., 2006, ApJ, 644, 283
Kaufman M. J., Wolfire M. G., Hollenbach D. J., Luhman M. L., 1999, ApJ, 527, 795
Kelly P. L., Kirshner R. P., Pahre M., 2008, ApJ, 687, 1201
Kemper F., Vriend W. J., Tielens A. G. G. M., 2004, ApJ, 609, 826
Kennicutt R. C. et al., 2011, PASP, 123, 1347
Kennicutt Jr. R. C., 1989, ApJ, 344, 685
Kennicutt Jr. R. C., 1992, ApJS, 79, 255
Kennicutt Jr. R. C., 1998, ArA&A, 36, 189
Kennicutt Jr. R. C. et al., 2003, PASP, 115, 928
Kennicutt Jr. R. C. et al., 2007, ApJ, 671, 333
Kennicutt Jr. R. C. et al., 2009, ApJ, 703, 1672
Kingsburgh R. L., Barlow M. J., 1992, MNRAS, 257, 317
Kingsburgh R. L., Barlow M. J., 1994, MNRAS, 271, 257
Kobulnicky H. A., Kennicutt Jr. R. C., Pizagno J. L., 1999, ApJ, 514, 544
Komugi S., Sofue Y., Kohno K., Nakanishi H., Onodera S., Egusa F., Muraoka K., 2008, ApJS, 178, 225
Kotak R. et al., 2009, ApJ, 704, 306
Kravtsov A. V., 2006, e-print (astro-ph/0607463)
Kreckel H., Bruhns H., Čížek M., Glover S. C. O., Miller K. A., Urbain X., Savin D. W., 2010, Science, 329, 69
Kroupa P., Aarseth S., Hurley J., 2001, MNRAS, 321, 699
Kroupa P., Gilmore G., Tout C. A., 1991, MNRAS, 251, 293
Krumholz M. R., McKee C. F., 2005, ApJ, 630, 250
Kuin N. P. M., Rosen S. R., 2008, MNRAS, 383, 383
Laine S., 2013, IRAC Instrument Handbook (version 2.0.3)
Laor A., Draine B. T., 1993, ApJ, 402, 441
Lebouteiller V. et al., 2012, A&A, 548, A91
Leitherer C. et al., 1999, ApJS, 123, 3
Leloudas G. et al., 2011, A&A, 530, A95
Leloudas G., Sollerman J., Levan A. J., Fynbo J. P. U., Malesani D., Maund J. R., 2010, A&A, 518, A29
Li A., 2003, ApJ, 584, 593
Li A., 2005, in Popescu C. C., Tuffs R. J., eds, The Spectral Energy Distributions of Gas-Rich Galaxies: Confronting Models with Data Vol. 761 of American Institute of Physics Conference Series, On the Absorption and Emission Properties of Interstellar Grains. pp 123–133
Li A., Draine B. T., 2001, ApJL, 550, L213
Liebert J., 1980, ArA&A, 18, 363
MacLachlan J. M., Matthews L. D., Wood K., Gallagher J. S., 2011, ApJ, 741, 6
Madden S. C. et al., 2013, PASP, submitted
Madden S. C., Galliano F., Jones A. P., Sauvage M., 2006, A&A, 446, 877
Mahoney W. A. et al., 2010, in Society of Photo-Optical Instrumentation Engineers (SPIE) Conference Series Vol. 7737 of Society of Photo-Optical Instrumentation Engineers (SPIE)

Conference Series, Spitzer warm mission transition and operations
Malhotra S. et al., 2001, ApJ, 561, 766
Marble A. R. et al., 2010, ApJ, 715, 506
Marengo M. et al., 2010, ApJ, 725, 2392
Markwardt C. B., 2009, in Bohlender D. A., Durand D., Dowler P., eds, Astronomical Data Analysis Software and Systems XVIII Vol. 411 of Astronomical Society of the Pacific Conference Series, Non-linear Least-squares Fitting in IDL with MPFIT. p. 251
Martin C. L., 1997, ApJ, 491, 561
Martin C. L., Kennicutt Jr. R. C., 1997, ApJ, 483, 698
Martin D. C. et al., 2005, ApJL, 619, L1
Martínez-Galarza J. R., Groves B., Brandl B., de Messieres G. E., Indebetouw R., Dopita M. A., 2011, ApJ, 738, 176
Matheson T., Filippenko A. V., Li W., Leonard D. C., Shields J. C., 2001, AJ, 121, 1648
Mathis J. S., Rumpl W., Nordsieck K. H., 1977, ApJ, 217, 425
Matsuura M. et al., 2009, MNRAS, 396, 918
Matsuura M. et al., 2011, Science, 333, 1258
Mattila S. et al., 2008, MNRAS, 389, 141
Maurer I., Mazzali P. A., 2010, MNRAS, 408, 947
Meikle W. P. S. et al., 2007, ApJ, 665, 608
Meikle W. P. S. et al., 2011, ApJ, 732, 109
Méndez-Abreu J., Aguerri J. A. L., Corsini E. M., Simonneau E., 2008, A&A, 478, 353
Mendoza C., 1983, in D. R. Flower ed., Planetary Nebulae Vol. 103 of Proceedings of the International Astronomical Union Symposia and Colloquia, Recent advances in atomic calculations and experiments of interest in the study of planetary nebulae. pp 143–172
Mendoza C., Zeippen C. J., 1982, MNRAS, 199, 1025
Michałowski M. J., Watson D., Hjorth J., 2010, ApJ, 712, 942
Miller J. S., Mathews W. G., 1972, ApJ, 172, 593
Miyake K., Nakagawa Y., 1993, Icarus, 106, 20
Modjaz M. et al., 2008, AJ, 135, 1136
Modjaz M., Kewley L., Bloom J. S., Filippenko A. V., Perley D., Silverman J. M., 2011, ApJL, 731, L4
Morgan H. L., Edmunds M. G., 2003, MNRAS, 343, 427
Moriya T., Tominaga N., Tanaka M., Nomoto K., Sauer D. N., Mazzali P. A., Maeda K., Suzuki T., 2010, ApJ, 719, 1445
Morrissey P. et al., 2005, ApJL, 619, L7
Morrissey P. et al., 2007, ApJS, 173, 682
Müller T., Nielbock M., Balog Z., Klaas U., Vilenius E., 2011a, PACS Photometer – Point-Source Flux Calibration (PICC-ME-TN-037)
Müller T., Okumura K., Klaas U., 2011b, PACS Photometer Passbands and Colour Correction Factors for Various Source SEDs (PICC-ME-TN-038)
Nagakura T., Hosokawa T., Omukai K., 2009, MNRAS, 399, 2183
Nakano S., Itagaki K., Puckett T., Gorelli R., 2006, Central Bureau Electronic Telegrams, 666, 1
Neufeld D. A., Lepp S., Melnick G. J., 1995, ApJS, 100, 132
Neugebauer G. et al., 1984, Science, 224, 14
Nordgren T. E., Chengalur J. N., Salpeter E. E., Terzian Y., 1997, AJ, 114, 913
Nozawa T. et al., 2008, ApJ, 684, 1343
Nozawa T., Maeda K., Kozasa T., Tanaka M., Nomoto K., Umeda H., 2011, ApJ, 736, 45
Oberst T. E. et al., 2006, ApJL, 652, L125
Oey M. S., Massey P., 1995, ApJ, 452, 210
O'Halloran B. et al., 2010, A&A, 518, L58
Ott S., 2010, in Y. Mizumoto, K.-I. Morita & M. Ohishi ed., Astronomical Data Analysis Software and Systems XIX Vol. 434 of Astronomical Society of the Pacific Conference Series, The Herschel Data Processing System – HIPE and Pipelines – Up and Running Since the Start of the Mission. p. 139
Pagel B. E. J., Edmunds M. G., Blackwell D. E., Chun M. S., Smith G., 1979, MNRAS, 189, 95

Pastorello A. et al., 2007, Nature, 447, 829
Pastorello A. et al., 2008, MNRAS, 389, 113
Peeters E., Hony S., Van Kerckhoven C., Tielens A. G. G. M., Allamandola L. J., Hudgins D. M., Bauschlicher C. W., 2002, A&A, 390, 1089
Peeters E., Tielens A. G. G. M., Allamandola L. J., Wolfire M. G., 2012, ApJ, 747, 44
Peimbert M., 1967, ApJ, 150, 825
Peimbert M., Costero R., 1969, Boletin de los Observatorios Tonantzintla y Tacubaya, 5, 3
Peimbert M., Torres-Peimbert S., 1977, MNRAS, 179, 217
Perets H. B. et al., 2010, Nature, 465, 322
Pilbratt G. L. et al., 2010, A&A, 518, L1
Planck Collaboration 2011, A&A, 536, A7
Poglitsch A. et al., 2010, A&A, 518, L2
Pohlen M. et al., 2010, A&A, 518, L72
Poole T. S. et al., 2008, MNRAS, 383, 627
Porter A. C., Filippenko A. V., 1987, AJ, 93, 1372
Proctor R. N., Forbes D. A., Romanowsky A. J., Brodie J. P., Strader J., Spolaor M., Mendel J. T., Spitler L., 2009, MNRAS, 398, 91
Purcell E. M., 1969, ApJ, 158, 433
Reach W. T. et al., 2005, PASP, 117, 978
Reeves H., Salpeter E. E., 1959, Physical Review, 116, 1505
Reines A. E., Johnson K. E., Goss W. M., 2008, AJ, 135, 2222
Relaño M., Kennicutt Jr. R. C., Eldridge J. J., Lee J. C., Verley S., 2012, MNRAS, 423, 2933
Rémy-Ruyer A. et al., 2013, A&A, in prep.
Rich R. M., Collins M. L. M., Black C. M., Longstaff F. A., Koch A., Benson A., Reitzel D. B., 2012, Nature, 482, 192
Roming P. W. A. et al., 2005, Space Sci. Rev., 120, 95
Roussel H., 2012, e-print (astro-ph/1205.2576)
Russell S. C., Dopita M. A., 1992, ApJ, 384, 508
Sahu D. K., Anupama G. C., Srividya S., Muneer S., 2006, MNRAS, 372, 1315
Sakon I. et al., 2009, ApJ, 692, 546
Salas P., Bauer F. E., Stockdale C., Prieto J. L., 2013, MNRAS, 428, 1207
Salpeter E. E., 1952, Physical Review, 88, 547
Salpeter E. E., 1955, ApJ, 121, 161
Salpeter E. E., 1977, ArA&A, 15, 267
Sanders D. B., Mazzarella J. M., Kim D.-C., Surace J. A., Soifer B. T., 2003, AJ, 126, 1607
Sandstrom K. M. et al., 2012, ApJ, submitted (astro-ph/1212.1208)
Sauvage M., 2011, Experiments in photometric measurements of extended sources (SAp-PACS-MS-0718-11)
Schaerer D., Stasińska G., 1999, A&A, 345, L17
Schechtman-Rook A., Bershady M. A., Wood K., 2012, ApJ, 746, 70
Schlegel D. J., Finkbeiner D. P., Davis M., 1998, ApJ, 500, 525
Schruba A. et al., 2012, AJ, 143, 138
Seki J., Yamamoto T., 1980, ApSS, 72, 79
Sellgren K., Werner M. W., Ingalls J. G., Smith J. D. T., Carleton T. M., Joblin C., 2010, ApJL, 722, L54
Skillman E. D., Terlevich R., Teuben P. J., van Woerden H., 1988, A&A, 198, 33
Skrutskie M. F. et al., 2006, AJ, 131, 1163
Sloan G. C. et al., 2012, ApJ, 752, 140
Sloan G. C., Kraemer K. E., Matsuura M., Wood P. R., Price S. D., Egan M. P., 2006, ApJ, 645, 1118
Smartt S. J., 2009, ArA&A, 47, 63
Smartt S. J., Eldridge J. J., Crockett R. M., Maund J. R., 2009, MNRAS, 395, 1409
Smith H. A. et al., 2010, ApJ, 716, 490
Smith J. D. T. et al., 2007, ApJ, 656, 770
Smith L. J., Norris R. P. F., Crowther P. A., 2002, MNRAS, 337, 1309
Smith N., Foley R. J., Filippenko A. V., 2008, ApJ, 680, 568
Spoon H. W. W., Marshall J. A., Houck J. R., Elitzur M., Hao L., Armus L., Brandl B. R.,

Charmandaris V., 2007, ApJL, 654, L49
Springel V. et al., 2005, Nature, 435, 629
Stacey G. J., Geis N., Genzel R., Lugten J. B., Poglitsch A., Sternberg A., Townes C. H., 1991, ApJ, 373, 423
Stecher T. P., 1969, ApJL, 157, L125
Stecher T. P., Williams D. A., 1967, ApJL, 149, L29
Sturm E. et al., 2011 Vol. 52 of EAS Publications Series, Star formation and the ISM in infrared bright galaxies – SHINING. pp 55–61
Sugerman B. E. K. et al., 2006, Science, 313, 196
Swaters R. A., van Albada T. S., van der Hulst J. M., Sancisi R., 2002, A&A, 390, 829
Szalai T., Vinkó J., 2013, A&A, 549, A79
Temim T. et al., 2006, AJ, 132, 1610
Theis C., Kohle S., 2001, A&A, 370, 365
Thomas D., Maraston C., Bender R., 2003, MNRAS, 339, 897
Thronson Jr. H. A., Hunter D. A., Telesco C. M., Decher R., Harper D. A., 1987, ApJ, 317, 180
Tielens A. G. G. M., 2012, in Tuffs R. J., Popescu C. C., eds, IAU Symposium Vol. 284 of IAU Symposium, Chemical and physical properties of interstellar dust. pp 72–81
Tielens A. G. G. M., Hollenbach D., 1985, ApJ, 291, 722
Todini P., Ferrara A., 2001, MNRAS, 325, 726
Tominaga N. et al., 2008, ApJ, 687, 1208
Toomre A., 1964, ApJ, 139, 1217
Tully R. B., Shaya E. J., Karachentsev I. D., Courtois H. M., Kocevski D. D., Rizzi L., Peel A., 2008, ApJ, 676, 184
Valdez-Gutiérrez M., Rosado M., Puerari I., Georgiev L., Borissova J., Ambrocio-Cruz P., 2002, AJ, 124, 3157
Valtchanov I., 2011, SPIRE Observers' Manual (HERSCHEL-DOC-0798, version 2.4)
van Hoof P. A. M., Verner D., 1997, in Heras A. M., Leech K., Trams N. R., Perry M., eds, The first ISO workshop on Analytical Spectroscopy Vol. 419 of ESA Special Publication, A Comprehensive IR Line List for Atomic Transitions on the WWW. p. 273
van Loon J. T., Groenewegen M. A. T., de Koter A., Trams N. R., Waters L. B. F. M., Zijlstra A. A., Whitelock P. A., Loup C., 1999, A&A, 351, 559
Vandenbussche B., Blommaert J., Contursi A., Feuchtgruber H., Jean C., Poglitsch A., Royer P., Vavrek R., 2011, PACS Spectroscopy performance and calibration (PICC-KL-TN-041)
Vasta M., Barlow M. J., Viti S., Yates J. A., Bell T. A., 2010, MNRAS, 404, 1910
Vázquez G. A., Leitherer C., 2005, ApJ, 621, 695
Ventura P. et al., 2012, MNRAS, 420, 1442
Vigroux L., Stasińska G., Comte G., 1987, A&A, 172, 15
Wada K., Norman C. A., 2001, ApJ, 547, 172
Waldrop M. M., 1987, Science, 235, 1322
Watson W. D., 1972, ApJ, 176, 103
Weingartner J. C., Draine B. T., 2001, ApJ, 548, 296
Werner M. W. et al., 2004, ApJS, 154, 1
Wesson R. et al., 2010, MNRAS, 403, 474
West A. A., Garcia-Appadoo D. A., Dalcanton J. J., Disney M. J., Rockosi C. M., Ivezić Ž., Bentz M. C., Brinkmann J., 2010, AJ, 139, 315
Witt A. N., Thronson Jr. H. A., Capuano Jr. J. M., 1992, ApJ, 393, 611
Wolfire M. G., Tielens A. G. G. M., Hollenbach D., 1990, ApJ, 358, 116
Wooden D. H., Rank D. M., Bregman J. D., Witteborn F. C., Tielens A. G. G. M., Cohen M., Pinto P. A., Axelrod T. S., 1993, ApJS, 88, 477
Woods P. M., Kelly G., Viti S., Slater B., Brown W. A., Puletti F., Burke D. J., Raza Z., 2012, ApJ, 750, 19
Woosley S. E., Bloom J. S., 2006, ArA&A, 44, 507
Woosley S. E., Weaver T. A., 1995, ApJS, 101, 181
Worthey G., 1994, ApJS, 95, 107
Worthey G., Ottaviani D. L., 1997, ApJS, 111, 377
Wright E. L. et al., 2010, AJ, 140, 1868

Wright N. J., Barlow M. J., Ercolano B., Rauch T., 2011, MNRAS, 418, 370
Wu X., Roby T., Ly L., 2010, in Society of Photo-Optical Instrumentation Engineers (SPIE) Conference Series Vol. 7737 of Society of Photo-Optical Instrumentation Engineers (SPIE) Conference Series, Spitzer Heritage Archive
Yin J., Hou J. L., Prantzos N., Boissier S., Chang R. X., Shen S. Y., Zhang B., 2009, A&A, 505, 497
York D. G. et al., 2000, AJ, 120, 1579
Yoshii Y., Tsujimoto T., Nomoto K., 1996, ApJ, 462, 266
Zubko V., Dwek E., Arendt R. G., 2004, ApJS, 152, 211